UNIVERSITY OF MODENA AND REGGIO EMILIA

PhD Programme of Clinical and Experimental Medicine

Curriculum: Translational Medicine

PhD Cycle: XXXV

Director of the PhD Programme: Chiar.mo Prof. Marco Vinceti

THE ROLE OF INNATE IMMUNITY

IN SEVERE COVID-19

Supervisor:

Prof. Andrea Cossarizza

Candidate:

Dr. Rebecca Borella

Academic year 2021/2022

TABLE OF CONTENTS

ABSTRACT **4**

1. INTRODUCTION **6**

1.1. SARS-CoV-2: INFECTION AND DISSEMINATION **6**
1.2. GENERAL FEATURES OF CORONAVIRUS INFECTIONS: SARS, MERS, AND COVID-19 ..... **7**
1.3. CLINICAL PATHOLOGY OF COVID-19 ..... **10**
1.3.1. PNEUMONIA AND DAMAGES TO LUNG 10
1.3.2. HISTOPATHOLOGICAL CHARACTERISTICS 10
1.3.3. LUNG FIBROSIS, COAGULOPATHY, AND ENDOTHELIAL DAMAGE 11
1.4. HOST RESPONSE TO SARS-CoV-2: INFLAMMATION AND INNATE IMMUNITY **12**
1.4.1. CYTOKINE AND INFLAMMATORY MEDIATOR RESPONSE 12
1.5. MONOCYTES **14**
1.5.1. MAIN CHARACTERISTICS OF MONOCYTES 14
1.5.2. MONOCYTE METABOLISM 16
1.5.3. MONOCYTES AND COVID-19 PATHOGENESIS 17
1.6. NEUTROPHILS **18**
1.6.1. MAIN CHARACTERISTICS OF GRANULOCYTES 19
1.6.2. NEUTROPHIL METABOLISM 19
1.6.3. NEUTROPHILS AND COVID-19 PATHOGENESIS 20
1.7. TECHNOLOGIES TO STUDY THE METABOLISM AT THE CELLULAR LEVEL **21**
1.7.1. EXTRACELLULAR FLUX ANALYSIS 22
1.7.1.1. Glycolytic rate assay and glycolysis stress test 22
1.7.1.2. Mitochondrial stress test 23
1.7.2. FLOW CYTOMETRY AND CELL METABOLISM 23
1.7.3. RNA FLOW CYTOMETRY 25
1.7.4. THE NOVEL SCENITH ASSAY 26

AIMS OF THE THESIS **28**

2. METHODS **29**

2.1. ANALYSIS OF MONOCYTES **29**
2.1.2. HUMAN SAMPLES 29
2.1.3. BLOOD COLLECTION AND PBMC ISOLATION 29
2.1.4. PURIFICATION OF MONOCYTES AND ANALYSIS OF THEIR BIOENERGETIC STATUS 30
2.1.5. FLOW CYTOMETRY 31
2.1.6. IN VITRO STIMULATION OF MONOCYTES AND INTRACELLULAR CYTOKINE STAINING 31
2.1.7. TRANSMISSION ELECTRON MICROSCOPY 32
2.1.8. QUANTIFICATION OF CYTOKINE PLASMA LEVELS 32
2.1.9. STATISTICAL ANALYSIS 32
2.2. ANALYSIS OF GRANULOCYTES **34**
2.2.1. HUMAN SAMPLES 34
2.2.2. BLOOD COLLECTION 34
2.2.3. PURIFICATION OF NEUTROPHILS AND ANALYSIS OF THEIR BIOENERGETIC STATUS 35
2.2.4. FLOW CYTOMETRY 36
2.2.5. TRANSMISSION ELECTRON MICROSCOPY 36
2.2.6. RNA EXTRACTION, REVERSE TRANSCRIPTION, AND REAL-TIME QUANTIFICATION 37

2.2.7. Intracellular glycogen quantification 37
2.2.8. NET quantification 37
2.2.9. Western blot 38
2.2.10. Quantification of plasma levels of MPO, EL, and MPO-DNA complexes 38
2.2.11. Quantification of cytokine plasma levels 39
2.2.12. Reanalysis of single-cell RNA sequencing (scRNA-seq) data 39
2.2.13. Gene Ontology enrichment analysis 40
2.2.14. Analysis of the correlations among cytokines and clinical features 40
2.2.15. Statistical analysis 40

3. RESULTS 42

3.1. DATA ON MONOCYTES 42
3.1.1. Demographic and clinical characteristics of patients 42
3.1.2. Monocyte from COVID-19 patients displayed a compromised bioenergetic profile 42
3.1.3. Mitochondria in monocytes of COVID-19 patients exhibited ultrastructural rearrangements 43
3.1.4. Monocytes from COVID-19 patients maintained the capacity to produce cytokines 44
3.1.5. Different distribution of monocytes subsets and immune exhaustion 45
3.1.6. Presence of immature monocytes in peripheral blood of severe COVID-19 patients 46
3.2. DATA ON GRANULOCYTES 62
3.2.1. Circulating granulocytes are altered in severe COVID-19 patients 62
3.2.2. Circulating neutrophils displayed a remodeled metabolism 63
3.2.3. Neutrophils rely on glycolysis for NET formation 64
3.2.4. Pro-inflammatory cytokines trigger neutrophils metabolic rewiring in COVID-19 patients 66
3.2.5. Circulating neutrophils store glycogen, whose lysis is crucial for NET formation 66
3.2.6. Glycogenolysis is important for NET formation in COVID-19 patients 67
3.2.7. Cytokines and other soluble molecules regulating neutrophils' function are profoundly altered 67

4. DISCUSSION 97

4.1. Role and functionality of monocytes during COVID-19 97
4.2. Role and functionality of neutrophils during COVID-19 101

5. CONCLUSIONS 105

6. BIBLIOGRAPHY 107

ABSTRACT

COVID-19 is a disease caused by SARS-CoV-2 infection, triggering a complex immune response that often worsens the course of the disease. In all infections, innate immunity is the first line of defence and, as previously described by our group, a hyperactivation of innate immune cells leads to a persistent inflammatory status that contributes to the immunopathogenesis of severe COVID-19. Therefore, my studies aimed at the identification of main pathophysiological mechanisms that are triggered by soluble molecules and cells belonging to innate immunity, like monocytes and neutrophils, and their contribution to the heterogeneity of the symptomatology of COVID-19.

For this, two cohorts of patients with COVID-19 pneumonia were investigated. The first one comprised 28 patients and 27 healthy donors (HD) and was used to characterize metabolism, phenotype, and functions of circulating monocytes. The second one included 88 patients and 59 HD and was studied to dissect mechanisms underlying the neutrophilic response during SARS-CoV-2 infection. In this thesis, it is reported how monocytes from severe COVID-19 patients are metabolically impaired. In COVID-19 patients, the percentage of monocytes with depolarized mitochondria (mt) was increased as well as their mt mass and mt ultrastructure was profoundly altered compared to healthy monocytes. Moreover, dysfunctional monocytes expressed low levels of HLA-DR and showed a reduced capacity to perform the oxidative burst, but they were still able to produce cytokines. A relevant redistribution of monocyte subsets was also detected, with an expansion of intermediate monocytes, which have pro-inflammatory function, and a reduction of nonclassical monocytes. In all subsets inhibitory checkpoints PD-1 and PD-L1 were overexpressed, probably contributing to immune exhaustion. Finally, plasma concentration of several mediators involved in monocyte regulation and migration was higher in COVID-19 patients such as granulocyte-macrophage colony-stimulating factor (GM-CSF), suggesting the presence of emergency myelopoiesis in severe patients. In fact, immature monocytes were significantly increased in peripheral blood from COVID-19 patients.

Regarding neutrophils, formal evidence of their functional status in severe COVID-19 patients was missing. Here, it is shown that circulating granulocytes were altered in severe COVID-19 patients, with a higher proportion of immature neutrophils and more degranulated neutrophils. The analysis of neutrophil bioenergetic profile revealed a decreased spare respiratory capacity and a defective respiratory burst in neutrophils from COVID-19 patients versus HD. However, glycolysis

and glycolytic capacity were strongly increased which sustain neutrophils extracellular traps (NET) formation. Other than glycolysis, other metabolic routes have been recently associated with neutrophils' differentiation and function. Large intracytoplasmic deposits of glycogen in neutrophils from COVID-19 patients compared to HD were observed, along with increased levels of intracellular glycogen and mRNA levels of glycogen phosphorylase L (*PYGL*), which catalyses glycogenolysis. Indeed, neutrophils can use glycogen for NET formation. The analysis of cytokine and chemokine profile in patients with severe COVID-19 revealed that they are profoundly altered delineating an activation pattern which correlates with the severity of the disease of COVID-19. In conclusion, data suggested that infection with SARS-CoV-2 can heavily affect the innate compartment of immune system.

Monocytes and neutrophils have a remodelled phenotype and metabolism that can prove effective targets for innovative therapies. The upregulation of inhibitory checkpoints on monocytes could thus represent an interesting strategy for immunotherapy, whereas the increased glycolysis and glycogenolysis in neutrophils, crucial for NET formation, suggest possible novel strategies to control inflammatory diseases.

1. INTRODUCTION

1.1. SARS-CoV-2: infection and dissemination

SARS-CoV-2 is a member of the coronavirus family, a large family of single-stranded RNA viruses that can be isolated from various animal species and by zoonotic transfer can cause severe diseases in humans such as severe acute respiratory syndrome (SARS) and Middle East respiratory syndrome (MERS). Prior to SARS outbreak in 2003, in China, coronaviruses were considered exclusively veterinary pathogens, now they are considered agents responsible for human respiratory pathologies as demonstrated during SARS, MERS and the current COVID-19 epidemic caused by SARS-CoV, MERS-CoV and SARS-CoV-2, respectively (Machhi *et al*, 2020; Coleman and Frieman, 2014; Siddamreddy *et al*, 2020). Despite the markedly lower fatality rate of COVID-19 compared with the previous coronavirus epidemics, its rapid global spread has had a devastating impact on almost every part of society worldwide, including healthy system, national economics and daily habits and lifestyle (Zhu *et al*, 2020; Osuchowski *et al*, 2021). An extraordinary response of the medical and scientific communities was observed for gaining insight into the COVID-19 epidemiology and pathophysiological mechanisms to implement optimum management strategies and improve care for patients with the infection (Osuchowski *et al*, 2021).

COVID-19 transmission occurs via airborne particles and droplets of respiratory fluids containing SARS CoV-2 virus that are released into the air by infected individuals when they exhale (e.g., breathing, coughing, sneezing, exercising, or talking). Droplets or aerosol particles vary in sizes, from visible to microscopic. Once released from the infected source, particles continue to spread through the air, carrying the virus and transmitting infection. This happens more easily indoors where the very fine droplets can accumulate in the air in the room and may be inhaled by people who stand in close proximity without covering mouth and nose.

The particles can linger in the air after a person has left the room and remain airborne for hours. Other ways of spreading include the exposition of splashes and sprays of respiratory fluids directly onto people mucous membranes, as well as touching mouth, eyes, or nose with unwashed hands and contacting contaminated surfaces or objects (Li *et al*, 2020). The faecal microbiota transplantation, which is an emergent treatment for the management of recurrent *Clostridioides difficile* infection, may also be a source for COVID-19 transmission, indeed stools from all donors have been screened for SARS-CoV-2 (Green *et al*, 2020). In contrast to influenza viruses, which

mainly infect cells in respiratory tracts and immune cells including alveolar and interstitial macrophages and natural killer cells, SARS-CoV-2 can target a wider range of cells. Main targets are alveolar type II cells in lung and macrophages, but it can also infect endothelial cells, cardiomyocytes, bile duct cells, stromal cells in adrenal gland, in ovary and in testis. Less often it targets kidney proximal tubule cells, and enterocytes. However, the highly acidic environment in the stomach neutralises the virus (Hikmet *et al*, 2020; Zhou *et al*, 2020b).

1.2. General features of Coronavirus infections: SARS, MERS, and COVID-19

SARS-CoV-2 has many structural and molecular similarities to SARS-CoV, which was responsible for the SARS outbreak originated in Guangdong, China in 2003, and MERS-CoV, causative agent of MERS outbreak that was first reported in Saudi Arabia in 2012 (Osuchowski *et al*, 2021). Coronaviruses (CoVs) are enveloped, spherical or variable in shape, with a diameter of 80–160 nm (Cui *et al*, 2019) and club-shaped glycoprotein spikes in the envelope that give the viruses a crownlike appearance. CoVs have the largest genome among all known RNA viruses, which is a positive, single-stranded RNA genome packed in a helical capsid. The capsid comprises the nucleocapsid protein N, surrounded by a membrane, that contains three proteins: the membrane protein (M) and the envelope protein (E), which are involved in the virus budding process, and the spike glycoprotein (S), which is a key viral player for host trophism, by determining virus entry into host cells through binding cell receptors and initiating membrane fusion (Li, 2016; Cueno and Imai, 2021). The SARS-CoV-2 genome contains ~30 kilobases (Cao *et al*, 2021) and shows 79.0% and 51.8% nucleotide sequence identity to SARS-CoV and MERS-CoV, respectively. SARS-CoV-2 shares 87.6–89% nucleotide identity with bat-origin SARS-like coronavirus (bat-SLCoVZC45) (Ren *et al*, 2020), for this reason bats are considered to be the natural hosts for SARSCoV-2, whereas Pangolins are believed to be one of the intermediate hosts for species viral transfer to humans (Lam *et al*, 2020). SARS-CoV and SARS-CoV-2 both bind to the human angiotensin-converting enzyme 2 (ACE2) receptor expressed in epithelial cells for viral entry. As mentioned before, viral protein S is responsible for the binding, and according to the sequence alignment, the SARS-CoV and SARS-CoV-2 S protein structures are highly conserved (Baig *et al*, 2020; Srinivasan *et al*, 2020; Wrapp *et al*, 2020). S is trimeric where each monomer contains two subunits: S1 and S2, which mediate attachment and membrane fusion, respectively. S1 itself can be subdivided further into S1a and S1b, where the latter includes the receptor-binding domain (RBD) (Shang *et al*, 2020). S1 contains the feature that allows the binding to ACE2 receptor and cell entry, whereas the S2 is the fusion

domain that enables the virus to fuse with the host cell membrane. Generally, in a virus RBD is characterized by high sequence variability that is also generated by the strong selective pressure exerted by the host immune system on the pathogen.

Differences between SARS-CoV-2 S protein from the original SARS-CoV spike protein have been identified. One difference regards the composition of the six critical amino acids within the ACE2 binding domain. In SARS-CoV-2 five of these six residues are different from SARS-CoV enabling a much more efficient interaction of SARS-CoV-2 with the ACE2 receptor compared to the previous SARS-CoV (Wrapp *et al*, 2020; Yan *et al*, 2020). Another difference which is a distinguishing feature of SARS-CoV-2 is the presence of a polybasic cleavage site in the region critical for fusion peptide activation, at the S1/S2 boundary. This enables the cleavage of the spike precursor by proteases that are different from those used by SARS-CoV and facilitates the processing of spike precursor earlier during viral assembly in the producer cell, rather than later during entry into the target cell. This feature has been suggested to be determinant for the increased transmissibility between individuals of SARS-CoV-2 compared to SARS-CoV (Yan *et al*, 2020; Winstone *et al*, 2021). Host cell proteases play a crucial role for the priming of the viral spike protein that triggers the conformational shifts (cleavage) in S protein. Transmembrane protease serine 2 (TMPRSS-2) expressed on the target cell surface is responsible for the cleavage (Yan *et al*, 2020). Indeed, it has been reported that SARS-CoV-2 entry via ACE2 into the host cell could be blocked by an inhibitor of TMPRSS2. Thus, molecules targeting ACE2, and inhibiting proteases could be used as therapeutic agents to contrast the rapid SARS-CoV-2 transmission (Hoffmann *et al,* 2020). Other receptors previously used by SARS-CoV to bind the host cell (e.g., L-SIGN and DC-SIGN), are under investigation to understand whether they can be alternatively used also by SARS-CoV-2 for binding and determining its cell tropism (Li *et al*, 2005; Masters, 2006; deWit *et al*, 2016). SARS-CoV-2 mainly targets the lungs by binding primarily to ACE2 receptors expressed on type 2 pneumocytes (Chaouat *et al*, 2021; Loganathan *et al*, 2021), but due to the large expression of ACE2 on several other cell types, the virus can target and damage other organs such as heart, liver, kidneys, blood, and immune system (Wang *et al*, 2020c).

An apparent discrepancy in the outcome of MERS-CoV- and SARS-CoV-infection was found, along with a different pathogenicity of the two viruses. In fact, MERS-CoV could productively infect immune cells with efficient transcription and translation of the viral genome, in contrast to SARS-CoV, whose infection in monocyte-derived-dendritic cells is abortive since the virus is unable to propagate (Chu *et al*, 2014). Regarding SARS-CoV-2 mechanisms of infection in immune cells it has

been reported that it can directly infect monocytes (Wang *et al*, 2020a). SARS-CoV-2 actively replicate in the upper respiratory tract during both pre-symptomatic and symptomatic phases (Rockx *et al*, 2020; Wölfel *et al*, 2020). Viral loads from respiratory tract samples were found to be much higher than from other samples such as urine, peripheral blood, ocular secretions (Puhach *et al*, 2022), for this reason greater attention has been put on SARS-CoV-2 infection through the respiratory tract.

COVID-19 disease symptoms are very heterogeneous among patients. Some symptoms are incredibly severe, while others are so mild that infected subjects can be defined as asymptomatic (Guo *et al*, 2020). Severe COVID-19 shows a typical pattern of progression of the disease, whereas patients affected by the mild form of the disease can recover after few days from the infection, or suffer from persistent symptoms, or may get worse again shortly thereafter (Song *et al*, 2020). Within 14 days after virus exposure symptoms begin to appear, which are commonly fever, cough, headache, muscle pain, sore throat, loss of taste or smell. In severe COVID-19, the clinical situation of the patients becomes more critical with the development of respiratory difficulties due to pneumonia (Chen *et al*, 2020; Huang *et al*, 2020). COVID-19 pneumonia in adults is characterised by typical clinical signs as fever and cough, aggravated by respiratory impairment which means a respiratory rate of more than 30 breaths per min, a ratio of partial pressure of arterial oxygen (PaO_2) to fractional concentration of oxygen in inspired air (FiO_2) ≤ 300 mm Hg or oxygen saturation (SpO_2) <93%. The life-threatening impairment of oxygenation is defined as hypoxaemia, which can worsen and result in the development of acute respiratory distress syndrome (ARDS). About 80% of patients with COVID-19 develop mild-to-moderate symptoms, 15% progress to severe disease stages requiring oxygen support, and 5% develop critical disease including ARDS, septic shock with various deleterious effects such as cell apoptosis, endothelial inflammation, neovascularisation, thrombotic events, multiorgan dysfunction or failure (Osuchowski *et al*, 2021; MacIntyre, 2013; Bein *et al*, 2016).

An early identification and treatment of hypoxemia is mandatory. For the management of severe ARDS ventilator settings, positioning therapy, infection control, and supportive measures are essential to improve survival. Most clinicians use invasive mechanical ventilation via an endotracheal tube or tracheostomy, for patients with moderate or severe ARDS. Non-invasive ventilation (NIV) carried out by using a mask, nasal prongs, or helmet with breaths delivered by an NIV device, may be reserved for mild patients who don't present contraindications to its use, are

hemodynamically stable, and do not need immediate intubation (Griffiths *et al*, 2019). Despite such intensive efforts, approximately 40% of ARDS patients do not survive.

1.3. Clinical pathology of COVID-19

In the last years, the pathogenesis of COVID-19 has been explored in detail by an uncountable number of studies. Here some pivotal observations on tissue damages that are induced by SARS-CoV-2, as well as by the response to the virus, are resumed.

1.3.1. Pneumonia and damages to lung

An atypical cause of respiratory failure in severe COVID-19 patients is silent hypoxaemia, a condition characterised by a very low PO_2 and critical PO_2/FiO_2 but not shortness of breath (Siswanto *et al*, 2020; Dhont *et al*, 2020). Hypoxaemia is not always associated with sensation of breathlessness (Manning and Schwartzstein, 1995), but it is strictly related to the increase of the respiratory drive due to the exposure to low PaO_2 (<60 mm Hg). The respiratory drive is the intensity of neural stimulus to breath directed to respiratory muscles to generate inspiratory effort and tidal breathing (Spinelli *et al*, 2020). Several pathophysiological events that disrupt lung function in COVID-19 patients such as the progressive pulmonary inflammation, alveolar collapse and fibrosis can explain tissue hypoxia (Osuchowski *et al*, 2021).

1.3.2. Histopathological characteristics

Features of severe COVID-19, described in deceased patients, include perturbation of the lung with an increased organ weight, oedema, and a remodelling of parenchyma with hyperplasia, metaplasia, and necrosis of pneumocytes. In addition, the respiratory tract was found to be damaged with bronchial obstruction and intraalveolar fibrin deposition (Carsana *et al*, 2020). Angiogenesis was upregulated and microthrombosis occurred within alveolar capillaries (Ackermann *et al*, 2020). The latter was also caused by infiltration of leukocytes in the alveolar lumina, and of lymphocytes and monocytes in the interstitium (Carsana *et al*, 2020). Another hallmark of SARS-CoV-2 infection shared with SARS and H1N1 influenza, was the appearance of haemophagocytosis in the pulmonary lymph nodes, suggesting the presence of an overproduction and uncontrolled release of proinflammatory cytokines (especially interferon (IFN)-γ) also known as cytokine storm syndrome (Prilutskiy *et al*,2020; Gao *et al*, 2020).

To predict early outcome of patients with COVID-19-associated ARDS, the combination of two more factors had been evaluated. These are static compliance of the respiratory system and D-dimer concentrations. Compliance describes the expandability of the lungs and chest wall and can be dynamic or static. These two conditions are defined as the change in lung volume by the change in pressure in the presence or absence of flow, respectively. COVID-19 patients with low static compliance and high D-dimer concentrations have the highest risk of mortality (Tonetti *et al*, 2021). Intermittent prone positioning appears to improve gas exchange. In worse conditions, for patients presenting pulmonary failure with an oxygenation index ≤ 80 mmHg for more than 3 hours, extracorporeal membrane oxygenation is indicated as a treatment (Sorbello *et al*, 2020).

1.3.3. Lung fibrosis, coagulopathy, and endothelial damage

Lung fibrosis is a known complication of ARDS and correlates with poor prognosis. The onset of this process is driven by secretion of pro-fibrotic factors. Transforming growth factor-β (TGF-β) signalling is crucial for the repair of infection-injured lung, but when excessively secreted as in severe COVID-19, it can contribute to pulmonary fibrosis (Wilson *et al*, 2009; Chen, 2020). This was observed to be a common complication of SARS, MERS, and COVID-19. Among survivors after recovery from SARS and MERS, older patients frequently developed it, and its extent was directly correlated to the duration of disease (Hui *et al*, 2005). In patients recovered from severe COVID-19, who experienced a strong inflammatory reaction, pulmonary fibrosis could be early predicted by detecting parenchymal abnormalities using computed tomography scanning (Yu *et al*, 2020).

In the lungs of COVID-19 severe patients there is a high prevalence of coagulopathy and endotheliopathy, which are strongly associated with poor prognosis and mortality (Guan *et al*, 2019; Zhou *et al*, 2020a). Hypercoagulability is defined by increased levels of D-dimer and fibrinogen (Guan *et al*, 2019; Leisman *et al*, 2020), and endotheliopathy is the pulmonary vascular dysfunction induced by dysregulated crosstalk between endothelial and immune cells (leukocytes), which aggravates hypoxaemia (Arachchillage *et al*, 2020). SARS-CoV-2 induced-vascular pathology is not only restricted to the lungs, it is often systemic and shared with other infectious disorders such as sepsis, that are characterized by abnormal nitric oxide metabolism, and oxidative stress also aggravated by disabled antioxidant mechanisms (Osuchowski *et al*, 2021).

1.4. Host response to SARS-CoV-2: inflammation and innate immunity

The innate immune system is the front line of the defences against this pathogen, and triggering inflammation is crucial for the immune response to occur. Different mediators and cells are involved and are briefly described here below.

1.4.1. Cytokine and inflammatory mediator response

A hallmark of severe SARS-CoV-2 infection is the uncontrolled cytokine production by the dysregulated immune system known as "cytokine storm" syndrome (Moore and June, 2020; Zhang *et al*, 2020b). This phenomenon is not new, it has been in association with several viral infection-derived diseases such as SARS, MERS, seasonal influenza, avian flu (H5N1) and pandemic influenza (H1N1 2009) (Ryabkova *et al*, 2021). Increased neutrophil-to-lymphocyte ratio (NLR) in COVID-19 patients is a clear indicator of cytokine storms. The excessive cytokine release dramatically increases leukocyte recruitment to the site of injury, in particular to lung cells, followed by the activation of tissue repair mechanisms which, if not controlled, lead to the severe hypoxemic respiratory failure and systemic inflammatory condition typical of ARDS (Zhang *et al*, 2020a; Gibson *et al*, 2020).
Cytokine production in COVID-19 can be triggered or by direct recognition of the SARS-CoV-2 by immune cells or indirectly through the signalling of associated molecular patterns (DAMPS), released from epithelial cells damaged by the virus. Direct recognition of the pathogen happens through the binding of pattern-recognition receptors (PRRs), such as virus-specific Toll-like receptors (TLR3, TLR7, TLR8, and TLR9) (Onofrio *et al*, 2020). Defects in these receptors are associated with the development of the severe form of COVID-19 (Zhang *et al*, 2020c). Damaged cells (endothelial, epithelial, parenchymal cells) release immunogenic molecules recognized mainly by PRRs and trigger immune activation, in particular macrophages' activation. This leads to the production of several proinflammatory cytokines and chemokines including tumor necrosis factor (TNF), monocyte chemoattractant protein-1 (MCP-1), C-C motif chemokine ligand (CCL)2, macrophage inflammatory proteins (MIP)1α, C-X-C motif chemokine ligand (CXCL)10, whose plasma concentration increased in patients with severe COVID-19 admitted to the intensive care unit (ICU) (Huang *et al*, 2020). Moreover, increased circulating levels of interleukin (IL)-6 were correlated with COVID-19 severity and IL-1 production was upregulated in cells from infected subjects (Chen G. *et al*, 2020).

It was reported an increase in classic monocyte subset in patients with COVID-19 with high IL-1β expression (Giamarellos-Bourboulis *et al*, 2020). Whereas the expression of the HLA-DR on circulating monocytes from COVID-19 patients was decreased, but nevertheless cells remain highly capable to produce cytokines (Gill *et al*, 2020). Interferon signalling was defective in severe COVID-19, (Hadjadj *et al*, 2020; Galani *et al*, 2021) as demonstrated by restricted or delayed interferon type I and type II responses in patients with severe COVID-19 compared to those with severe influenza characterized by a main early IFN response. Some studies reported the evidence of the cytokine response directly in lungs of COVID-19 patients. A viral specific activation signature of proinflammatory genes was confirmed in the bronchoalveolar lavage fluid (BALF) of patients with COVID-19 compared to patients with non-COVID-19 related pneumonia and healthy subjects. TNF, IL-1β, IL-6, IL-8, IL-10, MCP-1, CXCL10, MIP-1α, and MIP-1β were upregulated in BALF from patients with COVID-19 (Xiong *et al*, 2020). In a study investigating lungs from patients died of COVID-19 and from patients died of respiratory failure due to influenza H1N1, it was observed an increased RNA expression of CXCL8 and CXCL13 in lungs from patients with COVID-19 and increased IL-6 expression in both groups (Ackermann *et al*, 2020).

In severe COVID-19, ferritin has been studied as an inflammatory mediator and it is indeed a good marker of disease severity and predictor of mortality (Mesas *et al*, 2020; Cheng *et al*, 2020). Circulating ferritin is normally a marker of secondary haemophagocytic lymphohistiocytosis (HLH) and macrophage activation syndrome (MAS-HLH) in critically ill patients (Lachmann *et al*, 2020; Kyriazopoulou *et al*, 2017). In severe COVID-19 patients, high levels of circulating ferritin were associated with increased IL-1β production from ex vivo-stimulated circulating monocytes, simulating a MAS-HLH like condition (Giamarellos-Bourboulis *et al*, 2020), which was also confirmed by autopsy of lymph nodes and bone marrow of SARS-CoV-2 infected patients. Ferritin concentration in blood of patients with COVID-19 admitted at the hospital was correlated to other severity-associated markers belonging to the host-defence complement system, such as C5a and C5b (Cyprian *et al*, 2021). Another important predictor of COVID-19-related mortality in patients ≥ 60 years old is C reactive protein (CRP) whose elevated concentrations correlate with COVID-19 severity (Feng *et al*, 2020). Procalcitonin has proven useful in the early diagnosis of bacterial infections occurring at the lower respiratory tract (Schuetz *et al*, 2011). In a meta-analysis including 5912 patients with COVID-19, procalcitonin concentration in severe disease was double that in mild disease (Bao *et al*, 2020).

1.5. Monocytes

Monocytes develop in the bone marrow and represent the primary type of mononuclear phagocyte found in the blood. This family of myeloid cells comprises monocytes, dendritic cells (DCs) and macrophages. Monocytes constitute around 5-10% of peripheral-blood leukocytes in humans and present a heterogeneous morphology when circulating in the blood. They vary in size and have different degrees of granularity and different nuclear morphology (Gordon *et al,* 2005*)*.

1.5.1. Main characteristics of monocytes

Circulating monocytes have both the capability to transmigrate across the endothelium and enter the tissues in response to appropriate signals including pro-inflammatory, metabolic, and immune stimuli, as well as to patrol the vessel walls and support endothelial cell functions (Auffray *et al*, 2007). Migrating monocytes can develop in different ways, either remaining as monocytes within the tissue, or differentiating into antigen-presenting cells and macrophages and contribute to host defence, tissue remodelling and repair (Jakubzick CV. *et al,* 2017). In the steady state, monocytes continuously enter in non-inflamed tissues without differentiating into macrophages or classical DCs (cDCs), and finally undergo local apoptosis and clearance (Gautier *et al*, 2013). When they have interacted with the endothelium, they generally maintain their transcriptional profile apart from few changes, including the upregulation, at gene and protein level, of the expression of IL-1β, TNF, MHC class II, CD206, CD11c and CC-chemokine receptor (CCR)7 and the loss of expression of lymphocyte antigen 6 complex (LY6C) and CD62L (Jakubzick C. *et al*, 2017). The increased expression of MHC class II, co-stimulatory molecules and CCR7 shown suggests that these cells are required for trafficking the antigens to the draining lymph nodes and present them to cognate T cells (Jakubzick C. *et al*, 2017).

Monocyte migration and retention in inflamed sites is enhanced during inflammation due to the presence of pro-inflammatory mediators including chemokines, complement components and the products of tissue matrix degradation that trigger the extravasation of monocytes. In these circumstances, monocytes become the dominant mononuclear phagocyte present in inflamed tissues and in draining lymph nodes and gain several pro-inflammatory properties (Jakubzick CV. *et al,* 2017). The tissue recruitment of monocytes is highly dependent on the expression of CCR2 which determines $CCR2^{+}$ monocyte migration towards its ligand CCL2 also known as MCP-1 (Palframan *et al*, 2001). Once at the inflamed site the $CCR2^{+}$ monocytes upregulated expression of CD11c and MHC

class II molecules and differentiate into DCs, as demonstrated with the finding of some $CD11c^{+}$MHC class II^{+} cells in the draining lymph nodes. Other than secreting inflammatory mediators at the site of injury, monocytes undergo changes in metabolism, in cell size and in cytoplasmic complexity that involve the endoplasmic reticulum, mitochondria and lysosomes. During an infection, monocytes produce TNF and nitric oxide (NO) to control and drive microbial clearance as originally demonstrated during infection of mice with *Listeria monocytogenes* (Serbina *et al*, 2003). Subsequently, many other studies using different pathogenic models of bacterial, viral, and fungal infections have also highlighted the importance and requirement of TNF- and NO-producing monocytes as facilitators of the resolution of an infection (Shi *et al*, 2011). *In vivo* and *ex vivo* studies have shown that monocytes have an important role in both the trafficking and the presentation of antigens to cognate T cells, which supports the differentiation of specific T cell subsets. In lymph nodes, they can support the differentiation of T helper (TH), T follicular helper (TFH) cells and cytotoxic $CD8^{+}$ T cells. Monocytes can also exert suppressor functions promoting the inhibition of T cell proliferation and regulatory T (Treg) cell development (Augier *et al*, 2010). This influence exerted by monocytes on the adaptive immune response can be useful to understand the contribution of monocytes in pathological responses and to define some strategies to prevent them in diseases such as cancer, and metabolic syndrome (Jakubzick CV. *et al,* 2017).

The application of flow cytometry and novel single-cell transcriptomic and mass cytometry technologies allowed a deep phenotypic classification of human monocytes (Kapellos *et al*, 2019). Currently it is well established that three major populations of monocytes exist, which are classical ($CD14^{+}CD16^{-}$), intermediate ($CD14^{+}CD16^{++}$) and non-classical ($CD14^{-}CD16^{++}$) monocytes. Each of these subsets is distinguished from each other by the remarkable heterogeneity in their surface marker expression and function in homeostasis and disease (Kapellos *et al*, 2019). Classical monocytes were found to be primed for phagocytosis, immune responses and migration, intermediate monocytes, the only subset expressing CCR5, were in charge for antigen presentation, cytokine secretion, apoptosis regulation, and differentiation, whereas nonclassical monocytes were assigned to complement and Fc gamma-mediated phagocytosis and adhesion (Wong *et al*, 2011). Classical monocytes express higher levels of chemokine receptors, such as CCR2, CCR5, CXCR2, thus migrate to CCL2 and CCL3 gradients and are more efficient than intermediate monocytes in producing reactive oxygen species (ROS) and constraining fungi (Weber *et al*, 2000). Intermediate monocytes express the highest levels of antigen presentation-related molecules and can secrete TNF, IL-1β, IL-6, and CCL3 upon TLR stimulation (Wong *et al*, 2011; Lee *et al*, 2017). Regarding

chemokine receptors, they express more CCR5 than classical monocytes and this likely accounts for their high susceptibility to HIV-1 infection (Ellery *et al*, 2007). Non-classical human monocytes differ from classical subset for several reasons. Non-classical monocytes express a distinct transcriptomic and metabolic profile preferring a respiratory metabolism instead of glycolysis. They are distinguished from classical monocytes by their association with wound healing processes. Furthermore, they do not produce as many proinflammatory cytokines as the classical monocytes (Kapellos *et al*, 2019) and promote neutrophil adhesion at the endothelial interface via the secretion of TNF (Chimen *et al*, 2017). Taken together, human monocyte subsets display remarkable heterogeneity in their surface marker expression and function.

1.5.2. Monocyte metabolism

Metabolism plays an important role in the differentiation of monocytes and affect their functionality. Monocyte and derived-macrophage populations show a great plasticity in their metabolic features. During inflammation related for example to stimulation induced by microbial ligands, they rewire their metabolism to sustain their activation and generation of immune response (Tolstik *et al*, 2022). The metabolic reprogramming consists in a switch from oxidative phosphorylation to glycolysis, which sustains monocyte migration to the site of injury and their differentiation into pro-inflammatory macrophages (M1). Increased glycolysis also induces ROS production which exerts antibacterial activities (Kramer *et al*, 2014). Whereas, during the resolution of inflammation, anti-inflammatory macrophages (M2) become the main players sustained by oxidative phosphorylation and fatty acid oxidation (FAO) (Stunault *et al,* 2018; Shapiro *et al*, 2011). After resolution, homeostasis is recovered by restoring the balance between anabolic and catabolic processes (Zhu *et al*, 2019).

Alterations in the metabolic rewiring are involved in the pathogenesis of many diseases. As observed in sepsis, the decrease in mitochondrial function due to mitochondrial stress and damage leads to a reduction of ATP, NADH, and acetyl-CoA, which indeed promotes the development of immune metabolic paralysis, strongly related to increased mortality (Zhu *et al*, 2019; Japiassú *et al*, 2011). In type 2 diabetes monocytes showed a reduced mitochondrial mass and mitochondria hyperpolarization (Widlansky *et al*, 2012). In patients with fibromyalgia mitochondrial membrane potential in monocytes was decreased, in contrast to an increased superoxide production (Cordero *et al*, 2010). Lipopolysaccharide (LPS) stimulation in monocytes causes changes in the morphology of mitochondria including mitochondrial fragmentation which reduces mitochondrial length, and a

change in mitochondrial shape that leads to an increase in membrane potential (Zuo *et al*, 2019). As a result, the production of ROS in mitochondria is increased, and monocytes produce pro-inflammatory cytokines. Different from lymphocytes that mostly use oxidative phosphorylation, and from neutrophils which are entirely glycolytic, monocytes exhibit a high degree of aerobic glycolysis. The loss of the balance between oxidative phosphorylation and aerobic glycolysis with a switch towards the latter correlates with the age of monocytes. Elderly monocytes indeed show a reduced reserve respiratory capacity (known as the difference between maximal oxygen consumption induced by uncoupling and basal respiration) due to impaired metabolic fitness and a limited ability to utilize additional glucose (Tolstik *et al*, 2022).

1.5.3. Monocytes and COVID-19 pathogenesis

Profound COVID-related alterations in myeloid cell compartment have been reported by several authors in the very earliest phases of the pandemic. Severe COVID-19 is characterized by an increase in neutrophil count and a decrease of non-classical ($CD14^{-}CD16^{++}$) monocytes (Schulte-Schrepping *et al*, 2020). Circulating $CD16^{+}$ monocytes present a more activated phenotype with an increased IL-1 and IL-6 production in severe COVID-19 (Wen *et al*, 2020; Schulte-Schrepping *et al*, 2020). The observed cell activation is associated with changes in the transcriptomic profile and correlates with the severity of the disease. Genes involved in the antiviral interferon response (IFI27, IFITM3, IFI6, IFITM1), in inflammatory response (S100A8 and S100A9), in chemotaxis (CXCR2, CSF3R) and in cell adhesion (SELL) were found to be upregulated in $CD16^{+}$ monocytes in individuals with COVID-19 compared to healthy controls (Osuchowski *et al*, 2021).

Accordingly, single-cell studies of bronchoalveolar lavage samples confirmed the activation pattern in monocytes highlighting some differences between mild and severe COVID-19 disease. In mild COVID-19 patients activated $HLA\text{-}DR^{++}CD11c^{++}CD14^{+}$ monocytes were increased and characterized by high expression of IFN-stimulated genes. In contrast, monocytes from severe COVID-19 patients showed a low expression of HLA-DR associated with a high expression of alarmins S100A8, S100A9, S100A12 and anti-inflammatory mediators. Most classical monocytes showed high expression of activation markers CD38, CD95, and CXCR3 together with high levels of CD11c and HLA-DR. Other classical monocyte clusters expressed high levels of CD226 and CD69 but low HLA-DR suggesting an altered or alternative activation (Schulte-Schrepping *et al*, 2020; Davison *et al*, 2017). Upregulation of CD226 and CD69 in COVID-19 promotes diapedesis, tissue infiltration and

retention of monocytes (Davison *et al*, 2017; Reymond *et al*, 2004), thus reducing the presence of monocytes at the periphery. Of note, the presence of immature HLA-DR^{-}CD34^{+} monocytes was increased. Other than phenotypical changes, also metabolic perturbation are induced in monocytes by SARS-CoV-2 infection.

The infection triggers a significant downregulation of genes involved in oxidative phosphorylation encoding for mitochondrial electron transport chain complexes I and IV (Chilunda *et al*, 2021). This contributes to an impaired oxidative phosphorylation and ROS accumulation which induces stabilization of hypoxia-inducible factor-1α (HIF-1α) and consequently promotes glycolysis (Shenoy, 2020). This metabolic reprogramming promotes monocyte proinflammatory cytokines production and contributes to T cell dysfunction and epithelial cell death. To contrast the impaired immune response in COVID-19, targeting mtROS/HIF-1α/glycolysis axis can represent a therapeutic strategy, especially in subjects who are more prone to develop the severe form of the disease due to their clinical conditions like diabetic people presenting high blood glucose levels (Codo *et al*, 2020).

1.6. Neutrophils

Neutrophils are the most abundant type of peripheral leukocytes with a primary role in the response against extracellular pathogens as well as in acute inflammation. Mature adult neutrophils do not divide, contain lobulated nuclei, are short lived and are constantly replenished by the bone marrow (Lawrence *et al*, 2018). Neutrophils are effective antimicrobial cells exerting a plethora of functions. They phagocytose and kill prokaryotic and eukaryotic organisms very efficiently. They are able to degranulate and release different kind of enzymes, including elastase (EL) and myeloperoxidase (MPO) which participate in their effector functions. They can produce NET by decondensing their chromatin, decorating it with cytoplasmic or granule effector proteins, and then extruding it from the cells mainly to capture and kill bacteria (Lawrence Burn *et al*, 2021). Neutrophils can produce the respiratory burst, which is the rapid increase in the production of ROS during phagocytosis, and finally they can produce and release inflammatory mediators, including different types of chemokines and cytokines (Mantovani *et al*, 2011; Brinkmann *et al*, 2004). Neutrophils also interact with different immune cells through soluble factors and membrane receptors exposing antigens on their surface. This function is fundamental to regulate the activation and functionality of adaptative and innate immune cells (Lawrence Burn *et al*, 2021).

1.6.1. Main characteristics of granulocytes

Upon injury, neutrophils exit the bloodstream and move to the surrounding tissue to reach the site of the insult. To do this, neutrophils coordinate cellular movement using adhesion receptors. Neutrophil polarization and homing are sustained by chemotactic molecules, including lipid mediators, chemokines, and cytokines that are released from the injured site and intercepted by specific receptors on neutrophil cell surface. Extracellular matrix-degrading enzymes expressed by neutrophils then allow their entry to the injured site (Lawrence Burn *et al*, 2021). Once in the tissue, neutrophils deploy effector functions, die, and are cleared by macrophages (Fox *et al*, 2012). The amplitude and duration of neutrophil activation influence the outcome of the injury. Increasing evidence indicates that neutrophils are responsible for pathological manifestations within healthy tissues not belonging to the injured site. Indeed, activated neutrophils in the bloodstream may be lethal (Lawrence Burn *et al*, 2021). During the last years, it has become increasingly evident that neutrophils do not only exit the vasculature, but they can also re-enter the vasculature in a process named “reverse migration” (Mathias *et al*, 2006). The molecular determinants regulating reverse migration remain mostly undefined, although specific proteases might be important. Recent findings show that neutrophils also play critical roles in the resolution of inflammation (Selders *et al*, 2017). Indeed, neutrophils can produce anti-inflammatory molecules, which inhibit neutrophil trans-endothelial migration and tissue infiltration (Mantovani *et al*, 2011; Schwab *et al*, 2007; Serhan *et al*, 2008).

1.6.2. Neutrophil metabolism

Glycolysis has long been viewed as the sole source of energy for neutrophil functions. Defects in glucose shuttling between the endoplasmic reticulum and cytosol results in neutropenia and impairment in respiratory burst activity, ATP production and bacterial killing (Cheung *et al*, 2007; Kim *et al*, 2008; Jun *et al*, 2012). While glycolysis still remains the major metabolic pathway operating in neutrophil cytosol, recent studies indicate that other routes also act during their differentiation and function (Kumar *et al*, 2019). Neutrophils utilize pentose-phosphate pathway (PPP) to produce ribose-5-phosphate NADPH which is an important substrate for ROS production in activated neutrophils. In certain conditions, mainly due to limited availability of glucose, neutrophils also adapt to fatty acid metabolism and glutaminolysis. On the contrary, when glucose is abundant, they can store small amounts of glycogen (Kumar *et al*, 2019). Recent findings indicate that neutrophils are the only myeloid cell type capable of gluconeogenesis and glycogenesis, thus

indicating that they are able generate ATP in low-glucose and low-oxygen environments (Sadiku *et al*, 2021).

The metabolic plasticity of these cells helps to fulfil the energy requirement in the presence of inflammatory conditions and infections. Neutrophils react to different signals by increasing the uptake of glucose, and this suggests a crucial role of glucose in improving neutrophil functions. Several proteins and genes control the metabolism of neutrophils at the basis of their development and functionality (Kumar *et al*, 2019). At inflammatory sites, neutrophils contribute to hypoxia using oxygen during generation of ROS. As a response to hypoxia, the transcription factors HIF-1α and HIF-2α ensure neutrophil viability and functionality at the inflammatory sites (Walmsley *et al*, 2005). HIFs are regulated by oxygen pressure and prolyl hydroxylases domain (PHDs) enzymes, that hydroxylate HIFs and target them to ubiquitin-proteasome degradation. A study observed that the removal of PHD-2 triggers lung injury following increased neutrophil permanence. PHD2-lacking neutrophils showed increased glycolytic function, glycogen stores, and ATP levels (Sadiku *et al*, 2017).

1.6.3. Neutrophils and COVID-19 pathogenesis

In case of infection, granulocytes are the main actors of the early immune response and the first cells recruited to the site of infection. They also play a key role as mediators between the innate and adaptive branch of the immune system. Yet, if not properly regulated, the powerful effector functions of these cells can lead to tissue damage (Liew *et al*, 2019; Reusch *et al*, 2021). Granulocytes include eosinophils, basophils, and neutrophils. Hospitalized patients with COVID-19 presented alterations in all the subsets. The peripheral blood eosinophil count is decreased, indicating a higher incidence of complications and poor outcome of the patient with COVID-19 (Roca *et al,* 2021). Basophils displayed an activated phenotype in COVID-19 patients (Lourda *et al,* 2021) and are depleted during acute and severe phases of COVID-19 (Rodriguez *et al*, 2020). The number of circulating basophils in COVID-19 patients correlates to the titers of anti-receptor-binding domain IgG, according to the well-known mutual interaction between basophils and T and B cells (Rodriguez *et al*, 2020). Regarding neutrophils, several evidence indicates that neutrophils play a main role in SARS-CoV-2 infection and COVID-19 pathogenesis.

Neutrophilia is present with an increased neutrophil-to-lymphocyte ratio in blood of patients with COVID-19 (Qin et al, 2020). Neutrophils are hyperactivated, releasing ROS, such as superoxide, leading to oxidative stress and triggering the cytokine storm in SARS-CoV-2 infection. A higher

amount of NET is released, confirmed by the elevated levels of markers of NET formation (MPO, EL, citrullinated histone H3 -DNA, cell free DNA) in plasma from patients with COVID-19 (Zuo et al, 2020; Borella *et al*, 2022) which correlate with disease severity. NET-containing microthrombi have been detected in individuals who died after SARS-CoV-2 infection (Middleton *et al*, 2020). Moreover, an increased number of immature granulocytes has been observed in patients with severe COVID-19. This feature strongly suggests the presence of emergency hematopoiesis, that means the dramatic increase of the turnover of myeloid cell compartment that occurs during severe systemic bacterial infection, to fight invading pathogens (Schulte-Schrepping *et al*, 2020; Carissimo *et al*, 2020; Wilk *et al*, 2020; Boettcher and Manz, 2017).

Notably, neutrophils accumulate not only at the periphery but also in lung tissue of infected patients, as observed in analysis of post-mortem bronchial lumens, alveolar spaces, and pulmonary lesions (Carsana *et al*, 2020). The massive invasion of inflammatory neutrophils into the lung is promoted by pro-inflammatory mediators (i.e., CXCL1, CXCL2, CCL2), whose concentration has been found elevated in BALF (Hazeldine and Lord, 2021). The consequent worsening of the inflammatory state can lead to serious lung injury, ARDS, and in the worst case even death by COVID-19 (Xiong *et al*, 2020).

1.7. Technologies to study the metabolism at the cellular level

The phenotypic, functional, and transcriptional profile, even at single cell level, of heterogeneous immune cell populations has been analysed for several years through flow cytometry and then next generation sequencing. In the last decade immunologists have been exploring another important feature, the metabolic profile of immune cells and its impact on the modulation of the immune response. This rediscovery of metabolism has given rise to the new field of immunometabolism that studies the complex interplay between metabolic reprogramming and immunity and provided new insights about the physiopathology of the immune system in health and disease (O'Neill *et al,* 2016). In particular, the study of immunometabolism is largely involved in the field of cancer to outline how the harsh tumor microenvironment manipulates the metabolic changes that drive immune cell effector functions (Sugiura and Rathmell, 2018). It is well known that under normoxia normal cells first perform glycolysis in the cytosol to obtain energy, then mitochondrial oxidative phosphorylation (OXPHOS), while in low oxygen conditions cells rely mostly on glycolytic pathways for energy supply (Xia *et al*, 2021). Similarly, to tumors, in infectious diseases changes within the metabolic pattern occur in response to inflammatory stress signals in order to

satisfy the increased demand for rapid energy supply to sustain the infinite proliferation of cancer cells and the immune response, respectively. To obtain a much faster ATP production, activated cells perform glycolysis even in the presence of oxygen. This is known as aerobic glycolysis or Warburg effect (Xia *et al*, 2021).

1.7.1. Extracellular flux analysis

Extracellular flux analysis using the Seahorse XF analyser technology is crucial to characterize the metabolic phenotype of cells, including immune cells, and to highlight several features of their bioenergetic activity. This analysis consists in the simultaneous measurement of the main metabolic pathways involved in the inflammatory response, which are OXPHOS and glycolysis (Voss *et al*, 2021). To obtain this, fibre-optic probes with two sensors quantify the oxygen consumption rate (OCR) and the extracellular acidification rate (ECAR) over time, which correspond to changes in oxygen level and in pH of the medium, respectively. OCR is an indicator of oxidative phosphorylation and ECAR, mainly related to lactate production, is a read-out of glycolysis (Nicholas *et al*, 2017). Cells' immediate reactions to perturbations of their metabolic pathways can be monitored in real time thanks to the possibility to inject up to four compounds or mixtures including inhibitors into each well during the run (van der Windt *et al,* 2016; Pelgrom *et al*, 2016). Phorbol 12-myristate 13-acetate (PMA) and ionomycin are commonly injected to examine T cell metabolic capacity and adaptation upon activation. An advantage of Seahorse technology is that starting from few cells seeded in single wells, it efficiently identifies changes in many mitochondrial functions including basal respiration, proton leak, maximal respiration, ATP production, spare respiratory capacity, and non-mitochondrial respiration (Nicholas *et al*, 2017).

1.7.1.1. Glycolytic rate assay and glycolysis stress test

The glycolytic rate assay and glycolysis stress test are the chosen tests for the assessment of glycolytic activity. In glycolysis stress assay, samples are first equilibrated under glucose-starvation conditions. Then, glucose is injected to measure basal glycolytic activity in response to glucose availability. Next, to assess the glycolytic capacity (maximal glycolysis), oligomycin is injected to inhibit mitochondrial ATP synthase and push the use of glycolysis as the primary source of ATP. The capacity to shift metabolic activity to predominantly rely on glycolysis also informs on the metabolic flexibility of the cell. Last, 2-deoxy-D-glucose (2-DG) is injected to inhibit glycolysis and confirm that

ECAR measurements reflect glycolytic activity. Although ECAR quantifies the degree of media acidification, mainly due to glycolytic activity (lactate production), the CO_2 generated by OXPHOS can readily hydrolyse into bicarbonate and subsequently acidify the medium, thereby confounding ECAR results. The glycolytic rate assay can better distinguish between glycolytic and mitochondrial acidification producing a more specific and reliable read-out of glycolysis. Similar to the glycolysis stress test, the glycolytic rate assay quantifies basal and maximal, glycolytic activity, notably in presence of glucose (Voss *et al*, 2021).

1.7.1.2. Mitochondrial stress test

Mitochondrial stress test is the best assay to explore mitochondrial metabolism in cells that use OXPHOS as the main source of energy. The mitochondrial stress test can interrogate numerous aspects of mitochondrial biology, through sequential treatment of the sample with electron transport chain inhibitors. Following basal OCR measurements, oligomycin is injected to inhibit ATP production. Next, carbonyl cyanide-4-trifluoromethoxyphenylhydrazone (FCCP) is injected to depolarize the mitochondrial membrane and dissipate the proton gradient. This forces maximal electron transport chain activity to re-establish the electrochemical gradient necessary for mitochondrial function. This OCR measurement quantifies maximal respiration. The difference between maximal and basal OCR represents the spare respiratory capacity, also known as metabolic fitness, that means the energy reserved for response to cellular stress. Finally, rotenone and antimycin A, which inhibit complex I and III respectively, are co-injected to shut down electron transport chain function. Altogether, the mitochondrial stress test characterizes the metabolic phenotype and assesses numerous parameters of mitochondrial function (Voss *et al*, 2021).

1.7.2. Flow cytometry and cell metabolism

Flow cytometry represents an invaluable tool to analyze the metabolic features of the immune landscape. The combination of metabolic with phenotypical, functional, and transcriptional features of immune cells allows to have an overall picture of the immune response, from which it is also possible to derive therapeutic strategies for the treatment of inflammatory disease. Several flow-cytometry assays can be used to study cell metabolism at different levels. It is well established that mitochondria are essential mediators of cell metabolism, and its morphology and functions

play crucial roles in a variety of immune functions. Mitochondria are present in all types of cells, both in those that rely on oxidative phosphorylation and in those that perform glycolysis for ATP synthesis. They are heterogeneous in size, shape, and number, depending on the metabolic requirement of the cells and tissue and they are responsible for the production of ROS and involved in the regulation of the principal cell biosynthetic pathways (Cossarizza *et al*, 2021). Mitochondrial (mt) dysfunctions have been observed in several diseases such as cancer (Wallace, 1999). Mt dysfunctions mainly include changes in mitochondrial membrane potential (mtmP), mt mass, and redox potential (Cossarizza, *et al* 2021; Cottet-Rousselle *et al*, 2011). All these features can be studied by flow cytometry using fluorescent probes that are specific for mitochondria and able to detect the mt state at a specific time point or its changes over time. Dyes for measuring mtmP in living cells are typically lipophilic cationic compounds that can cross membranes without binding them and accumulate in the mt matrix. Since hyperpolarized or depolarized mitochondria present a more or less negative mt matrix, respectively, hyperpolarized mitochondria accumulate more dye, whereas depolarized mitochondria accumulate less dye. The main probes used to assay mtmP includes dihexyloxacarbocyanine iodide (DiOC6) and rhodamine 123 (Rh123), which have been extensively used in flow cytometric studies. However, the high toxicity of the former and the rapid release of the latter form the cell strongly limit their use (Troiano *et al*, 1998; Salvioli *et al*, 1997).

Whereas there are small, nontoxic, cell-permanent monochromatic dyes that specifically monitor dynamic changes of mtmP, among them tetramethylrhodamine ethyl ester (TMRE) and tetramethylrhodamine methyl ester (TMRM). In healthy cells with functioning mitochondria the signal of accumulated TMRM and TMRE is bright. The loss of mitochondrial membrane potential determines a halt to TMRM and TMRE accumulation and the weakening of the signal or its loss from the mitochondria (Rossi *et al*, 2021). The most reliable probes for the detection of mtmP are carbocyanine dyes, in particular 5,5’,6,6’-tetrachloro-1,1’,3,3’-tetraethyl-benzimidazol-carbocyanine (JC-1) (Cossarizza *et al*, 1993). JC-1 is a dual-emission dye that when it forms aggregates emits an orange-red fluorescence, while upon mt depolarization becomes monomers and emits a green fluorescence (Reers *et al*, 1991). JC-1 has multiple advantages such as its wide applicability for different cell types and assay conditions and in multicolor panels thanks to its compatibility with other fluorescent probes (De Biasi *et al*, 2015). Measurement of mitochondrial mass can be obtained by using probes that bind specific mt molecules, so that the bigger the mt content, the greater the signal emitted by the probe. Examples are MitoTracker dyes that form covalent bonds with cysteine residues present in mt proteins (Cossarizza *et al*, 2021; Rossi *et al*,

2021). Another feature of mitochondrial metabolism that can be measured by flow cytometry is the production and release of ROS in living cells. Mt anion superoxide can be quantified by means of the fluorescent probe MitoSOX red mitochondrial superoxide indicator (MitoSOX). It permeates live cells and selectively targets mitochondria where it is rapidly oxidized by superoxide and emits a high fluorescent signal upon binding to nucleic acid (Robinson *et al*, 2006). Whereas hydrogen peroxide production can be measured by mitochondria peroxy yellow-1 (mitoPY1). MitoSOX and mitoPY1 have been tested by flow cytometry in several cell lines including cancer cells lines. It has also been reported the possible simultaneous use of MitoSOX and mitoPY1 in the same panel for the analysis of mt ROS in living cells (Gibellini *et al*, 2015).

1.7.3. RNA flow cytometry

Metabolism as well as other pathways that shape cellular phenotype and function is tightly regulated at a transcriptional and post-transcriptional level, thus a quantitative analysis of gene and/or protein expression may provide important information on the activation of specific metabolic pathways in different immune cell types under healthy or pathological conditions. To perform this analysis, two flow cytometry-based strategies have been recently developed. The first one is named Met-Flow and has been proposed by P. J. Ahl as the first method that could simultaneously examine multiple metabolic pathways at single-cell, protein level within a heterogeneous population. Met-Flow utilizes antibodies that bind proteins playing a crucial role in specific metabolic pathways. The expression level of these enzymes provides a picture of the activated metabolic state of a cell type (Ahl *et al*, 2020). However, some limitations may hinder the application of Met-Flow approach such as the shortage of antibodies specific for most intracellular enzymes, and the need to combine antibodies with intranuclear markers to identify certain cell types (Rossi *et al*, 2021). The second strategy is RNA flow cytometry and consists of different techniques for the analysis of selected mRNAs at the single cell level. As for proteins, also RNA molecules can be detected by one or more complementary probes. Since cell metabolism is regulated by a precise gene expression profile, RNA analysis becomes essential (Rossi *et al*, 2021). Standard techniques used for RNA analysis (i.e., real-time qPCR, microarrays, and RNA sequencing) have been joined by newly developed flow cytometry-based approaches that allow single-cell RNA detection from heterogeneous samples. These are the SmartFlare (EMD Millipore, Burlington, MA, USA) system and the Prime Flow (ThermoFisher Scientific, Waltham, MA, USA).

These methods allow multiparametric immunological studies by combining RNA detection with phenotypical analysis (Segundo-Val *et al*, 2016; Soh and Wallace, 2018). SmartFlare technology has been used for the characterization of tumor cell lines and pluripotent stem cells in different tissues (Banerjee *et al*, 2017; Lahm *et al,* 2015), whereas Prime Flow is mostly applied in immunological studies focused on metabolism. Prime Flow can simultaneously detect different types of target RNA (mRNA, microRNA, viral and long non-coding RNA) in combination with surface and intracellular/intranuclear staining. The simultaneous study of RNA and protein expression allows for a finer definition of the posttranscriptional mechanisms at the basis of cell functions (Rossi *et al*, 2021). An example of Prime Flow application was for the study of *PPARG*, *ACACB*, and *CPT1A* genes involved in fatty acid metabolism in intratumoral conventional $CD4^+$ T cells and Tregs (Pacella *et al*, 2018). In another case, it was possible to define the duration of incubation needed to initiate protein translation using Prime-Flow by simultaneously detecting at different time points both intracellular TNF protein and mRNA in monocytes following LPS stimulation (Venable *et al*, 2016). An important advantage of RNA flow cytometry is that it offers an alternative when the quantification of a protein is infeasible either because no quality antibody exists, or the epitope is not accessible (Soh and Wallace, 2018). This tool, then, makes it possible to study tumors at a single-cell level but taking into account sample heterogeneity (Rossi *et al*, 2021).

1.7.4. The novel SCENITH assay

Another method called SCENITH exists to determine the overall metabolic capacities and dependencies of multiple cell subpopulations by flow cytometry (Argüello *et al*, 2020). Protein synthesis (PS) is one of the most energy-consuming metabolic processes and is tightly coupled with ATP kinetics (Lindqvist *et al,* 2018). SCENITH offers a methodological opportunity to determine the PS levels as a measure of global metabolic activity. The principle of SCENITH is to incubate a given sample with different specific inhibitors of metabolic pathways. If a cell population is energetically dependent on the inhibited metabolic pathway, its ATP concentration will drop as well as its PS levels. PS levels are measured using puromycin, a drug whose incorporation is detected by direct immune-fluorescence with a specific anti-puromycin monoclonal antibody (Aviner, 2020; Hidalgo San Jose and Signer, 2019). SCENITH has several advantages, such as the fact that it can be performed on a very small number of cells and directly in whole blood, without the incubation of cells in culture media for a long time, thus excluding a possible effect of media on the metabolic

profile of cells. Moreover, SCENITH allows the simultaneously analysis of the phenotypic and metabolic profiles of heterogeneous cell populations at single-cell resolution using multiparametric flow cytometry (Argüello *et al*, 2020). The accessibility of SCENITH, due to the great availability of flow cytometers in research centres and hospitals, together with its sensitivity, single-cell resolution and stable readout, makes SCENITH a reliable method to study energy metabolism in several fields (Artyomov and Van den Bossche, 2020). SCENITH can be performed in blood and tissue samples to understand the functional state of immune cells that are at the basis of the heterogeneous responses of patients to immunotherapies (Argüello *et al*, 2020).

AIMS OF THE THESIS

COVID-19 is caused by SARS-CoV-2 infection, that triggers a complex and often exaggerated immune reaction that can worsen the course of the disease. As in all infections, an effective immune response against the virus requires the involvement of both innate and adaptive cells. Since innate immunity is the first line of defence against infections, it is important to understand the pathophysiological mechanisms that are triggered by both soluble molecules and cells belonging to innate immunity, and their contribution to the heterogeneity of COVID-19 disease. Previous data indicate that a dysregulated hyperactivation of innate immune cells, including monocytes and neutrophils, leads to a persistent inflammatory status that is involved in the immunopathogenesis of severe COVID-19.

Accordingly, the main objective of my studies was the identification of the role of innate immune cells, like monocytes and neutrophils, in triggering or maintaining the inflammatory status in COVID-19 disease.

Thus, using biological samples from patients with SARS-CoV-2 infection who had developed COVID-19 pneumonia, specific aims of the thesis were:

to clarify, at least in part, metabolism, phenotype, and functions of monocytes in peripheral blood;

to characterize the phenotype of peripheral blood granulocytes;

to find the relationships between the metabolism and the functionality of circulating neutrophils;

to identify soluble plasma markers that indicate the degree and quality of the activation of innate immunity, including cytokines, chemokines, and other soluble molecules.

2. METHODS

2.1. ANALYSIS OF MONOCYTES

2.1.2. Human samples

Patients with COVID-19 pneumonia were admitted at the University Hospital in Modena during the first months of the pandemic, between March and July 2020. After the clinical visits and evaluation of entry criteria, patients were included in the study. Besides, healthy individuals negative to SARS-CoV-2 nasopharyngeal swab were recruited from the University Hospital personnel during the same period and served as normal controls. Demographic data and clinicopathologic characteristics of each patient have been recorded and are reported in Table 1. For this part of the study, twenty-eight patients with COVID-19 pneumonia were enrolled. They had a median age of 63 years (range 37–89) and 68.9% were males. All patients were stratified as severe, according to the WHO definition of COVID-19 disease. The cohort of controls was formed by twenty-seven healthy subjects with a median age of 58 years (range 35-80) and 53% were males. All patients provided an informed consent for blood and clinical data collection according to the ethical protocol approved by the local Ethical (Area Vasta Emilia Romagna, protocol number 177/2020, March 10, 2020). All the experiments were conformed to the principles set out in the WMA Declaration of Helsinki and the Department of Health and Human Services Belmont Report.

2.1.3. Blood collection and PBMC isolation

Up to 20 ml of blood were collected from each patient and healthy control in vacuette containing ethylenediamine-tetraacetic acid (EDTA). Blood was immediately processed. Peripheral blood mononuclear cells (PBMCs) were isolated using ficoll-hypaque according to standard procedures (Cossarizza *et al*, 2021). Plasma was collected, centrifuged at 3,500 rpm for 15 minutes at 4°C, aliquoted and stored at -80°C until use.

2.1.4. Purification of monocytes and analysis of their bioenergetic status

Pure populations of monocytes ($CD14^+$) were magnetically obtained from PBMCs by positive selection using CD14 microbeads (Miltenyi Biotec), according to manufacturer's instructions. Briefly, in this method $CD14^+$ cells are magnetically labelled with CD14 MicroBeads. Then, suspension of PBMCs is loaded onto a MACS column (Miltenyi Biotec) which is placed in the magnetic field of a MACS Separator (Miltenyi Biotec). The magnetically labelled $CD14^+$ cells are retained within the column. The unlabelled cells run through; this cell fraction is thus depleted of $CD14^+$ cells. After removing the column from the magnetic field, the retained $CD14^+$ cells can be eluted as the positively selected cell fraction. OCR, ECAR and oxidative burst were quantified by using the Seahorse XFe96 Analyser (Agilent Technologies). OCR and ECAR are measured in live cells in real time in a multi-well plate. In particular, 400,000 monocytes/well were plated in triplicate in XFe96 cell culture microplates (Agilent Technologies) precoated with poly-L-lysine to interfere microbic proliferation. RPMI medium was replaced with 180 µL of DMEM XF base medium, pH 7.4 (Agilent Technologies) supplemented with 10 mM glucose, 1 mM pyruvate, and 2 mM glutamine (all from Agilent Technologies). Plates were incubated 30 minutes at 37°C and loaded into the Seahorse XFe96 Analyser. OCR was quantified at the beginning of the assay and after the sequential injection of 2 µM oligomycin, 0.5 µM FCCP and 0.5 µM of rotenone plus antimycin A (MitoStress Test kit, Agilent Technologies). The assay measures basal respiration, ATP-linked respiration, H^+ leak, maximal respiration, spare respiratory capacity, and non-mitochondrial respiration using modulators of cellular respiration. Respiratory parameters were obtained as indicated: basal respiration as baseline OCR; proton leak by subtracting OCR after oligomycin injection to basal OCR; ATP-linked respiration by subtracting the proton leak to the basal OCR; spare respiratory capacity as the difference between the maximal respiration and the basal respiration; maximal OCR by calculating the difference of antimycin plus rotenone rate from FCCP rate (Gibellini *et al,* 2018; De Biasi *et al*, 2019). Oxidative burst was quantified after the injection of PMA/ionomycin (Sigma Aldrich), used to increase intracellular calcium, and was determined by assaying the AUC from the tenth to thirteenth measurement.

2.1.5. Flow cytometry

To identify monocytes, the following procedure was performed. Freshly isolated PBMCs were stained with viability marker PromoKine 840 (PromoCell); then, samples were washed with FACS buffer (PBS, 2% FBS) and incubated with a mix of pre-titrated directly conjugated mAbs. The mix included the following: anti-CD14-APC, anti-CD16-AF488, anti-HLA-DR-PE-Cy7, anti-PD1-BV421, anti-TIM-3-BV785, anti-CD15-PE-Cy5, anti-CD11-PE-Cy5, anti-CCR2-BV605 (BioLegend), anti-CD38-BUV496, anti-CXCR3-BUV395 (Becton Dickinson), anti-PD-L1-PE (ThermoFisher Scientific). Samples were acquired by using CytoFLEX LX (Beckman Coulter). To identify circulating mature and immature monocytes, thawed PBMC were stained with LIVE-DEAD Aqua, anti-HLA-DR-PE-Cy7, anti-CD14-APC, anti-CD13-PE, anti-CD64-FITC. Table 2 reports mAbs clones, catalogue numbers, type of fluorochrome used, and mAbs dilutions. Mitochondrial mass was analyzed by staining cells with Mito-Tracker green (MT Green, ThermoFisher) (De Biasi et al, 2019). Mitochondrial membrane potential was analyzed by staining cells with JC-1 (ThermoFisher), as described (Cossarizza et al, 1993). Cells were acquired using Attune NxT Acoustic flow Cytometer (ThermoFisher).

2.1.6. In vitro stimulation of monocytes and intracellular cytokine staining

Thawed PBMCs were washed twice with complete culture medium (RPMI 1640 supplemented with 10% foetal bovine serum and 1% each of L-glutamine, sodium pyruvate, nonessential amino acids, antibiotics, 0.1 M HEPES, 55 lM beta-mercaptoethanol) plus 0.02 mg/ ml DNAse. PBMCs were stimulated for 4 hours at 37°C in a 5% CO_2 atmosphere with PMA (100 ng/ml) and Ionomycin (1 μg/ml) in complete culture medium. For each sample, at least 2 million cells were left unstimulated as negative control, and 2 million cells were stimulated. All samples were incubated with a protein transport inhibitor containing brefeldin A (Golgi Plug, Becton Dickinson). After stimulation, cells were stained with LIVE-DEAD Aqua (ThermoFisher) and surface mAbs recognizing HLA-DR- PE-Cy7, CD14-APC, and CD16-BV421 (BioLegend). Cells were washed with stain buffer, fixed, and permeabilized with the cytofix/cytoperm buffer set (Becton Dickinson) for cytokine detection. Then, cells were stained with previously titrated mAbs recognizing IFN-γ-FITC and TNF-BV605 (all mAbs from BioLegend). Samples were acquired on Attune NxT acoustic cytometer.

2.1.7. Transmission electron microscopy

Monocytes were isolated by using the Pan Monocyte Isolation kit (Miltenyi Biotech) and were immediately fixed with 2.5% glutaraldehyde (Electron Microscopy Sciences) in 0.1 M cacodylate buffer (pH 7.4) for 4 hours at 4°C, washed in 0.1 M cacodylate buffer, and post-fixed with 1% OsO4 in cacodylate buffer for 1 hours at 4°C. The cells were dehydrated by routine procedures (Martín-Montañez *et al*, 2019) and embedded in Epon 812 (Electron Microscopy Sciences). Ultrathin sections (60 nm) were obtained with diamond knife, mounted on copper grids, and stained with a mix of lanthanum salts, samarium triacetate, and gadolinium triacetate (TAAB Laboratories Equipment Ltd) and with Reynolds' lead citrate. The samples were examined with a FEI NOVA NanoSEM 450, and images were obtained using the STEM mode using Solid State Detector with voltage at 30 kV. Mitochondrial size parameters and mitochondrial shape descriptors were measured on 225 mitochondria (from CTR, n = 3; COVID, n = 3) for each experimental group by using ImageJ software (version 2.0.0). In particular, mitochondrial area, external perimeter, Feret's diameter (the longest distance between any two points of the mitochondrial external perimeter), aspect ratio (ratio between major and the minor axis of each mitochondrion), and two indexes of sphericity: circularity [$4\pi\cdot(\text{area})/(\text{perimeter}^2)$] and roundness [$4\cdot(\text{area})/\pi\cdot(\text{major axis}^2)$] were considered for the analysis (Errea et al, 2015). Data were expressed as mean ± SEM.

2.1.8. Quantification of cytokine plasma levels

The plasma levels of 10 molecules were quantified using a Luminex platform (Human Cytokine Discovery, R&D System, Minneapolis, MN) for the simultaneous detection of the following molecules: IL-6, TNF, IFN-γ, GM-CSF, PD-L1, IL-18, osteopontin (OPN), CCL2, CCL11, CXCL10, according to the manufacturer's instruction. Data in the scatter plots represent the mean of two technical replicates.

2.1.9. Statistical analysis

Flow Cytometry Standard (FCS) 3.0 files were imported into FlowJo software version X (Becton Dickinson) and analysed by standard gating to eliminate aggregates and dead cells, and to identify $CD15^+$, $CD11b^+$, HLA-$DR^{+,+/-}$, $CD14^+$ monocytes. Then, data from 3,000 monocytes per sample were exported for further analysis in R, by following a script that makes use of Bioconductor libraries and R statistical packages (CATALYST 1.12.2). The script is available at:

https://github.com/HelenaLC/CATALYST) (Nowicka *et al,* 2019). The platform FlowSOM was used to perform the meta-clustering (K=10). Data were subsequently displayed using Uniform Manifold Approximation and Projection (UMAP) (Becht *et al*, 2019). Data are represented as individual values, means, and standard errors of the mean. Variables were compared using Mann–Whitney test, and statistical analyses were performed using Prism 8.0 (GraphPad software Inc, La Jolla, USA). There was no randomization, since this is not a clinical trial but a case–control study that compares patients with COVID pneumonia vs. age- and sex-matched healthy donors.

Table 2.

Specificity	Dye	Clone	Manufacturer	Cat.	Lot	Dil. (µl)
PromoFluor-840	Maleimide	N/A	Promokine	PK-PF840-3-01	429P0-17	0.3
CD14	APC	63D3	Biolegend	367118	B262993	0.6
CD16	AF488	3G8	Biolegend	302019	B216866	0.6
HLA-DR	PE-CY7	L243	Biolegend	307616	B260010	0.3
PD-1	BV421	EH12.2H7	Biolegend	329920	B217577	2.5
TIM-3	BV785	F38-2E2	Biolegend	345032	B241706	5.0
PD-L1	PE	MIH1	ThermoFisher	12-5983-41	1998319	5.0
CD11b	PE-CY5	ICRF44	Biolegend	301308	B284850	2.5
CCR2	BV605	K036C2	Biolegend	357214	B253733	0.6
CD15	PE-CY5	W6D3	Biolegend	323014	B287884	2.5
CD38	BUV496	HIT2	Beckton Dickinson	564658	9067622	1.25
CXCR3	BUV395	1C6/CXCR3	Beckton Dickinson	565223	7283777	2.5
TNFα	BV605	MAb11	Biolegend	502936	B282176	3.75
IFNγ	FITC	B27	Biolegend	506504	B286029	2.5
CD64	FITC	10.1	ThermoFisher	CD6401	1707112A	5.0
CD13	PE	L138	BD	347406	0086623	5.0
LIVE/DEAD	AQUA		ThermoFisher	L34957A	2145055	1.25

Table 2**.** List of monoclonal antibodies and fluorochromes for the cytofluorimetric analysis of monocytes. Dil: dilution; Cat: category number; Lot: lot number.

2.2. ANALYSIS OF GRANULOCYTES

2.2.1. Human samples

Two cohorts of patients were used in this part of the study: the first one was used to investigate the role of neutrophils' metabolism in their function; the second to analyze the levels of cytokines, chemokines, and other soluble factors involved in the regulation of neutrophils. Demographic and clinical characteristics of the first cohort patients and healthy donors are reported in Table 4. Seventy-two patients with severe COVID-19 admitted at the University Hospital in Modena (Italy) in March-December 2020, were included in this study. They had a median age of 66 years (range 37–88), 67% were males. We recorded demographic data, clinical characteristics of patients, arterial blood gas analysis, and several blood parameters from each patient. All patients were stratified as severe (WHO Working Group, 2020). Besides, 45 healthy donors negative to SARS-CoV-2 nasopharyngeal swab were recruited from the University Hospital personnel during the same period and served as normal controls (median age 59 years; range 34–79 years; 52.5% were males). Demographic and clinical characteristics of the second cohort patients and healthy donors are also reported in Table 4. Sixteen patients with severe COVID-19 admitted at the University Hospital in Modena (Italy) in March-December 2020, were included in this study. They had a median age of 63 years (range 36–85), 90% were males. We recorded demographic data, clinical characteristics of patients, arterial blood gas analysis, and several blood parameters from each patient. All patients were stratified as severe, according to the WHO. Besides, 14 healthy donors negative to SARS-CoV-2 nasopharyngeal swab were recruited from the University Hospital personnel during the same period and served as normal controls (median age 55 years; range 50–61 years; 70.0% were males). The study protocol was approved by the local Ethical (Area Vasta Emilia Romagna, proto- col number 177/2020, March 10th, 2020). Informed consent was obtained from each subject and the experiments were conformed to the principles set out in the WMA Declaration of Helsinki and the Department of Health and Human Services Belmont Report.

2.2.2. Blood collection

Up to 20 mL of blood were collected from patients and healthy donors in vacuette containing EDTA (Cossarizza *et al*, 2021). Blood was immediately processed. Plasma was collected, centrifuged, and stored at −80°C.

2.2.3. Purification of neutrophils and analysis of their bioenergetic status

Neutrophils were isolated from peripheral blood by using the MACSxpress whole blood neutrophil isolation kit (Miltenyi Biotech), following manufacturer's instructions. When requested, neutrophils were stimulated in culture medium (RPMI 1640 supplemented with 10% fetal bovine serum and 1% each of L-glutamine, sodium pyruvate, nonessential amino acids, antibiotics), for 4 or 16 hours at 37°C in a 5% CO2 atmosphere, in the presence/absence of 10 ng/mL chetomin, in the presence/absence of 50 µM GPI. Neutrophils were purified from peripheral blood by using the MACSxpress whole blood neutrophil isolation kit (Miltenyi Biotec), according to manufacturer's instructions. OCR, ECAR, and oxidative burst were quantified by using the Seahorse XFe96 Analyser (Agilent Technologies). In particular, for respiration and oxidative burst, 250,000 neutrophils per well were plated in triplicate in XFe96 cell culture microplates (Agilent Technologies) precoated with poly-L-lysine. RPMI medium was replaced with 180 µL of DMEM XF base medium, pH 7.4 (Agilent Technologies) supplemented with 2 mM glutamine, 10 mM glucose, 1 mM pyruvate (All from Agilent Technologies). Plates were kept for 30 min at 37°C and loaded into the Seahorse XFe96 Analyser. OCR was quantified at the beginning of the assay and after the sequential injection of 2 µM oligomycin, 0.5 µM FCCP, and 0.5 µM of rotenone plus antimycin A (MitoStress Test kit, Agilent Technologies). Respiratory parameters were obtained as indicated: basal respiration as baseline OCR; proton leak by subtracting OCR after oligomycin injection to basal OCR; ATP-linked respiration by subtracting the proton leak to the basal OCR; spare respiratory capacity as the difference between the maximal respiration and the basal respiration; maximal OCR by calculating the difference of antimycin plus rotenone rate from FCCP rate. Oxidative burst was quantified after the injection of PMA/ionomycin (Sigma Aldrich) and was determined by assaying the AUC from the 10^{th} to 13^{th} measurement. For glycolysis, 250,000 neutrophils per well were plated in triplicate in XFe96 cell culture microplates precoated with poly-L-lysine. RPMI medium was replaced with 180 µL of DMEM XF base medium, pH 7.4, supplemented with 2 mM glutamine. Plates were kept for 30 min at 37°C and loaded into the Seahorse XFe96 Analyser. ECAR was quantified at the beginning of the assay and after the sequential injection of 10 mM glucose, 1 mM oligomycin, and 50 mM 2-deoxy-glucose (all from Glycolysis Stress Test, Agilent Technologies). Glycolysis was quantified by subtracting ECAR after glucose injection to the basal ECAR. Glycolytic capacity was calculated by subtracting ECAR after oligomycin injection to the basal ECAR. ECAR, prior to glucose injection, was referred to as non-glycolytic acidification. Concerning ECAR quantification in neutrophils treated

with different cytokines, alone or in combination, the following concentrations were used: TNF (25 ng/mL), IFN-γ (50 ng/mL), GM-CSF (25 ng/mL), IL-8 (10 ng/mL).

2.2.4. Flow cytometry

To identify neutrophils, the following procedure was performed. Venous blood was collected in EDTA. One hundred µl of whole blood were incubated for 20 minutes at room temperature with pretitrated amount of Human BD Fc Block (Beckton Dickinson) and then with a mix of pretitrated directly conjugated mAbs for the following 20 minutes. The mix included: anti-CD45-FITC, -CD15-APC, CD16-APC-Cy7, -CD11b-PE-Cy7, -CD63-BV421, -CD62L-BV605, -CD66b-PE, -CXCR2-PerCP-Cy5.5 monoclonal antibodies (all from Biolegend) (Cossarizza *et al*, 2021). Samples were washed and lysed by using BD FACS Lysing Solution. Samples were acquired by using Attune NxT acoustic Flow Cytometer (ThermoFisher). Table 5 reports mAbs titers, clones, catalog numbers, and type of fluorochrome used in the panel. The gating strategy is shown in Figures 7a and 7b.

2.2.5. Transmission electron microscopy

Neutrophils were isolated by using the MACSxpress whole blood neutrophil isolation kit (Miltenyi Biotech) and were fixed with 2.5% glutaraldehyde (Electron Microscopy Sciences) in 0.1 M cacodylate buffer (pH 7.4) and postfixed with 1% OsO_4 in the same buffer. Cells were dehydrated using a graded ethanol series and embedded in Epon 812 (Electron Microscopy Sciences) (Gibellini *et al*, 2020). Ultrathin sections (60 nm) were cut using a Leica Ultracut S ultramicrotome with a diamond knife and collected on copper grids. Sections were stained with a mix of lanthanum salts, samarium triacetate, and gadolinium triacetate (TAAB Laboratories Equipment Ltd.) and with Reynolds' lead citrate. Samples were examined with a FEI NOVA NanoSEM 450 in a STEM mode using a Solid State Detector with voltage at 30 kV.

2.2.6. RNA Extraction, reverse transcription, and real-time quantification

Total RNA was extracted from neutrophils by using the Quick- RNA miniPrep kit (Zymo Research) and cDNA was synthesized with the iScript complementary DNA synthesis kit (Bio-Rad Laboratories). The quantification of the gene expression was performed using the CFX96 Touch Detection System. The following prevalidated primer assays (all from Bio-Rad Laboratories) were used: RPS18 (Prime PCR Assay; identifier, qHsaCED0037454) as the reference gene, PYGL (identifier, qHsaCID0017715), PGM1 (identifier, qHsaCID0010801), GYS1 (identifier, qHsaCID0021048), UGP2 (identifier, qHsaCED0004261), HIF1A (identifier, qHsaCID0014755). Changes in gene expression were calculated through the delta–delta cycle method.

2.2.7. Intracellular glycogen quantification

Intracellular glycogen was quantified by using the Glycogen Assay Kit (Abnova) following manufacturer's instructions. In brief, glucoamylase hydrolyses the glycogen to glucose which is then specifically oxidized to produce a product that reacts with OxiRed 21 probe to generate colour (OD 570 nm). Samples and standards were incubated for 30 minutes at room temperature with the mix, containing hydrolysis enzymes. After the incubation, 50 µL of the reaction mix, containing OxiRed probe, was added to samples and standards. The reaction was incubated for 30 minutes at room temperature, protected from light, and then absorbance (OD 570 nm) was measured.

2.2.8. NET quantification

NET was measured by using the NETosis Assay Kit (Cayman Chemical) following manufacturer's instructions. Freshly isolated neutrophils were resuspended in prewarmed NET assay buffer, prepared according to manufacturer's instruction as follows: 300 mL of RPMI 1640 base medium with or without glucose (GIBCO Life Technologies Cat Nos. 21875034, 11879020), 3 gr Bovine Serum Albumine (Cayman Chemical), and 300 µL of 1 M Calcium Chloride (Cayman Chemical). Cells were plated in 24-well tissue culture-treated plates at a concentration of 1×10^6 cells/mL and stimulated to release NET with PMA with or without glycogen phosphorylase inhibitor (50 µM; Sigma Aldrich) and chetomin (10 ng/mL; Sigma Aldrich) for 4 h at 37°C. After stimulation, cells were washed twice to remove soluble neutrophil elastase that is not NET-associated and treated with S7 Nuclease (Cayman Chemical) for 15 min at 37°C to disrupt the NET. The supernatant was collected from each well and nuclease was inactivated by adding EDTA (500 mM) Assay Reagent

Solution (Cayman Chemical). After a centrifugation at 300 *g* for 5 minutes, supernatants were transferred to polypropylene tubes and stored at −20°C. Samples were then assayed for released neutrophil elastase.

2.2.9. Western blot

Total protein lysates were obtained using RIPA buffer (50 mM Tris, pH 7.5, 0.1% Nonidet P-40, 0.1% deoxycholate, 150 mM NaCl, 4 mM EDTA, and protease inhibitors cocktail). Samples were kept on ice for 30 min, then centrifuged at 15,000 *g* for 30 min at 4°C. Protein concentration was determined by Bradford assay (Bio-Rad Laboratories). Samples (40 μg) were separated in 8% Bolt Bis-Tris precast gels (ThermoFisher) and transferred onto nitrocellulose membranes (Bio-Rad Laboratories) by using methanol transfer buffer. Membranes were blocked with 5% Blotting-Grade Blocker (Bio-Rad Laboratories) and incubated overnight, at 4°C, with the following primary antibody: anti-β-Tubulin (1:1000; Sigma-Aldrich), anti-HIF-1α (1:1000; Novus Biologicals). Membranes were washed and incubated with the secondary antibodies, goat anti-mouse IgG (H+L)-HRP Conjugate and Goat Anti-Rabbit IgG (H+L)-HRP Conjugate (1:5,000; Bio-Rad Laboratories). Proteins were visualized by Clarity TM Western ECL Blotting Substrates (Bio-Rad Laboratories) and images were acquired by using a ChemiDoc MP (Bio-Rad Laboratories). Image Lab (version 6.1, Bio-Rad Laboratories) was used to perform densitometric analysis.

2.2.10. Quantification of plasma levels of MPO, EL, and MPO-DNA complexes

Plasma levels of MPO were quantified by using the human MPO instant ELISA kit (ThermoFisher), according to manufacturer's instructions. Plasma levels of EL were quantified by using the PMN (Neutrophil) elastase human ELISA kit (ThermoFisher), according to manufacturer's instructions. The quantification of plasma levels of MPO-DNA complexes was performed by using the anti-human MPO primary antibody (Human Myeloperoxidase DuoSet ELISA; R&D systems) as the capture antibody and a peroxidase-conjugated anti-DNA primary antibody (from the Cell Death detection ELISA; Roche) as the detection antibody, as previously reported (Middleton *et al*, 2020; Kano *et al*, 2016).

2.2.11. Quantification of cytokine plasma levels

The plasma levels of 21 molecules involved in neutrophils' regulation were quantified using a Luminex platform, according to manufacturer's instructions (Human Cytokine Discovery, R&D System, Minneapolis, MN). The following molecules were quantified: BAFF, CCL2, CCL3, CCL4, CCL20, CXCL1, CXCL2, CXCL10, fibroblast growth factor-β (FGF-β), granulocyte colony-stimulating factor (G-SCF), GM-CSF, IFN-γ, IL-3, IL-4, IL-6, IL-17, IL-18, IL-23, transforming growth factor (TGF)-α, TNF, vascular-endothelial growth factor (VEGF). Data in the scatter plots represent the mean of two technical replicates.

2.2.12. Reanalysis of single-cell RNA sequencing (scRNA-seq) data

The scRNA-seq data from BAL from patients with COVID-19 and from healthy donors were acquired from the Gene Expression Omnibus (GEO) database under the series number GEO: GSE145926, which contains 12 data of lung tissue generated using 30 V2 chemistry kit on Chromium Single cell controller (10x Genomics). Analysis was performed using Seurat version 3. Cells with less than 200 genes or more than 4000 genes, and cells with 25% mitochondrial RNA content were excluded from analysis. Using SCTransform function, each sample was normalized and the variables "nCount_RNA" and "percent.mito" were regressed out (Hafemeister *et al*, 2019). Then, the 3000 most variable genes were selected and used to integrate all 12 samples together to remove batch effect across samples (Stuart *et al*, 2019). Dimensionality reduction was performed using UMAP selecting the first 15 PCs, while the clustering resolution was selected using clustree package (Zappia *et al*, 2018). Differentially expressed genes (DEGs) of COVID-19 versus HD neutrophils were identified using FindMarkers function. A gene was considered significant with adjusted $p < 0.05$ and logFC > 0.5. Genes upregulated of at least 1.5-fold between neutrophils from COVID-19 and neutrophils from healthy controls were analyzed by using Enricher (Chen *et al*, 2013; Kuleshov *et al*, 2016).

2.2.13. Gene Ontology enrichment analysis

The list of upregulated genes obtained in Seurat, across mild and severe conditions, was used to perform Gene Ontology functional profile using group GO function of cluster Profiler package version 3.18.1 (Yu *et al*, 2012). The biological process (BP) was used as orthogonal ontology and specific GO Level parameter as 2. The upregulated gene list was also used to perform Reactome pathway over-representation analysis using default parameters of enrich Pathway function implemented within the ReactomePA package version 1.34.0 (Yu *et al,* 2016). Dotplot, networkplot, and heatplot functions were used to plot the results.

2.2.14. Analysis of the correlations among cytokines and clinical features

To identify possible correlations among the studied parameters, a table was designed containing: (i) plasma cytokines/chemokines/soluble molecules; (ii) clinical characteristics reported in Table 4. Pairwise correlations between variables were calculated and visualized as a correlogram using R function corrplot. Spearman's rank correlation coefficient was indicated by color scale; significance was indicated by $*p < 0.05$, $**p < 0.01$, and $***p < 0.001$. All variables were displayed using original order without applying any hierarchical clustering.

2.2.15. Statistical analysis

Flow Cytometry Standard 3.0 files were imported into FlowJo software version X (Becton Dickinson), and analyzed by standard gating to eliminate aggregates, doublets, flow instability to identify $CD45^+CD11b^+$ myeloid cells. Then, data from $CD45^+CD11b^+$ cells per sample were exported for further analysis in R, by following a script that makes use of Bioconductor libraries and R statistical packages (CATALYST 1.12.2). The script is available at: https://github.com/ HelenaLC/CATALYST) (Nowicka *et al*, 2019). The platform FlowSOM was used to perform the metaclustering (K=10). Data were subsequently displayed using UMAP (Becht *et al*, 2019). Data are represented as individual values, means and SEM. Variables were compared using Mann- Whitney test and statistical analysis were performed using Prism 8.0 (GraphPad software Inc, La Jolla, USA) (De Biasi *et al*, 2020a).

Table 5.

MARKER	FLUOROCHROME	CLONE	TITER	CAT	LOT	BRAND
CD45	FITC	HI30	1,25	304006	B293670	Biolegend
CD15	APC	HI98	5	301908	B270323	Biolegend
CD16	APC-CY7	3G8	1,25	302018	B295414	Biolegend
CD11b	PE-CY7	ICRF44	5	301322	B277016	Biolegend
CD63	BV421	H5C6	5	353030	B275650	Biolegend
CD62L	BV605	DREG-56	1,25	304834	B294598	Biolegend
CD66b	PE	6/40C	5	392904	B284868	Biolegend
CXCR2	PerCP-CY5.5	5E8/CXCR2	2,5	320718	B282003	Biolegend

Table 5. Monoclonal antibodies (mAbs) used for detecting the phenotype of granulocytes by flow cytometry.

3. RESULTS

3.1. DATA ON MONOCYTES

3.1.1. Demographic and clinical characteristics of patients

Demographic and clinical characteristics of 28 COVID-19 patients with pneumonia admitted at the University Hospital in Modena and of 27 healthy donors were initially collected. All parameters are reported in Table 1. The mean age of subjects included in the study was 63.0 (37–89) years for COVID-19 patients (68.9% men) and 58.0 (35–80) years for healthy donors (53.5% men). At admission most of the patients presented fever (79.3%), cough (69%), and dyspnoea (58.6%). Minor symptoms registered in few patients were malaise, myalgia, dysgeusia, diarrhea, and asthenia. Regarding clinical parameters, a very high mean concentration of D-dimer and of CRP were present: 2,783 ng/ml for D-dimer (range: 390–17,140; normal values: <250 ng/ml) and 10.7 mg/dl for CRP (range: <0.2–34.5; normal values: <1 mg/dl). In addition, total bilirubin, and lactate dehydrogenase (LDH) mean concentration registered were equal to 0.51 mg/dl (range: <0.3–1.19; normal values: 0.2–1.2 mg/dl) and 576.9 U/l (range: 245–1,022; normal values: 100–190 U/l) respectively. From these data it was possible to confirm the presence of a high systemic inflammation. Another relevant characteristic associated to disease severity was the increased neutrophil-to lymphocyte ratio (7.2) in COVID-19 patients if compared to healthy controls (Liu *et al*, 2020b; Merad and Martin, 2020). A normal range of NLR is between 1-2, the values higher than 3.0 and below 0.7 in adults are pathological. Improving the clinical course of the disease and reducing risk of mortality are associated with decline of NLR values below 7 (Zahorec *et al*, 2021).

3.1.2. Monocyte from COVID-19 patients displayed a compromised bioenergetic profile

To determine whether SARS-CoV-2 infection had an impact on the metabolic capacity of monocytes, the bioenergetic function of these cells purified from PBMCs of 13 COVID-19 patients and 12 healthy controls was first examined. Changes in dynamics of bioenergetic function were observed using Seahorse XF Analyzer (Figure 1a). OCR and ECAR were measured in real-time in live monocytes seeded in a 96 multi-well plate. OCR was measured under basal condition, and in response to mitochondria inhibitors: oligomycin (Oligo, 2 µM), FCCP (0.5 µM), and antimycin A plus

rotenone (Rot/AA, 0.5 μM). Monocytes from COVID-19 patients exhibited reduced basal and maximal respiration, reduced proton leak, and reduced spare respiratory capacity if compared to those from healthy controls (Figure 1a). The ability of such cells to maintain the maximal respiration was investigated by analyzing the area under the curve (AUC) of the OCR trace from the sixth to the tenth timepoint and was indicated as "maximal respiration kinetic range". Monocytes from COVID-19 patients displayed a reduced capacity to maintain maximal respiration, if compared to controls. A marked reduction of the spare respiratory capacity was also observed in COVID-19 monocytes, suggesting that in these cells the mitochondrial capacity to meet metabolic demands in stressing conditions was compromised. Basal ECAR was also reduced in monocytes (Figure 1a). Oxidative burst was measured in response to PMA-ionomycin (PMA/Iono, 1 μg/ml) and data indicated that when monocytes from patients were challenged, they had a defective respiratory burst if compared to healthy controls (Figure 1a).

Mitochondrial function can be assessed also by monitoring changes in mitochondrial membrane potential (MMP). Mitochondrial depolarization can be associated with various inflammatory and metabolic disorders due to changes in the structure and function of mitochondria (Tolstik *et al*, 2022). Monocytes' MMP was analyzed by staining cells with JC-1 and it was observed that the percentage of monocytes with depolarized mitochondria was increased in COVID-19 patients (Figure 1b). A decrease in mitochondrial potential can promote a decrease in the reserve respiratory capacity (Tolstik *et al*, 2022). Not only the percentage of cells with depolarized mitochondria, but also mitochondrial mass was increased in monocytes from COVID-19 patients *versus* controls (Figure 1c). These data demonstrated that both the oxidative and glycolytic metabolism were defective in COVID-19 monocytes, a condition that strongly resembles the "immunometabolic paralysis" observed in monocytes from patients with sepsis (Cheng *et al*, 2016).

3.1.3. Mitochondria in monocytes of COVID-19 patients exhibited ultrastructural rearrangements

Monocytes isolated from the PBMCs of COVID-19 patients were investigated by transmission electron microscopy to assess whether alterations in the bioenergetics were accompanied by mitochondrial ultrastructural changes. As reported in Figure 2a (panel "a" and "b") by representative electron micrographs of monocytes, cells from COVID-19 patients were characterized by an eccentric reniform nucleus (indicated as "N"), chromatin aggregates at the periphery, abundant endoplasmic reticulum, Golgi complex, and small granules within the

cytoplasm. In control cells, mitochondria exhibited well-formed cristae (panel “c”) and, depending on the functional state, more or less condensed matrix can be observed. Mitochondria of monocytes from COVID-19 patients are shown in panels “d” and “e”. These organelles were characterized by heterogeneous size (panels “d”). Moreover, a number of mitochondria displayed intact mitochondrial membranes but high degree of swelling with electron-lucent matrix (panel “e”). Mitochondrial area, perimeter, and Feret’s diameter were significantly higher in COVID-19 compared to healthy monocytes (Table 3). Regarding mitochondrial shape that was evaluated as aspect ratio, circularity, and roundness, significant changes in aspect ratio and roundness were detected in monocytes of COVID-19 patients, whereas no difference was observed for circularity (Table 3).

3.1.4. Monocytes from COVID-19 patients maintained the capacity to produce cytokines

To understand whether impairment of oxidative burst activity was related to changes in COVID-19 monocytes capability to produce cytokines, high-dimensional flow cytometry was used to quantify the percentage of cells able to produce *in vitro* cytokines involved in monocyte immune response. Based on the gating strategy reported in Figure 3a, monocytes were identified according to the expression of HLA-DR and CD14 and the percentages of those cells producing IFN-γ and TNF before and after stimulation with PMA/ionomycin was determined, in both COVID-19 patients and controls. It was found that cells from COVID-19 patients were still capable to produce cytokines (Figures 3b and 3c). A difference, even if not statistically significant, in the pattern of IFN-γ and TNF expression was also noticed. The proportion of unstimulated monocytes producing IFN-γ was slightly decreased in COVID-19 patients if compared to controls, whereas the proportion of those producing TNF was higher (Figure 3c). These unpredicted observations could suggest that an inflammatory response was dominant in monocytes from COVID-19 rather than a direct antiviral activity driven by the production of IFN-γ.

3.1.5. Different distribution of monocytes subsets and immune exhaustion

To understand whether alterations in the bioenergetics performance were associated with phenotypic alterations, the expression of several membrane markers was analyzed using polychromatic flow cytometry (Cossarizza *et al*, 2021). Monocyte subpopulations in patients and healthy donors were analyzed by two complementary methodologies. In the first, the classical approach based upon the two-dimensional recognition of a given cell type was used, followed by a first gate that was required to identify the population of interest, followed by sequential gates to identify other markers. Data obtained with this gating strategy were then analyzed by appropriate, non-parametric statistical tests, and represented in the figures as scatter plots with means and standard errors of the mean. In the second, it was performed an unsupervised analysis that uses the multidimensional information obtained by FlowSOM meta-clustering coupled to a dimension-reduction method such as the UMAP, as described (De Biasi *et al*, 2020b). Heat maps finally report statistical analysis. Four populations were identified by UMAP: classical monocytes (defined as $CD14^{+}CD16^{-}CD38^{+}CCR2^{+}$), intermediate monocytes expressing CCR2 (defined as $CD14^{+}CD16^{++}CD38^{+}CCR2^{+}$), intermediate monocytes not expressing CCR2 (defined as $CD14^{+}CD16^{++}CD38^{+}CCR2^{-}$), and nonclassical monocytes (defined as $CD14^{-}CD16^{++}CD38^{-}CCR2^{-}$) (Figure 4a). All subsets of monocytes expressed different levels of CXCR3, PD-1, and PD-L1 (Figure 4b). T cell immunoglobulin and mucin domain-containing protein 3 (TIM3) was almost unchanged (Figure 4b). Classical monocytes were 86.7% (median value) of total monocytes in CTR vs. 75.8% in COVID-19 patients. Intermediate monocytes expressing $CCR2^{+}$ were 2.4% in CTR and 10.9% in COVID-19 patients while those not expressing CCR2 were 2.7% in CTR vs. 4.4% in COVID-19 patients.

Nonclassical monocytes were 8.2% in CTR vs. 8.9% in COVID-19 patients (Figure 4b). COVID-19 patients display a different distribution of monocytes subsets if compared to CTR (Figures 4c and 4d). Results obtained by unsupervised approach were then confirmed by the classical analysis based on sequential gates (Figures 4e and 4f). In COVID-19 patients, a higher percentage of $PD\text{-}1^{+}$ and $PD\text{-}L1^{+}$ cells were present among total monocytes, as well as within different subsets (Figures 4g, 4h, and 4i). The number of molecules per cell was measured by the quantification of median fluorescence intensity (MFI), and it was observed that the expression of PD-L1 on monocytes from COVID-19 patients was also increased (Figures 4g and 4l). It is interesting to note that despite the heterogeneity characterizing circulating monocytes, inhibitory checkpoints, in particular PD-1 and PD-L1, were significantly over-expressed in all the three subsets of monocytes, while previous data revealed that PD-L1 was mainly expressed on nonclassical monocytes in peripheral blood (Bianchini

et al, 2019). Moreover, soluble PD-L1 was present at thigh concentration in plasma from COVID-19 patients, if compared to healthy controls (Figure 5a). Thus, even if in this study the expression of TIM-3 on monocytes from healthy controls and COVID-19 patients was similar, it is possible to hypothesize that also in these patients soluble PD-L1 and galactin-9 can engage their receptors on monocytes, as already described in sepsis and alcoholic liver disease, and promote immune exhaustion and paralysis (Markwick *et al*, 2015).

3.1.6. Presence of immature monocytes in peripheral blood of severe COVID-19 patients

Then, to further investigate the role of circulating monocytes in the highly inflamed environment related to COVID-19, plasma concentrations of cytokines and other mediators from COVID-19 patients and controls were quantified. Among mediators involved in monocyte regulation and migration, plasma levels of IL-6, TNF, IFN-γ, IL-18, CCL2, CCL11, GM-CSF, OPN, CXCL10 were quantified (Figure 5a). The presence of an abnormal inflammatory response in most COVID-19 patients was revealed, by the presence of high levels of IL-6, TNF, IFN-γ, IL-18 in plasma from COVID-19 patients. Plasma concentrations of IL-6, TNF, and inflammatory chemokines, including CCL2 (ligand of CCR2), CCL11, CXCL10 (ligand of CXCR3), and OPN, was indeed significantly higher in COVID-19 patients if compared to healthy donors. Noteworthy, GM-CSF concentration was also increased in COVID-19 patients if compared to controls (Figure 5a), suggesting the presence of emergency myelopoiesis in severe COVID-19 patients (Silvin *et al*, 2020). Emergency myelopoiesis is a well-known phenomenon, characterized by the mobilization of immature myeloid cells to restore functional immune cells. Based on the obtained results, the presence of immature monocytes in peripheral blood was investigated. The gating strategy that was applied is reported in Figure 6, and by it, monocytes were first identified, according to physical parameters, then doublets and dead cells were removed. HLA-DR$^+$ cells were selected and among these, mature monocytes were identified as CD14$^+$CD13$^+$CD64$^+$ cells, while CD14$^-$CD13$^-$CD64$^-$ events were identified as immature monocytes. As expected, immature monocytes were significantly increased in peripheral blood from COVID-19 patients (24.01% ± 8.10 vs. 6.51% ± 0.85) (Figure 5b).

Table 1.

Variable	COVID-19 patients (n=28)	Healthy controls (n=27)
Age (mean yr, range)	63.0 (37-89)	58.0 (35-80)
Sex (M,%)	68.9	53.5
Symptoms		
Fever (%)	79.3	
Cough (%)	69.0	
Dyspnoea (%)	58.6	
Myalgia (%)	34.5	
Dysgeusia (%)	6.9	
Arthralgias (%)	10.3	
D-dimer (mean, ng/mL)	2,783.0	< 250.0
Total bilirubin (mean, mg/dL)	0.51	0.2-1.2
LDH (mean,U/L)	576.9	100-190
CRP (mean, mg/dL)	10.7	< 1.0
Blood cell count		
Neutrophils (mean N/μL)	5,439	3,723
Lymphocytes (mean N/μL)	1,256	2,199
Monocytes (mean N/μL)	430	457
Platelets (mean $N*10^3/\mu L$)	224	303.6
Neutrophil-to-lymphocyte ratio (mean)	7.2	1.28

Table 1. Demographic and clinical characteristics of patients. LDH, lactate dehydrogenase; CRP, C-reactive protein.

Figure 1a.

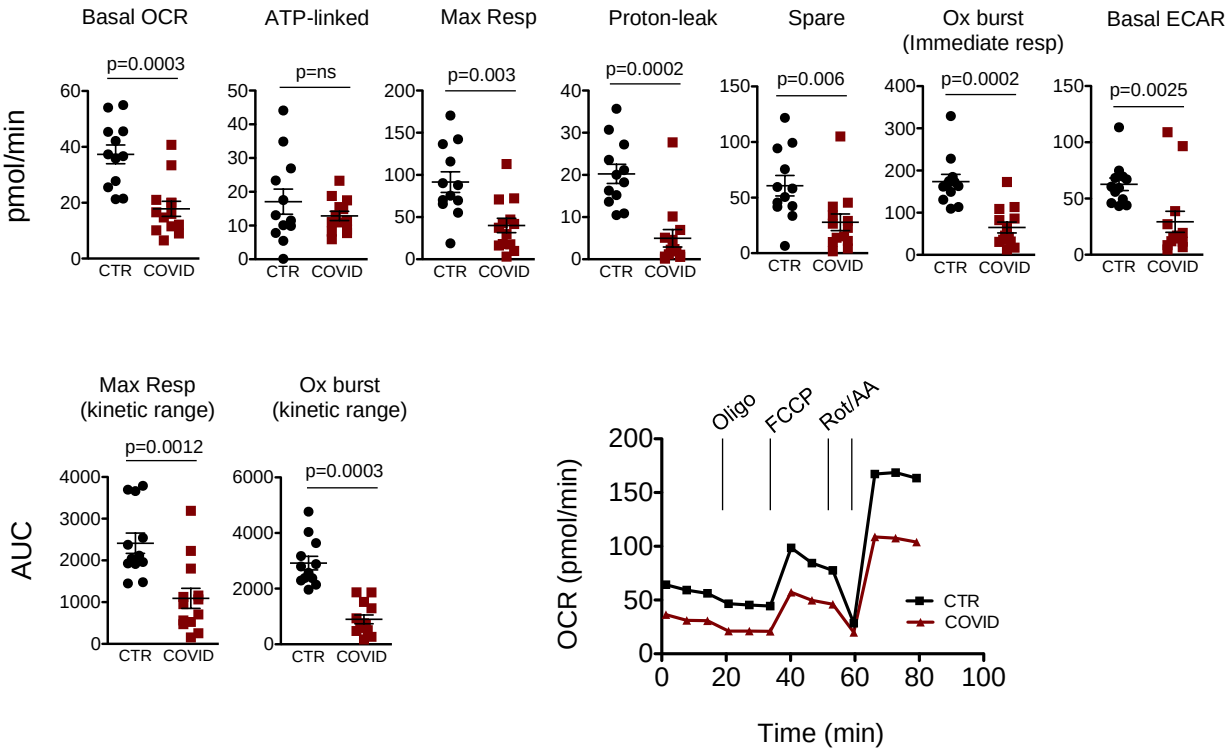


Figure 1a. Measurement of oxygen consumption rate (OCR), extracellular acidification rate (ECAR), and oxidative burst of monocytes from COVID-19 patients (COVID) and healthy controls (CTR). OCR was measured in real time, under basal condition, and in response to mitochondria inhibitors: oligomycin (Oligo, 2 µM), FCCP (0.5 µM), and antimycin A plus rotenone (Rot/AA, 0.5 µM). Oxidative burst was measured in response to PMA/ionomycin (PMA/Iono, 1 µg/ml). Scatter plots show the quantification of basal respiration (indicated as Basal OCR), ATP-linked respiration (ATP-linked), maximal respiration (Max Resp), proton leak, spare respiratory capacity (Spare), oxidative burst immediate response, and basal ECAR. The maximal respiration kinetic range and the oxidative burst kinetic range are also reported and were obtained by analyzing the area under the curve (AUC) from the sixth to the tenth measurement and from the tenth to the thirteenth measurement, respectively. Data represent individual values, mean and standard error of the mean (CTR, *n* = 12; COVID, *n* = 13). Mann–Whitney test was used for statistical analysis. Exact *P* values are reported in the figure. Representative traces of OCR of monocytes from COVID-19 patients (COVID) and healthy controls (CTR) are also reported.

Figure 1b.

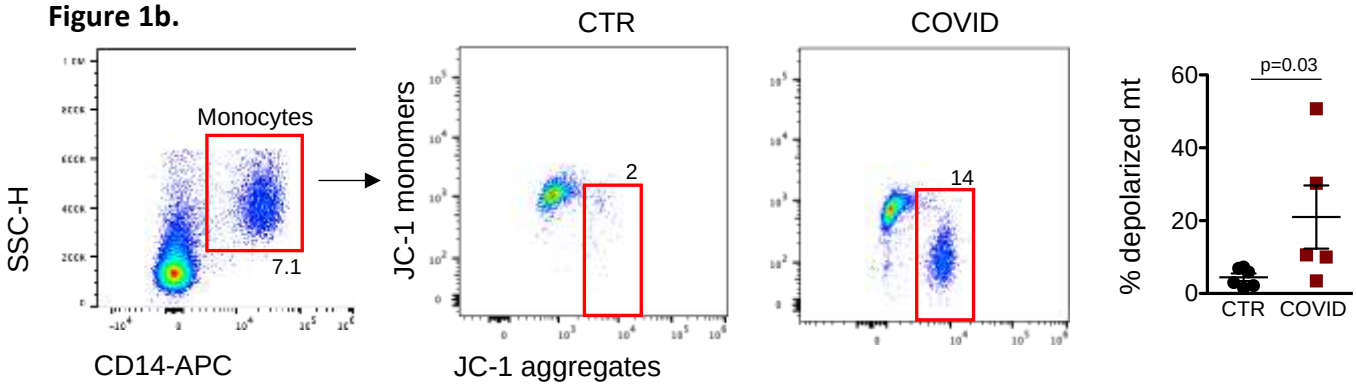


Figure 1b. Representative dot plots showing JC-1 monomers and aggregates in monocytes from COVID-19 patients (indicated as COVID) and healthy controls (CTR). The scatter plot on the right shows the quantification of cells with depolarized mitochondria. CTR, n=6; COVID, n=5. Mann-Whitney test was used for statistical analysis.

Figure 1c.

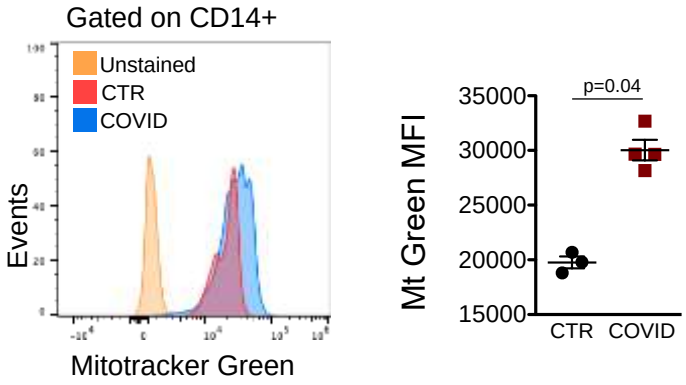


Figure 1c. Representative histograms showing Mitotracker Green (Mt Green) fluorescence in monocytes from COVID-19 patients (indicated as COVID) and healthy controls (CTR). The scatter plot on the right shows the quantification of Median Fluorescence Intensity (MFI) of Mt Green, as indicator of mitochondrial mass. CTR, n=3; COVID, n=4. Mann-Whitney test was used for statistical analysis

Figure 2a.

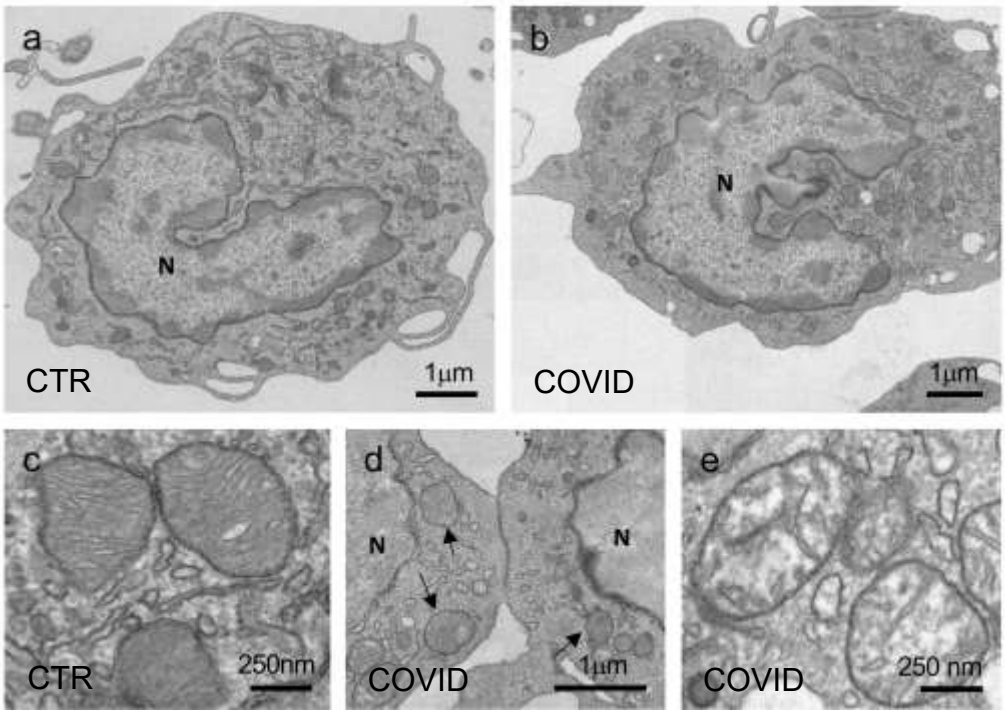


Figure 2a. Representative electron micrographs of mitochondrial ultrastructural changes observed in COVID-19 monocytes. Panels “a” and “c” are representative electron micrographs of monocytes from healthy controls, whereas panels “b”, “d”, and “e” are representative electron micrographs of monocytes from COVID-19 patients. Black arrows in panel “d” indicate mitochondria; N refers to nucleus.

Table 3.

Mitochondrial size parameters	CTR	COVID	p value	Mitochondrial shape descriptors	CTR	COVID	p value
Mitochondrial area (μm²)	0.09 ± 0.003	0.13 ± 0.01	0.001	Aspect ratio	1.40 ± 0.028	1.52 ± 0.06	0.042
External perimeter (μm)	1.09 ± 0.02	1.30 ± 0.05	0.0001	Circularity (0-1)	0.85 ± 0.005	0.84 ± 0.009	ns
Feret's diameter (μm)	0.41 ± 0.009	0.49 ± 0.02	0.0001	Roundness (0-1)	0.75 ± 0.01	0.72 ± 0.01	0.049

Table 3. The quantification of mitochondrial area, external perimeter, Feret’s diameter, aspect ratio circularity, and roundness are reported (*n* = 225 mitochondria for each group). Exact *P* values are reported.

Figure 3a.

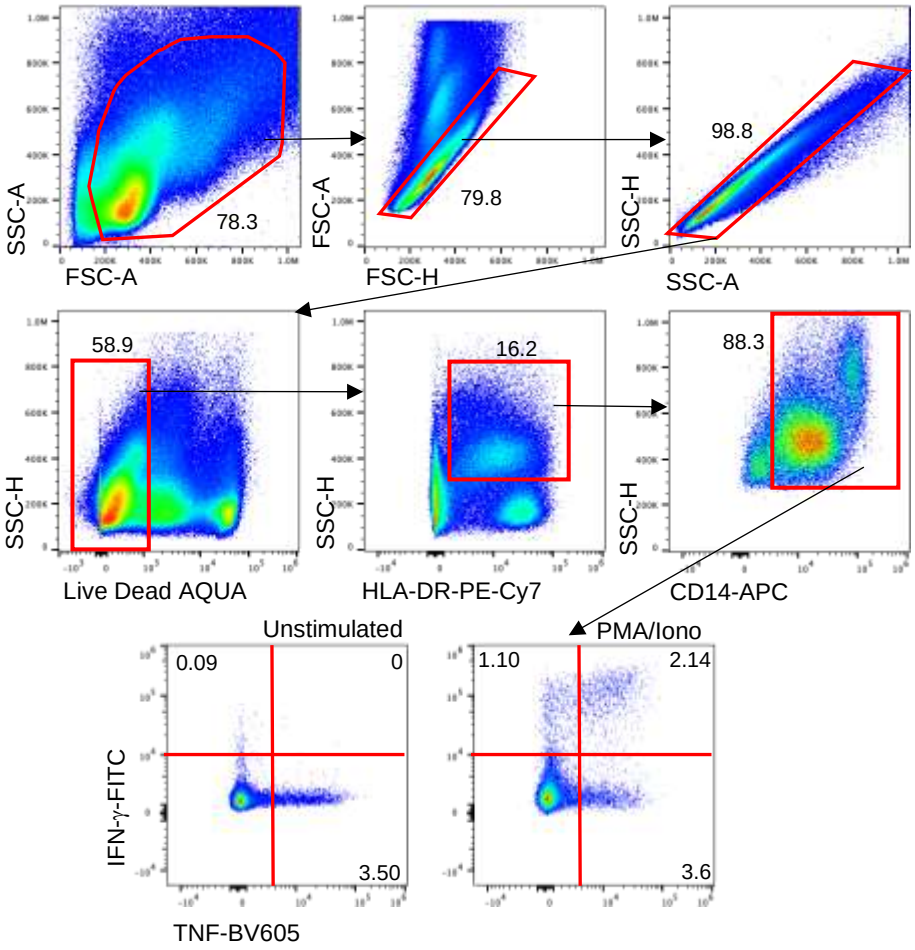


Figure 3a. Gating strategy for the identification of cytokine-producing monocytes after *in vitro* stimulation with PMA/Ionomycin (PMA/Iono). PBMCs were identified according to physical parameters; doublets and dead cells were removed. Monocytes were identified according to the expression of HLA-DR and CD14. The percentages of monocyte producing IFN-γ and TNF were evaluated before (indicated as unstimulated), and after stimulation.

Figure 3b.

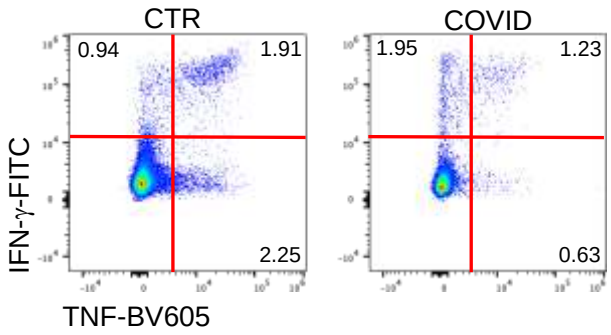


Figure 3b. Representative dot plots of monocytes producing cytokines after *in vitro* stimulation with PMA/Ionomycin in CTR and COVID patients

Figure 3c.

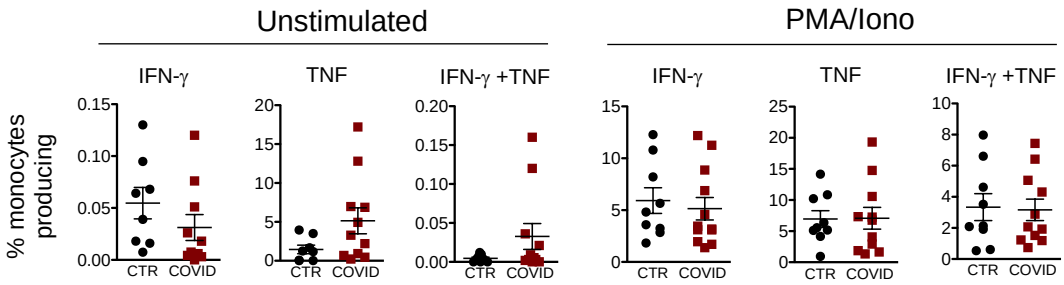


Figure 3c. Scatter plots reporting the quantification of monocytes producing IFN-γ, TNF or both cytokines in COVID-19 patients (COVID, n=8) and healthy controls (CTR, n=11), without any stimulus and after stimulation with PMA/ionomycin. Mann-Whitney test for used for statistical analysis, p=ns.

Figure 4a.

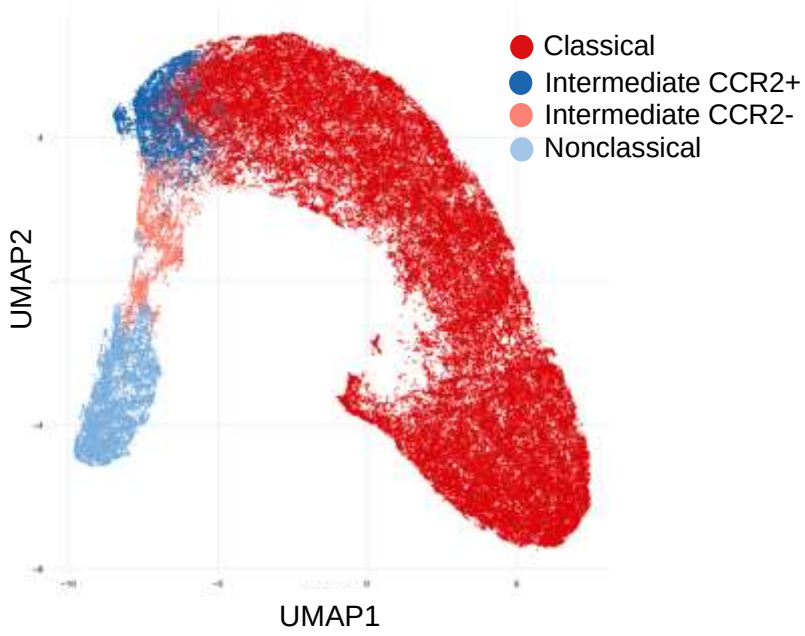


Figure 4a. Uniform Manifold Approximation and Projection (UMAP) representation of monocyte subpopulations.

Figure 4b.

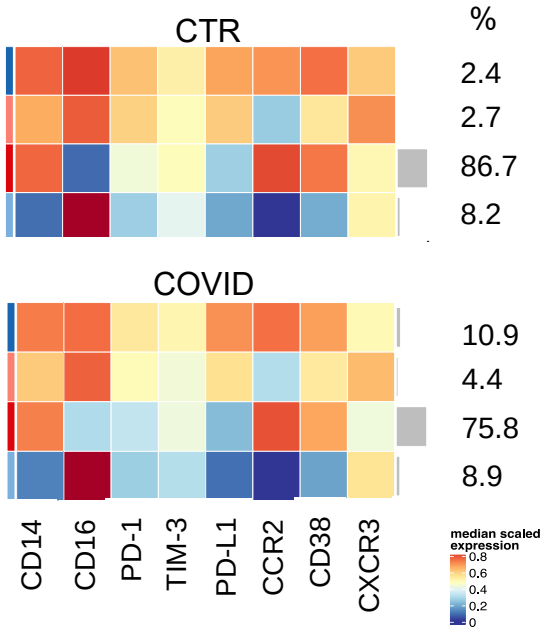


Figure 4b. Heatmaps representing different monocyte clusters identified by FlowSOM, with percentages in healthy donors (CTR) and COVID-19 patients. The colors in the heat map represent the median of the arcsinh, 0–1 transformed marker expression calculated over cells from all the samples, varying from blue for lower expression to red for higher expression. Each cluster has a unique color assigned (bar on the left which colors correspond to those used in Figure 4a).

Figure 4c.

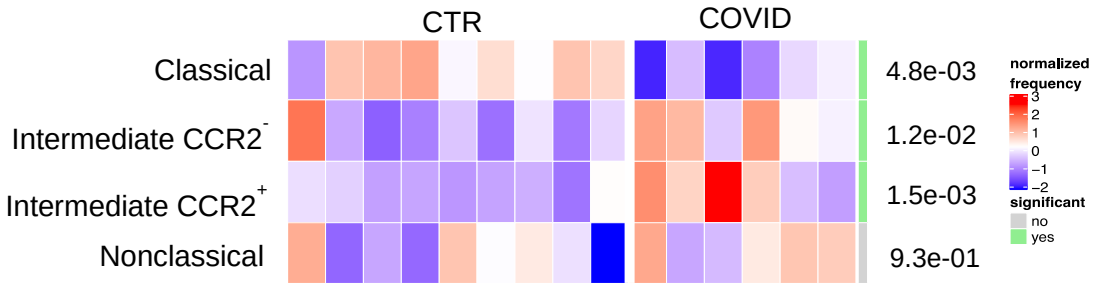


Figure 4c. Differential analysis between healthy donors (CTR, *n* = 8) and COVID-19 (COVID, *n* = 7). The heatmap represents arcsine-square-root transformed cell frequencies that were subsequently normalized per cluster (rows) to mean of zero and standard deviation of one. The color of the heat varies from blue, indicating relative under-representation, to red indicating relative over-representation. Bar and numbers at the right indicate significant differentially abundant clusters (green) and adjusted *P* values (Differential analysis performed by diffcyt package present in the Catalyst package). The statistical analyses were done using GLMM (according to the actual guidelines), and all *P* values were Bonferroni corrected. Clusters were sorted according to the adjusted *P* values, so that the cluster at the top shows the most significant abundance changes between the two conditions.

Figure 4d.

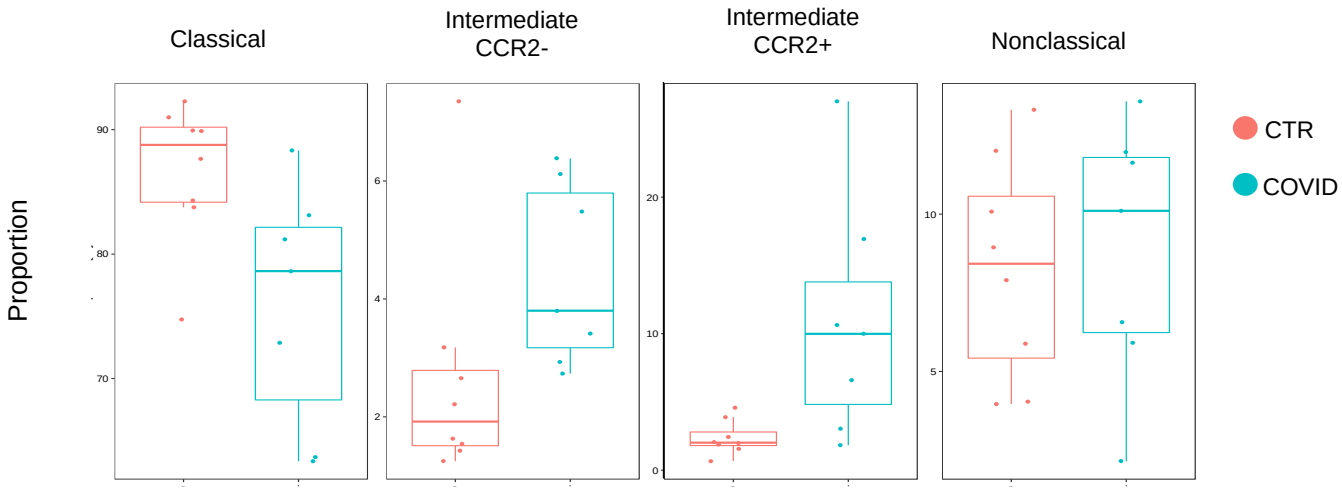


Figure 4d. Boxes and whiskers plots representing maximum, minimum, median value, 25 and 75 percentile of different subpopulations of monocytes in healthy donors (CTR, *n* = 8) and COVID-19 patients (COVID, *n* = 7).

Figure 4e.

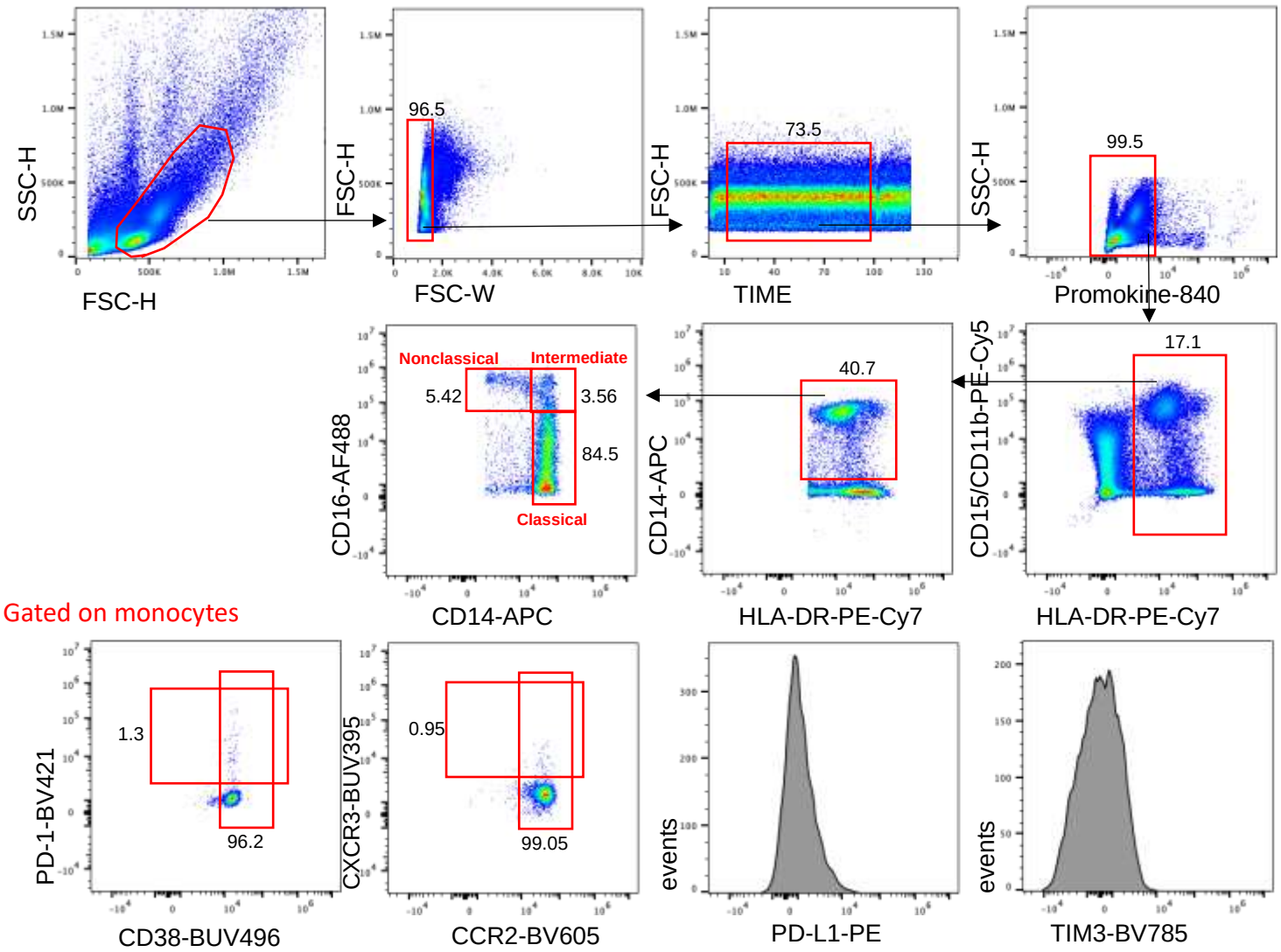


Figure 4e. The gating strategy for the identification of classical, intermediate, nonclassical monocytes expressing PD-1, PD-L1, and TIM-3 is reported. PBMCs were identified according to physical parameters, single cells were selected according to FSC-H and FSC-W gates, and the eventual turbulences of the flux present during acquisition were removed from the analysis, along with dead cells. Then, cells positive for HLA-DR, CD15 and CD11b were selected and monocytes expressing CD14 were identified. On the basis of the expression of CD14 and CD16, classical monocytes (defined as $CD14^{++}CD16^{-}$), intermediate monocytes (defined as $CD14^{++}CD16^{++}$), and nonclassical monocytes were identified (defined as $CD14^{-}CD16^{++}$). The expression of PD-1, PD-L1, TIM3, CXCR3, CCR2, and CD38 was evaluated in total monocytes and in the different subsets.

Figure 4f.

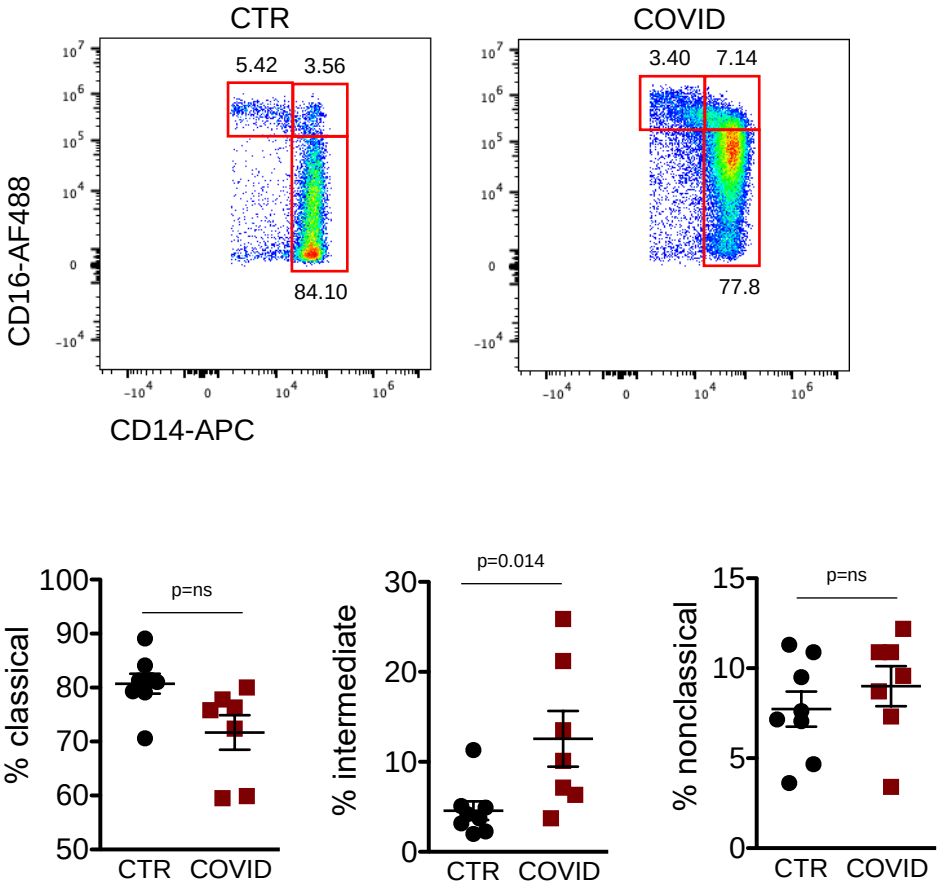


Figure 4f. Representative dot plots of the different subsets of monocytes, according to the expression of CD14 and CD16. Gates indicate classical ($CD14^{++}CD16^{-}$), intermediate ($CD14^{++}CD16^{++}$), and non-classical ($CD14^{++}CD16^{-}$) monocytes from one healthy control (CTR) and one COVID-19 patient (COVID). Scatter plots report the frequency of classical, intermediate and non-classical monocytes (CTR, n=8; COVID, n=7). Data represent individual values, mean and standard error of the mean. Mann-Whitney test was used for statistical analysis. The intermediate monocytes subset was expanded in COVID-19 *vs* controls (12.5±3.1% *vs* 4.5±1.04%, $p<0.05$), whereas the frequency of classical monocytes only tended to decrease (80.7±1.8% *vs* 71.7±3.2%, p= not significant). No obvious differences were found concerning the expression of CCR2, CXCR3 and CD38.

Figure 4g.

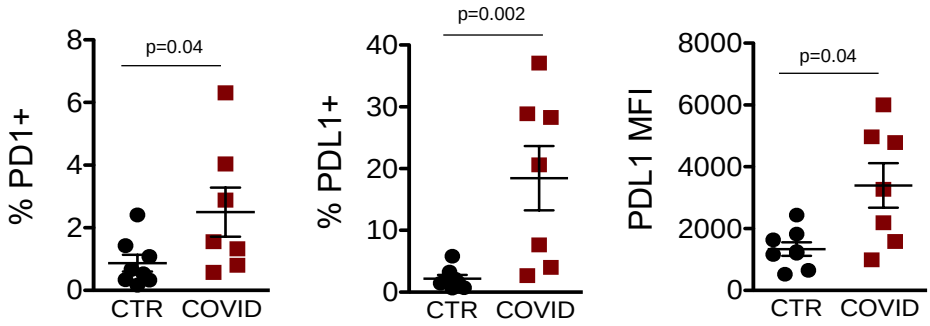


Figure 4g. Scatter plots showing the frequency of PD-1$^+$ cells, PD-L1$^+$ cells among total monocytes in healthy controls (CTR, *n* = 8) and COVID-19 patients (COVID, *n* = 7). A scatter plot reporting the median fluorescence intensity (MFI) of PD-L1 in total monocytes is also shown. Data represent individual values, mean ± standard error of the mean. Mann–Whitney test was used for statistical analysis. Exact *P* values are reported in the figure.

Figure 4h.

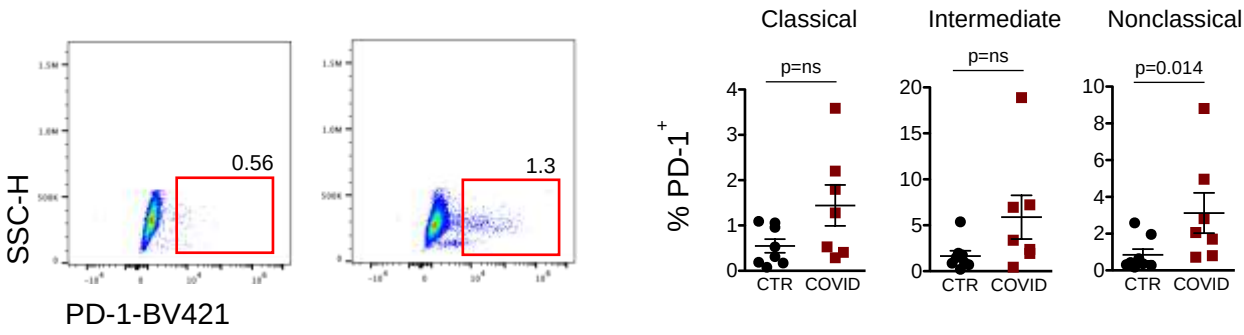


Figure 4h. Representative dot plots reporting the expression of PD-1 in classical monocytes from one healthy control (CTR) and one COVID-19 patient (COVID). Scatter plots report the frequency of PD-1$^+$ cells among classical, intermediate and nonclassical monocytes. CTR, n=8; COVID, n=7. Mann-Whitney test was used for statistical analysis.

Figure 4i.

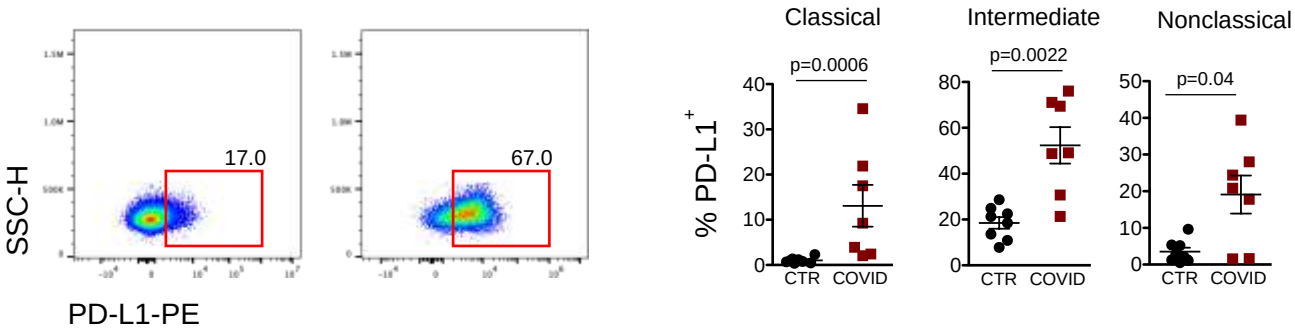


Figure 4i. Representative dot plots reporting the expression of PD-L1 in intermediate monocytes from one healthy control (CTR) and one COVID-19 patient (COVID). Scatter plots report the frequency of PD-L1^{+} cells among classical, intermediate and nonclassical monocytes. CTR, n=8; COVID, n=7. Mann-Whitney test was used for statistical analysis.

Figure 4l.

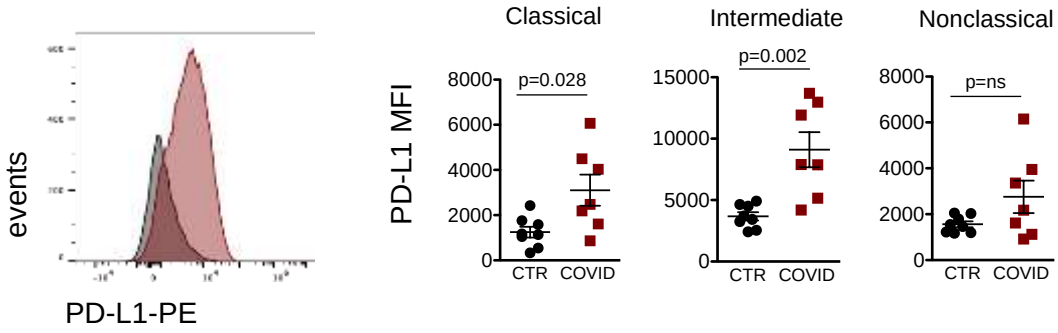


Figure 4l. Representative histogram reporting the expression of PD-L1 in monocytes from one healthy control (in grey) and one patient (in red). Scatter plots indicate the quantification of PD-L1 median fluorescence intensity (MFI) in classical, intermediate and nonclassical monocytes. CTR, n=8; COVID, n=7. Mann-Whitney test was used for statistical analysis.

Figure 5a.

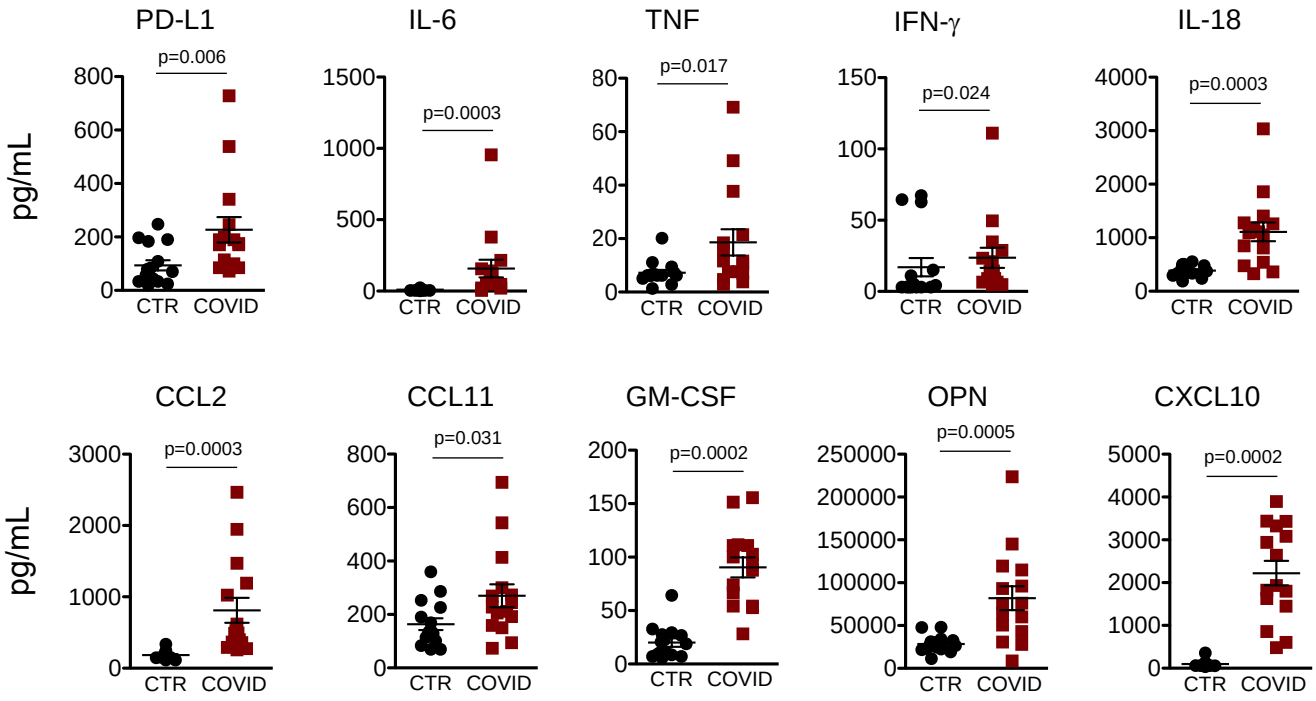


Figure 5a. Quantification of cytokines and other mediators in plasma obtained from COVID-19 patients (COVID, n = 15) and healthy controls (CTR, n = 15). Data represent individual values, mean±standard error of the mean. Mann–Whitney test was used for statistical analysis. Exact P values are reported in the figure.

Figure 5b.

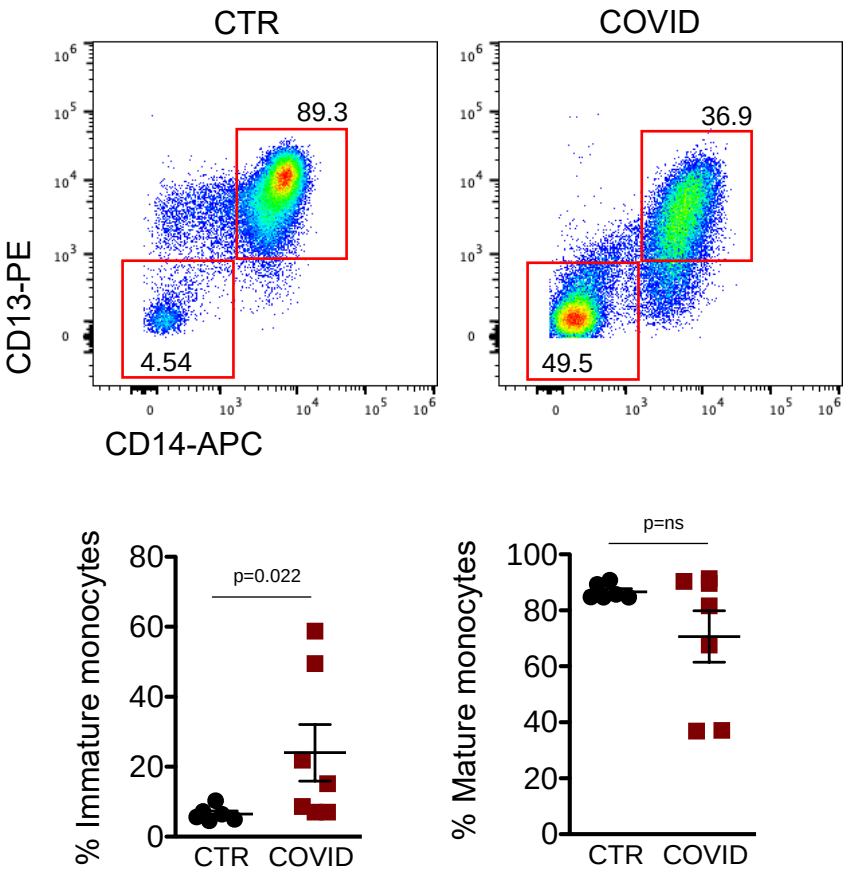


Figure 5b. Representative dot plots showing percentages of immature and mature circulating monocytes in CTR and COVID-19 patients. Scatter plots showing the quantification of immature and mature monocytes in healthy controls (CTR, n = 6) and COVID-19 patients (COVID, n = 7) are reported. Mann–Whitney test was used for statistical analysis. Exact P values are reported in the figure.

Figure 6.

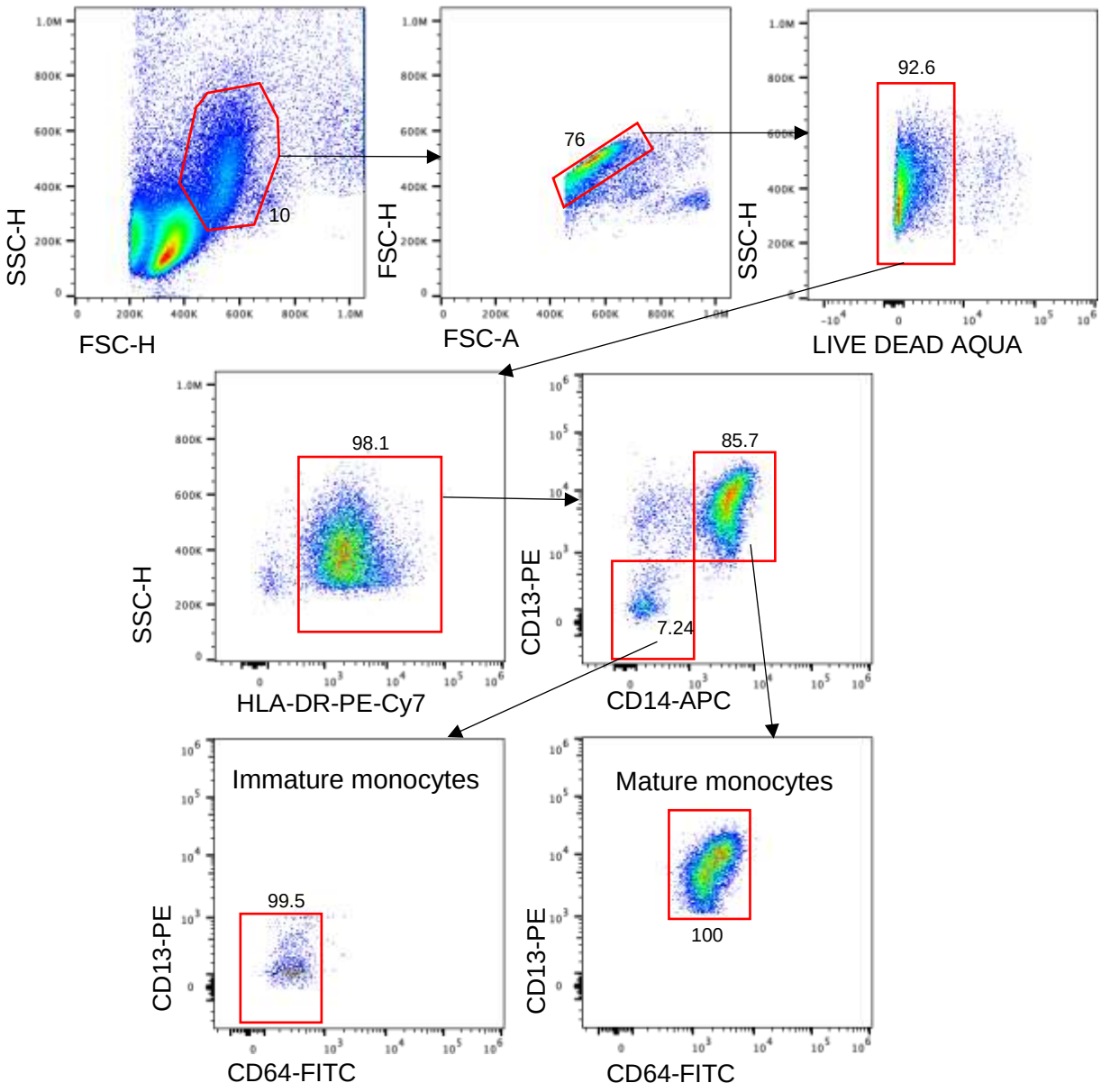


Figure 6. The gating strategy for the identification of immature monocytes is reported. Monocytes were identified according to physical parameters, doublets and dead cells were removed. HLA-DR$^+$ events were selected and among these, CD14$^+$CD13$^+$CD64$^+$ events were identified as mature monocytes and those CD14$^-$CD13$^-$CD64$^-$ were identified as immature monocytes.

3.2. DATA ON GRANULOCYTES

3.2.1. Circulating granulocytes are altered in severe COVID-19 patients

High-dimensional flow cytometry was initially used to characterize peripheral blood neutrophils, eosinophils, and basophils from patients with severe-COVID-19 pneumonia. Based on the selected gating strategy (Figure 7a), three populations of granulocytes were identified within the population of myeloid cells, according to the expression of CD16 and CD15. Basophils were classified as $CD15^{-}CD16^{-}$, eosinophils were $CD15^{+}CD16^{-}$, while neutrophils were $CD15^{+}CD16^{+}$. In this populations of granulocytes, the expression of important markers of neutrophil activation such as CD66b, CD63, CXCR2 and CD62L was analized (Figure 7b). Two different populations of $CD15^{+}CD16^{+}$ neutrophils were identified based on the expression of CXCR2 and represented by UMAP (Figure 8a), and the relative heatmap (Figure 8b). Among eosinophils two clusters of cells were identified, those $CD63^{+}CD62L^{+}$ and those $CD63^{+}CD62L^{-}$ cells. Finally, among basophils $CD63^{+}CD62L^{+}$ and $CD63^{-}CD62L^{-}$ cells were recognized. CXCR2 is a chemokine receptor involved in many inflammatory disorders, it has an important role in the trafficking of neutrophils in the inflamed site and it is a marker of cell maturity. The comparison between healthy donors and COVID-19 patients revealed that patients had a higher proportion of $CXCR2^{-}$ neutrophils, a phenotype associated to immature neutrophils presents in COVID-19 patients (Schulte-Schrepping *et al*, 2020; Silvin *et al*, 2020) (Figure 8c). Moreover, patients had a higher proportion of $CD63^{+}CD62L^{-}$ eosinophils compared to controls (Figure 8c).

Regarding basophils, no differences were detected among the two clusters, when comparing COVID-19 patients to healthy donors, but a higher proportion of degranulated basophils and neutrophils expressing CD63 was present in COVID-19 patients (Figures 8d,8e). No difference was detected in $CD63^{+}$ eosinophils between patients and controls (Figure 8d). The propensity of these cells to release their granule proteins is associated to priming mechanisms, the increase of degranulation in neutrophils from severe COVID-19 indicates that they are facing an inappropriate or excessive activation. Plasma levels of MPO and EL, two enzymes contained in neutrophil granules were quantified. It was found that MPO levels were highly increased in COVID-19 patients (mean ± SEM: 0.01±0.0001 in controls vs. 38.23±7.7 ng/mL in COVID-19 patients), and EL was almost undetectable in controls, but it was present at elevated concentrations in patients (mean ± SEM: 0.0009±0.0000014 ng/mL vs. 0.05±0.01 ng/mL) (Figure 8f). Notably, MPO and EL localize to NET, the net-like structures composed of DNA-histone complexes and proteins released by activated

neutrophils (Masucci *et al*, 2020), whose formation increases in COVID-19 patients (Radermecker *et al*, 2020; Veras *et al*, 2020). Therefore, to assess COVID-19-related NET formation and to quantify NET levels in plasma, plasma MPO-DNA complexes were also measure and it was observed that complexes were significantly increased in plasma of COVID-19 patients if compared to healthy donors (mean ± SEM: 0.000011 ng/mL vs. 8.175±2.78 ng/mL) (Figure 8f).

3.2.2. Circulating neutrophils displayed a remodeled metabolism

COVID-19 patients with severe pneumonia suffer from hypoxia, the condition generated by an inadequate oxygen availability that determines an imbalance between O_2 delivery and uptake and that is a relevant factor in COVID-19 progression (Osuchowski *et al.* 2021). Demographic and clinical data of each patient were recorded, including arterial blood gas values such as pO_2, sO_2, pO_2/FiO_2 and blood parameters. Data are all reported in Table 4. Notably, patients with severe COVID-19 had low blood levels of pO_2, and sO_2, and a low $pO_2/F\,iO_2$ ratio, delineating a typical profile of marked hypoxemia (Figure 9a and Table 4). Exposure to hypoxia quickly induces granulocytosis and the increased leukocyte count in deceased COVID-19 patients is caused by increased neutrophil count (Hitomi *et al*, 2003; Grieb *et al*, 2021). Considering that increased neutrophil-to-lymphocyte ratio and neutrophilia are indicators of disease severity and predictors of mortality (Du *et al,* 2020), the role of hypoxia in neutrophils regulation was investigated by the analysis of HIF-1α expression. HIF-1α is the main regulator of cellular adaptation in hypoxic conditions and its protein expression was indeed increased in neutrophils from COVID-19 patients (Figure 9b).

However, a reduction in the mRNA expression level of HIF-1A was observed, indicating that HIF-1α protein was stabilized at the post-translational level (Figure 9c). Hydroxylation is the main post-translational modification regulating oxygen-dependent HIF-1α degradation. In humans, HIF-1α hydroxylation is catalyzed by prolyl hydroxylase domain protein 2 (PHD2) that acts as a critical oxygen sensor (Berra *et al*, 2003). mRNA expression level of PHD2 were measured and it was found to be decreased in COVID-19 patients compared to controls (Figure 9c). Under hypoxic conditions, PHD2 is inhibited, so hydroxylation of HIF-1α slows down and HIF-1α subunits is stabilized (Gardie *et al*, 2014). Moreover, it was investigated whether HIF-1α was upregulated in neutrophils infiltrating lungs of SARS-CoV-2 infected patients. A publicly available single-cell RNA sequencing dataset obtained from bronchoalveolar lavage (BAL) of severe COVID-19 patients and healthy donors (scRNA-seq; GSE 145926) was interrogated (Bost *et al*, 2020). Within BAL several populations of leukocytes including neutrophils, macrophages, DCs, T cells and NK cells were

present (Figure 9d). Gene expression of *FCGR3B*, encoding for CD16b was used to identify neutrophils among different subsets (Figures 9d and 9e). In this analysis, a total of 3,971 cells (215 from healthy donors, 50 from mild COVID-19 patients, and 3,706 from severe COVID-19 patients) were considered. The comparison between neutrophils from healthy donors and COVID-19 patients identified 390 differentially expressed genes that were upregulated or downregulated at least 1.5-fold. 176 genes were upregulated in COVID-19 neutrophils and 214 were downregulated (Table 6). A twofold increase in HIF1A was observed in neutrophils from BAL obtained from COVID-19 patients (adjusted p-value 0.0006185) (Figure 9f and Table 6). In addition, Gene Ontology enrichment analysis revealed that differentially expressed genes in neutrophils from COVID-19 patients were strongly enriched for gene sets involved in IFN signalling and neutrophil degranulation, among others (Figures 9g and 10). Notably, several genes involved in mitochondrial functions, including *NDUFAB1*, *NDUFB2*, *ATP5ME*, *UQCRQ*, *NDUFA1*, and *COX6B1*, were downregulated in BAL neutrophils from COVID-19 patients if compared to healthy controls (Figure 9g, bottom panel).

Most of these genes encode for subunits of mitochondrial electron transport chain, therefore, indicating that oxidative phosphorylation could be impaired in these cells. If only upregulated genes are considered, those upregulated in BAL neutrophils from COVID-19 patients were enriched for gene sets involved in metabolic process, thus, suggesting that a profound metabolic remodeling occurs in these cells (Figure 11). Indeed, some regulators of cell metabolism, including *ATF3*, *GK*, *HIF1A*, *IDO1*, *IRF1*, *IRF7*, *ISG15*, *KLF6*, *NADK*, *SGK1*, *STAT1*, *STAT2*, *ZPF36* were upregulated in neutrophils from COVID-19 patients if compared with neutrophils from healthy donors (Figure 11 and Table 6). Among them, *ATF3*, *GK*, *HIF1A*, *ISG15*, *SGK1* are involved in glucose metabolism, glycogen metabolism, or gluconeogenesis (Gaspar and Velloso, 2018; Ku and Cheng, 2020; Mason *et al*, 2021); *NADK* is involved in oxidative metabolism (Hoxhaj *et al,* 2019).

3.2.3. Neutrophils rely on glycolysis for NET formation

In response to immunological challenges neutrophils utilize diverse metabolic pathways to fulfil their energy requirements, and to support specialized effector functions, such as NET formation, ROS generation, chemotaxis, and degranulation (Jeon *et al*, 2020). Glycolysis is a dominant metabolism in neutrophils. Neutrophils express various glucose transporters (GLUTs), such as GLUT1, GLUT3, and GLUT4 whose surface expression becomes increased after cell activation, also accompanied by an increase in the uptake of glucose. In fact, depletion of glucose totally shuts most effector functions of neutrophils (Jeon *et al*, 2020). Moreover, neutrophils have

relatively lower numbers of mitochondria than other immune cells and a lower basal OCR compared to monocytes or lymphocytes. This indicates that neutrophils are equipped with intact mitochondria but do not utilize them for energy production (Chacko *et al,* 2013). Differently, immature neutrophils depend on OXPHOS and FAO, have relatively higher numbers of mitochondria than mature neutrophils, and show an intact OCR activity (Rice *et al*, 2018). In inflammatory conditions, neutrophils show a larger accumulation of glycogen and under glucose-deprived conditions, neutrophils rely on glycogenolysis as an alternative source of glucose to perform their functions such as phagocytosis (Robinson *et al*, 1982; Weisdorf *et al*, 1982). Therefore, glycolysis seems to be a dominant and essential metabolic pathway for neutrophils.

In the study the bioenergetic profile of circulating neutrophils from COVID-19 patients and healthy donors was analyzed by the quantification of the extracellular flux (OCR and ECAR). It was found that neutrophils from healthy donors and COVID-19 patients had a low basal respiration as well as ATP-linked respiration (Figure 12a). Spare respiratory capacity was decreased in neutrophils from COVID-19 patients versus controls (Figure 12a). Uncoupling was also slightly different among the two groups. Monitoring OCR revealed that treating neutrophils from patients with PMA plus ionomycin caused a diminished respiratory burst (Figure 12a). In addition, the kinetic range of the maximal burst and the immediate response was investigated by calculating the AUC between the 10^{th} and the 13^{th} timepoint and by analyzing the OCR at the 11^{th} timepoint, respectively. The complete burst, as well as the immediate response, was decreased in neutrophils from COVID-19, thus, suggesting that cells from patients were less efficient in performing this function (Figure 12a). Neutrophils rely on glycolysis for NET formation (Lawrence Burn *et al*, 2021). Indeed, results indicated that both glycolysis and glycolytic capacity were strongly increased in neutrophils from COVID-19 (Figure 12b). A slight increase in non-glycolytic acidification was also observed. In line with this result, mRNA levels of GLUT1 and LDHA were strongly upregulated in neutrophils from COVID-19 patients (Figure 12c). Conversely, the mRNA level of glucose-6-phosphate dehydrogenase (G6PD) was similar between healthy controls and COVID-19 patients (Figure 12c), indicating that the pentose phosphate pathway was likely not engaged in these cells.

3.2.4. Pro-inflammatory cytokines trigger neutrophils metabolic rewiring in COVID-19 patients

To understand whether the increase in glycolysis could be due to simultaneous stimulation of neutrophils associated with the cytokine storm that is commonly observed in patients with severe COVID-19, neutrophils were isolated from healthy controls, and treated with cytokines (TNF, IFN-γ, GM-CSF, IL-8), alone or in combination. Then, ECAR was measured. The combinations of TNF+IFN-γ, TNF+GM-CSF, TNF+IL-8, IFN-γ+GM-CSF, TNF+IFN-γ+IL-8, TNF+IL-8+GM-CSF, IFN-γ+IL-8+GM-CSF, TNF+IFN-γ+IL-8+GM-CSF lead to increased glycolysis (Figure 12d) Enhanced glycolysis in neutrophils isolated from patients could represent an attempt of these cells to adapt to changes in their harsh environments where glucose and oxygen are lowly available, which could lead to the increased spontaneous NET formation.

3.2.5. Circulating neutrophils store glycogen, whose lysis is crucial for NET formation

In inflammatory conditions, neutrophils show a larger accumulation of glycogen that they can use as an alternative source of glucose by its breakdown through glycogenolysis (Jeon *et al*, 2020). Activities performed by neutrophils, as migration, chemotaxis, phagocytosis, and formation of NET are supported by the mobilization of stored glycogen (Robinson *et al*, 1982). Under hypoxia, HIF-1α regulates glycogen metabolism promoting its accumulation (Pescador *et al,* 2010). Neutrophils from COVID-19 and healthy controls were analyzed by transmission electron microscopy and huge amount of synthesized glycogen was found stored in the cytoplasm of COVID-19 neutrophils. Neutrophils from healthy donors (Figure 13a, panel “a”) and COVID-19 patients (Figure 13a, panels “b-d”) were characterized by several granules, typical segmented nuclei, scarce endoplasmic reticulum (ER), few mitochondria, and little Golgi complex. When present, glycogen particles were scarce and uniformly distributed throughout the cytoplasm in neutrophils from healthy donors (Figure 13a, insert of panel “a”). Conversely, in neutrophils from COVID-19 patients, glycogen particles appeared dramatically increased, forming large aggregates mainly located at the cell periphery in areas with a lower density of cytoplasmic organelles (Figure 13a, insert of panel “b-d”). Biochemical measurements of glycogen levels (Figure 13a, panel “e”) were performed using the Glycogen Assay Kit (Abnova). In agreement with ultrastructural results, intracellular glycogen was 3-fold higher in neutrophils from COVID-19 patients, if compared to intracellular glycogen in neutrophils from healthy donors (12.7±4.0 ng/μg protein in controls vs. 39.8±13.2 ng/μg protein in

COVID-19). mRNA expression of the master genes involved in glycogen metabolism was also analyzed. The analysis included phosphoglucomutase 1 (PGM1), which catalyses the transfer of phosphate between the 1 and 6 positions of glucose; UDP-glucose pyrophosphorylase 2 (UGP2), which is involved in glycogen synthesis together with glycogen synthase (GYS) 1 and GYS2; and glycogen phosphorylase L (PYGL), which catalyses glycogenolysis. GYS1 and GYS2 were almost undetectable, while PGM1, PYGL, UGP2 were expressed in neutrophils both from healthy donors and COVID-19 patients (Figure 13b). PGM1 was unchanged and UGP2 showed a tendency to increase, although this change was not statistically significant (Figure 13b). PYGL was upregulated in neutrophils from COVID-19 patients (Figure 13b).

3.2.6. Glycogenolysis is important for NET formation in COVID-19 patients

Neutrophils fuel effective immune responses through glycogenolysis (Sadiku *et al*, 2021). COVID-19 neutrophils' ability to spontaneously perform NET was analyzed in the presence or absence of CP-91149, a glycogen phosphorylase inhibitor. CP-91149 almost abrogated the capacity of neutrophils from COVID-19 patients to perform NET (Figure 13c). Conversely, neutrophils from healthy donors were not dependent on glycogenolysis (Figure 13c). The same tendency was noticed when cells were treated with chetomin, an HIF-1α inhibitor. However, no difference was detected when neutrophils were cultured in absence of glucose. To understand if HIF-1α could have a role in the regulation of glycogen phosphorylation, hypoxia-responsive elements (HRE) were searched in the 5'-flanking region of PYGL gene and two HRE were found (Figure 13d). Based on that, the expression of *PYGL in* neutrophils after the inhibition of HIF-1α by chetomin was studied. The obtained results could demonstrate that Inhibiting HIF-1α halved the expression of *PYGL* (Figure 13e), so HIF-1α could regulate glycogen metabolism through *PYGL*.

3.2.7. Cytokines and other soluble molecules regulating neutrophils' function are profoundly altered

In an independent cohort of 16 patients with severe COVID-19, the plasma levels of 21 cytokines, chemokines, and other molecules associated with the activation and recruitment of neutrophils were measured (Figure 14a). It was found that B-cell activating factor (BAFF), CCL2, CCL3, CCL20, CXCL10, G-CSF, GM-CSF, IFN-γ, IL-6, IL-18, VEGF, TNF were significantly higher in COVID-19 patients. CCL4, CXCL1, CXCL2, FGF-β, IL-3, IL-4, IL-17, IL-23, and TGF-α were unchanged. To get further insight, a principal component analysis (PCA) of cytokines/chemokines/soluble

molecules involved in neutrophils' regulation across the cohort was performed and it was found that the PC1 was mostly responsible for the stratification of COVID-19 patients and healthy donors (Figure 14b, upper part). A graph displaying the contribution of the different molecules on the principal components as arrows revealed that the most important contributors were the levels of BAFF, CXCL10, GM-CSF, CCL3, CCL4, and IFN-γ (Figure 14b, bottom part). A correlation map that included clinical data of COVID-19 patients revealed that: (i) the percentage of neutrophils correlated with plasma level of CCL4, CXCL1, CCL20, and IFN-γ; (ii) pO_2/FiO_2 correlated with plasma level of CCL20; (iii) sO_2 and pO_2 correlated with plasma level of CCL4 (Figures 15a and 15b).

Table 4. Demographic and clinical characteristics of COVID-19 patients and healthy donors.

Cohort	First		Second	
Variable	**COVID-19 (n=72)**	**HD (n=45)**	**COVID-19 (n=16)**	**HD (n=14)**
Demographic characteristics				
Age (mean years, range)	66.2 (37 – 88)	59 (34 – 79)	63 (36 – 85)	55 (50 – 61)
Sex (M,%)	67.0	52.5	90.0	70.0
Clinical characteristics				
Respiratory rate	22.3 (14 – 36)		23.2 (16 – 30)	
Heart rate	74.1 (48 – 120)		78.4 (60 – 112)	
Score			20.8 (3 – 41)	
NIV or high-flow, N (%)	43 (59.7)		12 (75.0)	
IMV, N (%)	29 (40.3)		4 (25.0)	
SOFA score, mean (range)	2.9 (1 – 6)		3.1 (1 – 7)	
Coexisting conditions				
Type 2 diabetes, N (%)	14 (26.4)		2 (12.5)	
Cardiovascular Dis., N (%)	32 (60.0)		4 (25.0)	
Obesity, N (%)	4 (7.5)		0	
Arterial blood gas analysis				
pO_2, mmHg (range)	66.3 (41.7 – 95.2)		66.0 (47.2 – 96.5)	
sO_2, % (range)	92.8 (82.0 - 97.8)		93.0 (85.9 – 97.8)	
pO_2/FiO_2 (range)	170.7 (53.0 – 338.0)		244.3 (95.0 – 421.0)	
Blood cell count				
Neutrophils, N/μL (range)	8,398 (1,020 – 29,120)		7,013 (3,052 – 20,152)	
Neutrophils (%)	80.9 (36.3 – 96.9)		77.4 (50.0 – 93.6)	
Lymphocytes, N/μL (range)	941.6 (120 – 2,390)		1,089 (735 – 2,051)	
Lymphocytes (%)	16.0 (3.4 – 45.7)		19.2 (5 – 61)	
Platelets, $N*10^3/\mu L$ (range)	233.1 (22 – 676)		199.6 (81 – 581)	
Neu-to-lymph ratio, (range)	13.4 (0.8 – 85.6)		7.0 (1 – 18.0)	
Blood parameters				
ALT, U/L (range)	72.2 (7 – 779)	19 – 33	55.5 (5 – 254)	19 – 33
Total bilirubin, mg/dL (range)	0.6 (0.3 – 1.5)	0.2 – 1.2	0.7 (0.3 – 1.1)	0.2 – 1.2
CK, U/L (range)	150 (20 – 908)	22 – 198	330.6 (20 – 904)	22 – 198
Creatinine, mg/dL (range)	1.3 (0.5 – 10.3)	0.59 – 1.35	1.3 (0.53 – 2.7)	0.59 – 1.35
D-dimer, ng/mL (range)	2,859 (100 – 33,740)	< 250	1,571 (510 – 3,430)	< 250
LDH, U/L (range)	708.5 (286 – 1,891)	100 – 190	770.3 (304 – 1,566)	100 – 190
CRP, mg/dL (range)	9.4 (0.2 – 41.9)	<1.0	15.1 (0.2 – 48.0)	<1.0

pCO2, partial pressure of carbon dioxide; pO2, partial pressure of oxygen; sO2, oxygen saturation; pO2/FiO2, fraction of inspired oxygen; ALT, alanine aminotransferase; CK, creatine kinase; LDH, lactate dehydrogenase; CRP, C-reactive protein; NIV, non-invasive ventilation; IMV, invasive mechanical ventilation; Dis, disease.

Figure 7a.

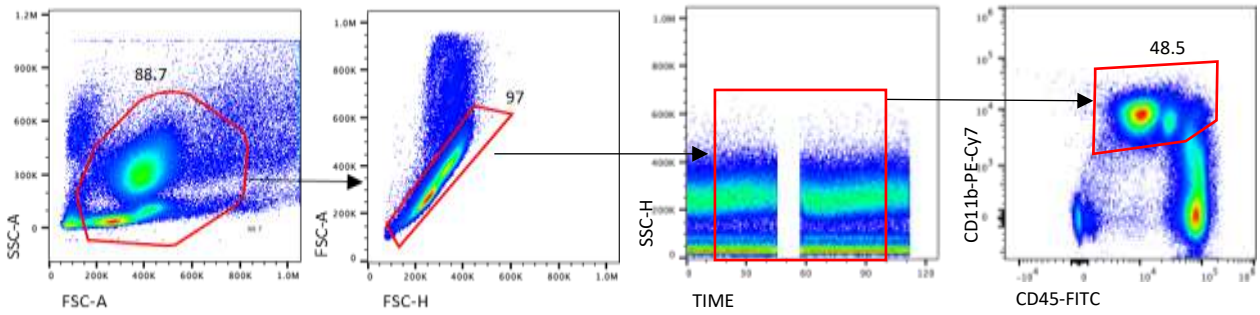


Figure 7a. The gating strategy for the identification of neutrophils, basophils and eosinophils. Nucleated cells were selected according to physical parameters, doublets were removed according to FCS-H vs FCS-A plot, instability during acquisition were removed according to time gate vs SSC-H. In this population, leucocytes expressing CD11b were selected.

Figure 7b.

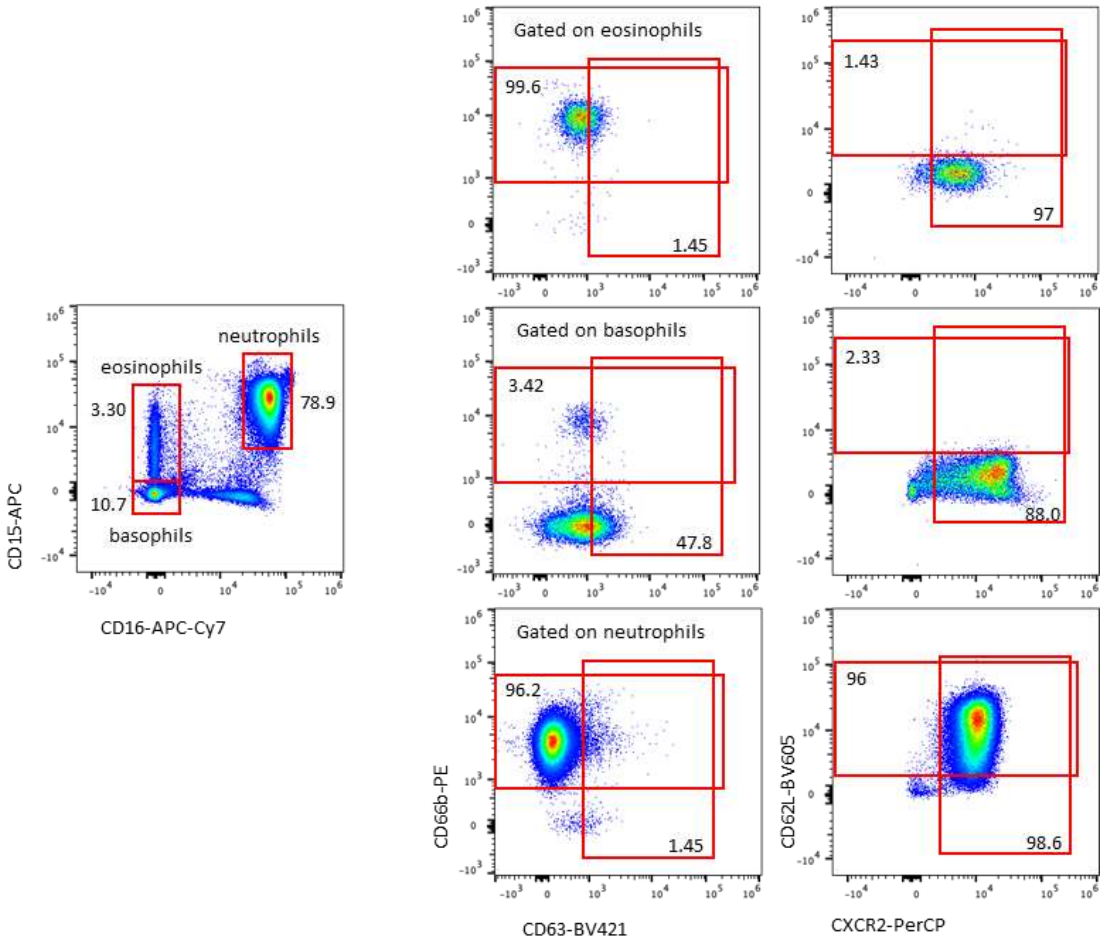


Figure 7b. Within the population of myeloid cells, three populations of granulocytes were identified according to the expression of CD16 and CD15: $CD15^{-}CD16^{-}$ cells were classified as basophils, eosinophils were $CD15^{+}CD16^{-}$, while neutrophils were $CD15^{+}CD16^{+}$. In this populations of granulocytes, the expression of CD66b, CD63, CXCXR2 and CD62L was analysed.

Figure 8a.

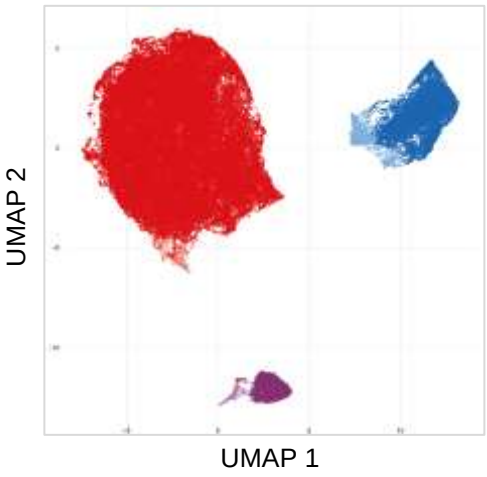


Figure 8a. Uniform Manifold Approximation and Projection (UMAP) representation of the granulocyte landscape.

Figure 8b.

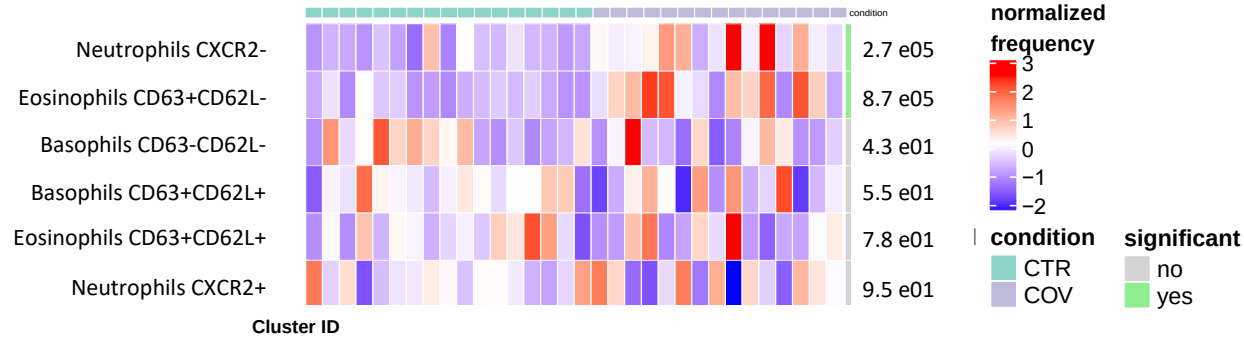


Figure 8b. Differential analysis between healthy donors (bar color: light green; n = 17) and COVID-19 (light purple; n = 15). The heat represents arcsine-square-root transformed cell frequencies that were subsequently normalized per cluster (rows) to mean of zero and standard deviation of one. The color of the heat varies from blue indicating relative under-representation to red indicating relative over-representation. Bar and numbers at the right indicate significant differentially abundant clusters (green) and adjusted *p* values. Clusters are sorted according to adjusted *p* values, so that the cluster at the top shows the most significant abundance changes between the two conditions

Figure 8c.

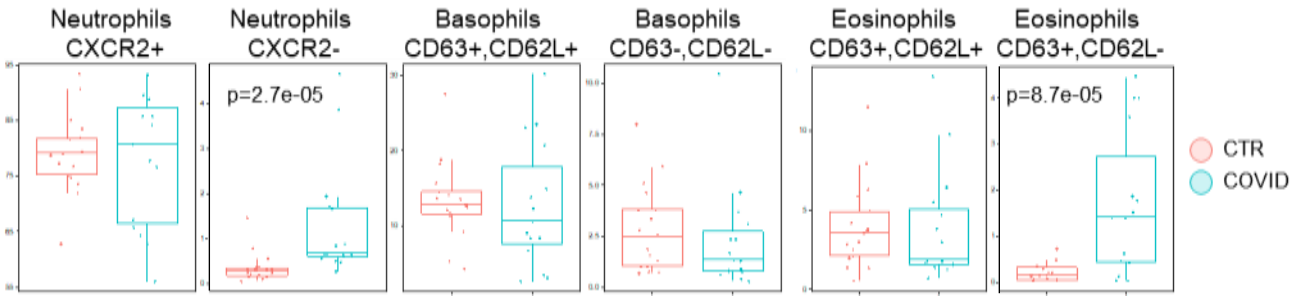


Figure 8c. Boxes and whiskers representation of proportions of different granulocytes subpopulations in healthy donors (salmon) and COVID-19 patients (emerald), obtained by FlowSOM. Five independent experiments on at least four samples per group were performed: n =17 healthy donors, n =14 COVID-19 patients. Data represent individual values (dots), mean (center bar) ± SEM (upper and lower bars). If not indicated, *p* value is not significant.

Figure 8d.

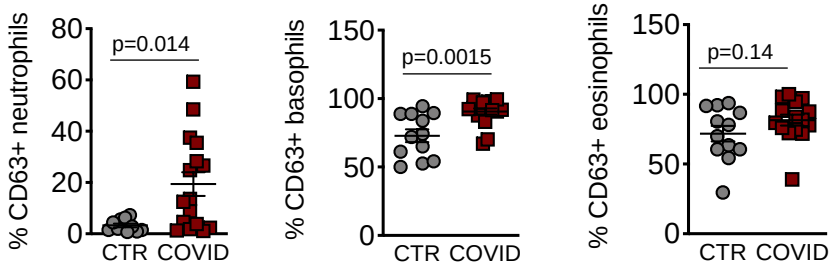


Figure 8d. Scatter plots showing the frequency of $CD63^+$ neutrophils, $CD63^+$ basophils, and $CD63^+$ eosinophils among total neutrophils in healthy donors and COVID-19 patients. Five independent experiments on at least four samples per group were performed: n=11 healthy donors, n=16 COVID-19 patients. Data represent individual values, mean ± SEM. Mann–Whitney test was used for statistical analysis. Exact *p* values are reported in the figure.

Figure 8e.

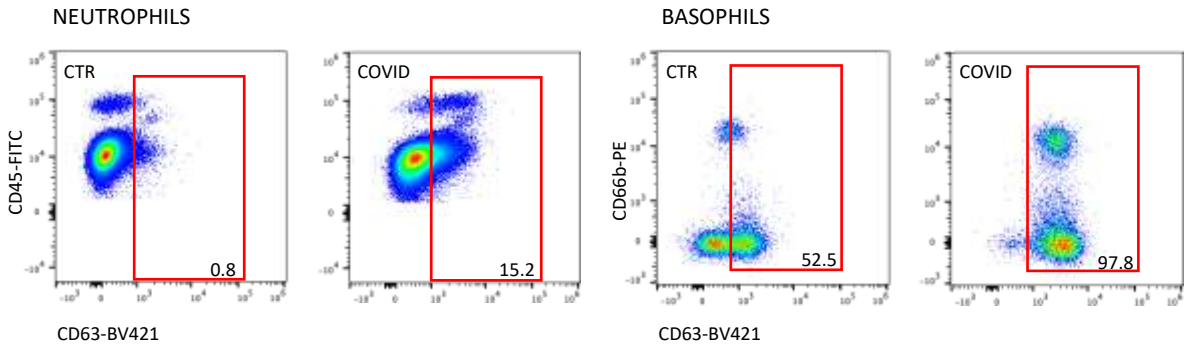


Figure 8e. Representative dot plots showing the percentage of $CD63^{+}$ neutrophils and basophils in one healthy control and one COVID-19 patient.

Figure 8f.

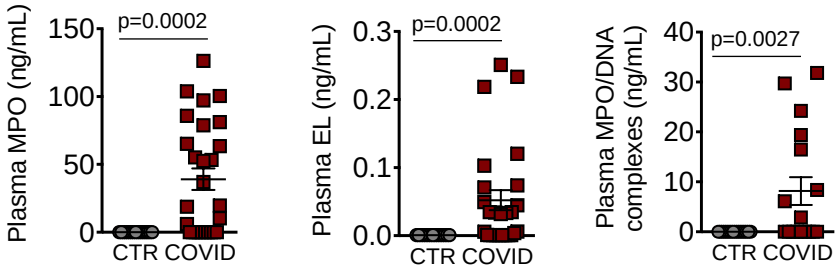


Figure 8f. Scatter plots showing the quantification of myeloperoxidase (MPO), neutrophil elastase (EL), and MPO-DNA complexes in plasma from healthy donors (CTR) and COVID-19 patients (COVID). Three independent experiments on 40 samples, in duplicates, were performed: n=17 healthy donors (for ELISA quantifying MPO, EL, and MPO-DNA complexes), n=27 COVID-19 patients (for ELISA quantifying MPO and EL), n=17 COVID-19 patients (for ELISA quantifying MPO-DNA complexes). Data represent individual values, mean ± SEM. Mann–Whitney test was used for statistical analysis. Exact *p* values are reported in the figure.

Figure 9a.

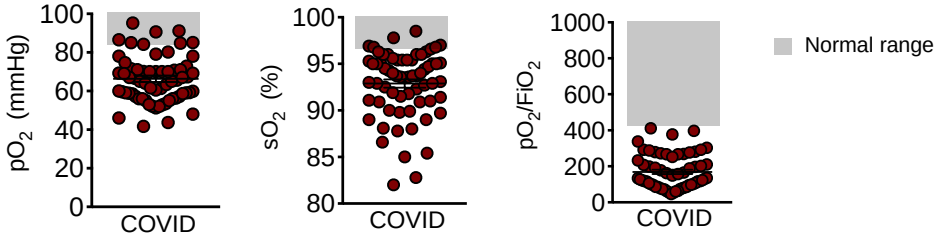


Figure 9a. Representation of pO_2, sO_2, pO_2/FiO_2 in peripheral blood from COVID-19 patients. Levels of these parameters indicate the presence of hypoxemia.

Figure 9b.

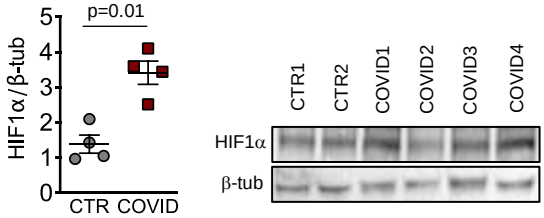


Figure 9b. Quantification of hypoxia inducible factor-1α (HIF-1α) by western blotting. β-tubulin was used as loading control. Two independent experiments on four samples were performed: n=4 healthy donors (CTR), n=4 COVID-19 patients (COVID). Data represent individual values, mean, and SEM. Mann–Whitney test was used for statistical analysis.

Figure 9c.

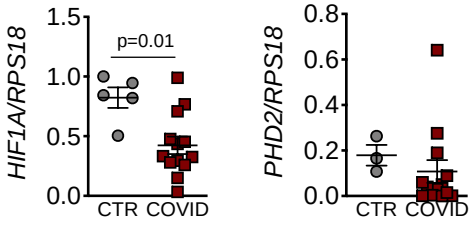


Figure 9c. Quantification of HIF-1α and PHD2 mRNA by real-time PCR. RPS18 was used as housekeeping gene. One experiment was performed on 18 samples, in duplicate: n=5 healthy donors (CTR), n=13 COVID-19 patients (COVID). Data represent individual values, mean, and SEM. Mann–Whitney test was used for statistical analysis.

Figure 9d.

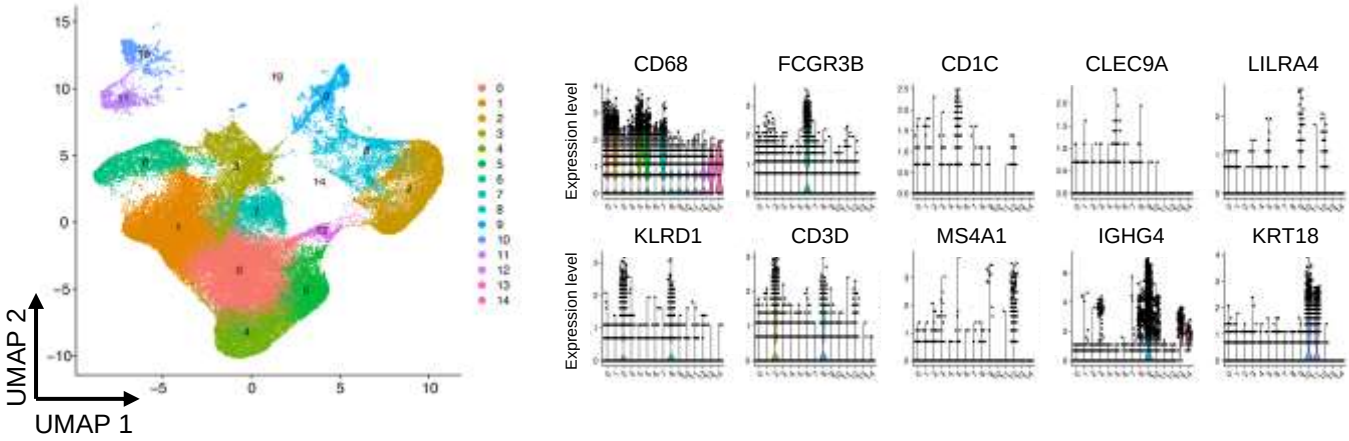


Figure 9d. Dimensional reduction (UMAP) and associated clusters of bronchoalveolar lavage (BAL) cells. One experiment was performed on 12 samples: n = 3 healthy donors, n = 3 mild COVID-19 patients, n = 6 severe COVID-19 patients. Clusters: 0,1,3,4,7 = macrophages; 2,8 = T/Natural Killer (NK) cells; 5 = dendritic cells (DC); 6 = neutrophils; 9,13,14 = plasma cells; 10,11 = epithelial cells; 12 = B cells. Violin plots showing the expression level of the indicated genes across different subsets are also reported. CD68 = macrophages; FCGR3B = neutrophils; CD1C-CLEC9A-LILRA4 = DC; KLRD1 = NK; CD3D = T cells; MSA41 = B cells; IGHG4 = plasma cells; KRT18 = epithelial cells.

Figure 9e.

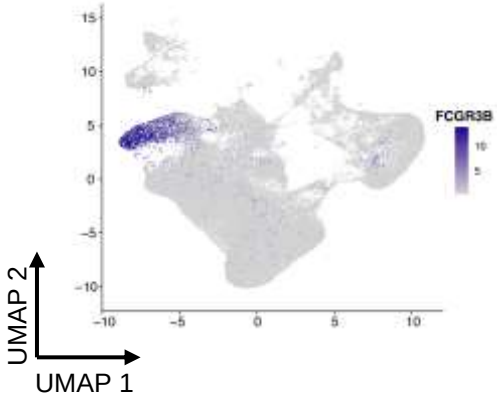


Figure 9e. Normalized expression level of FCGR3B gene, a neutrophilic marker, on UMAP projection. The unimodal expression strictly identifies neutrophils.

Figure 9f.

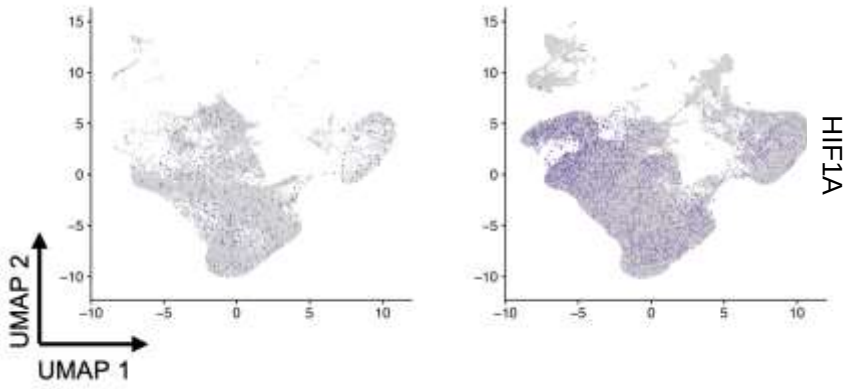


Figure 9f. Normalized expression of *HIF1A* gene on UMAP projection.

Figure 9g.

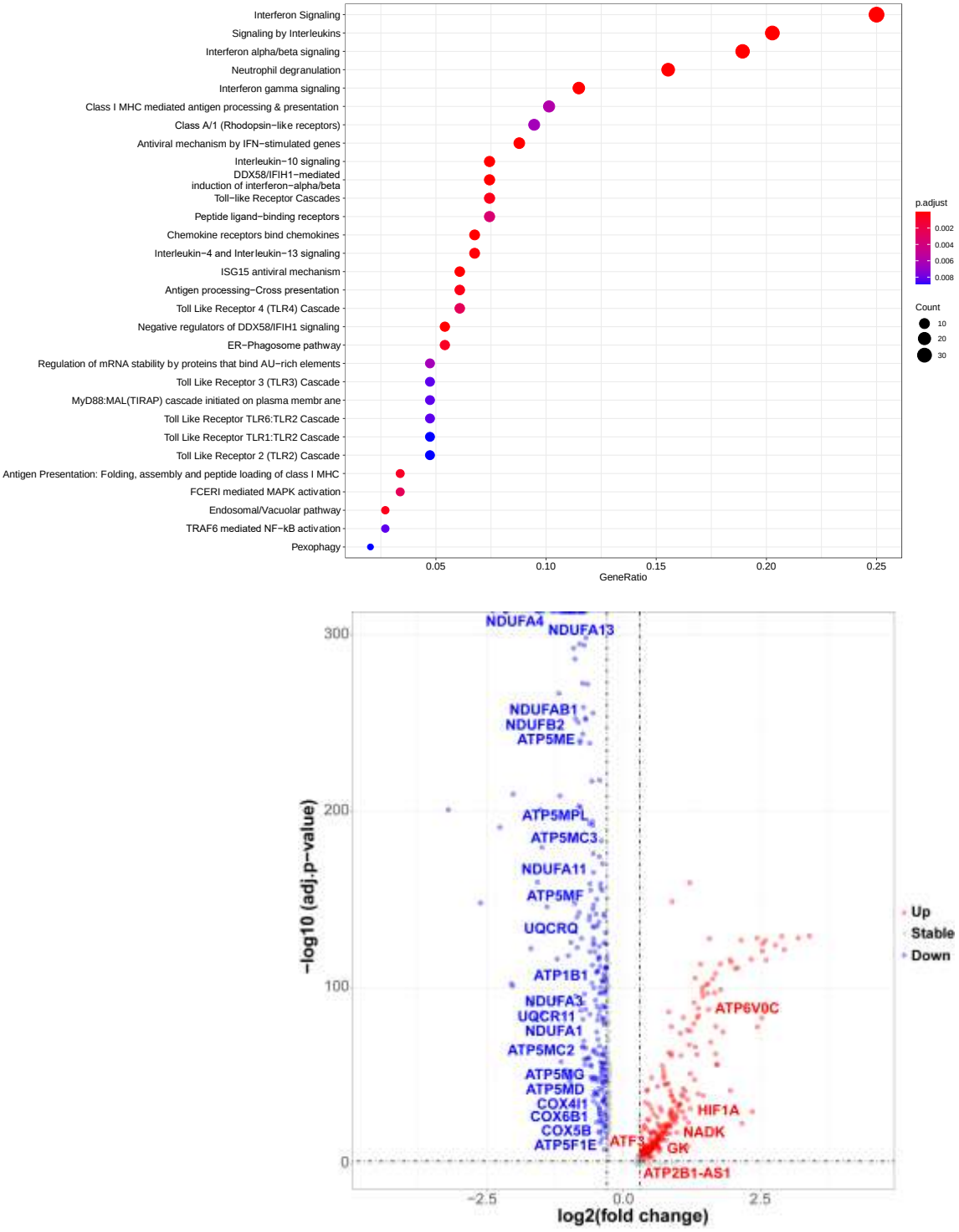


Figure 9g. Upper panel: dot plot of enriched pathways in BAL neutrophils from COVID-19 patients if compared with BAL neutrophils from healthy donors. Bottom panel: Volcano plot representing the differentially regulated mRNAs in BAL neutrophils from COVID-19 patents and healthy controls. Genes encoding for mitochondrial proteins are downregulated and indicated in bold, blue color. Genes encoding for proteins involved in cellular metabolism are upregulated and indicated in bold, red color.

Figure 10.

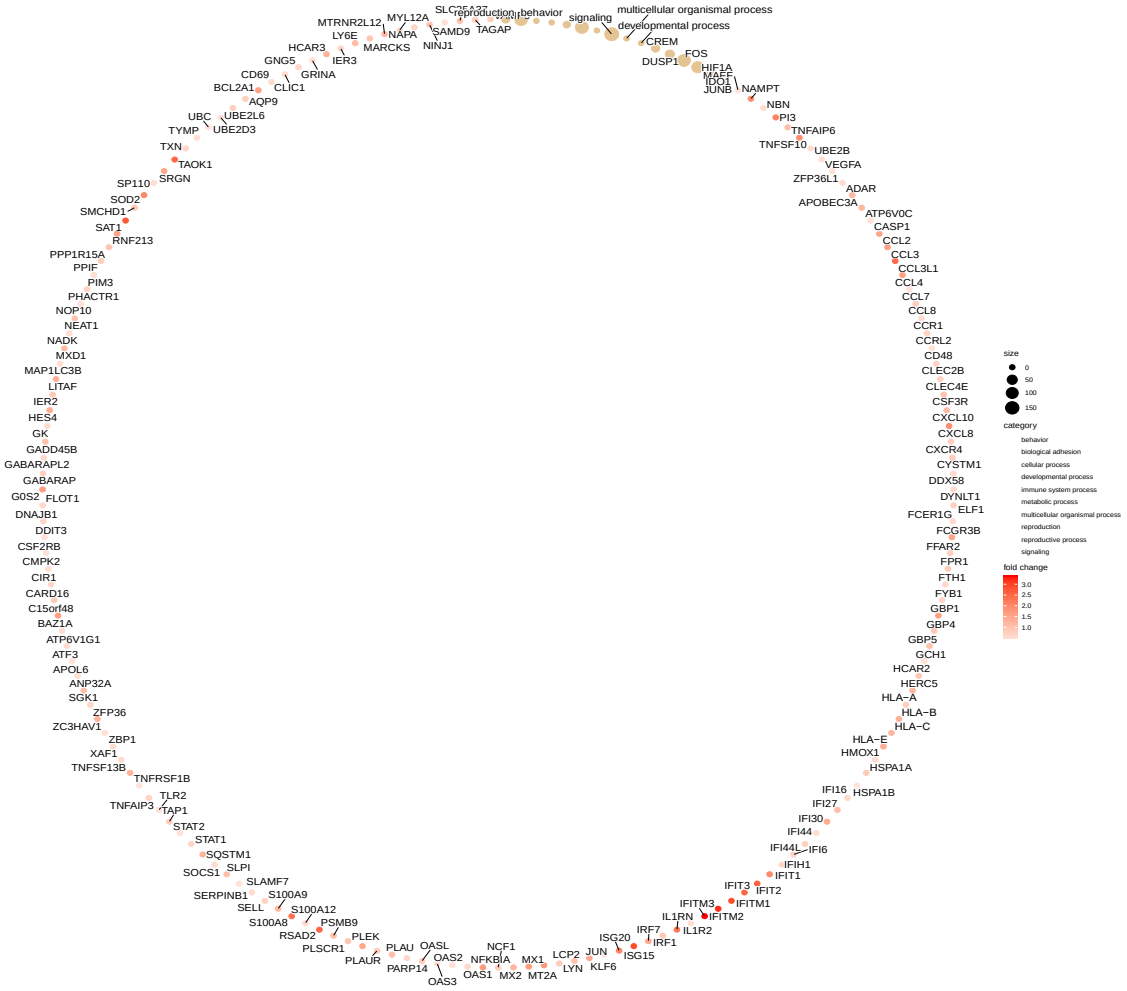


Figure 10. Gene Ontology Enrichment Analysis

Circle plot showing enriched pathways in BAL neutrophils from COVID-19.

Figure 11.

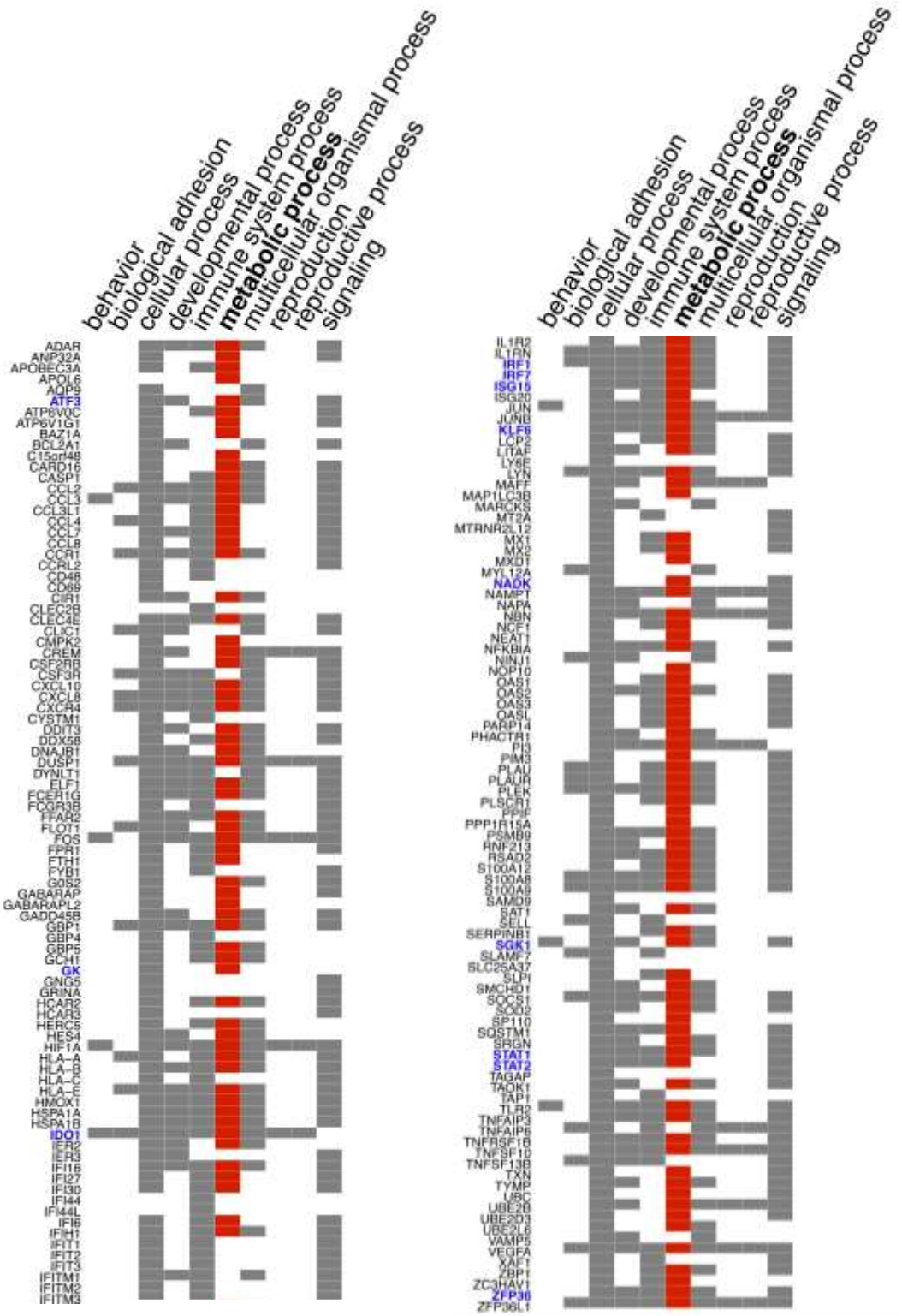


Figure 11. Heat map showing gene ontology enrichment analysis of upregulated genes in BAL neutrophils from both mild and severe COVID-19 patients if compared with neutrophils from healthy donors. One experiment was performed on 12 samples: n=3 healthy donors, n=3 mild COVID-19 patients, n=6 severe COVID-19 patients.

Figure 12a.

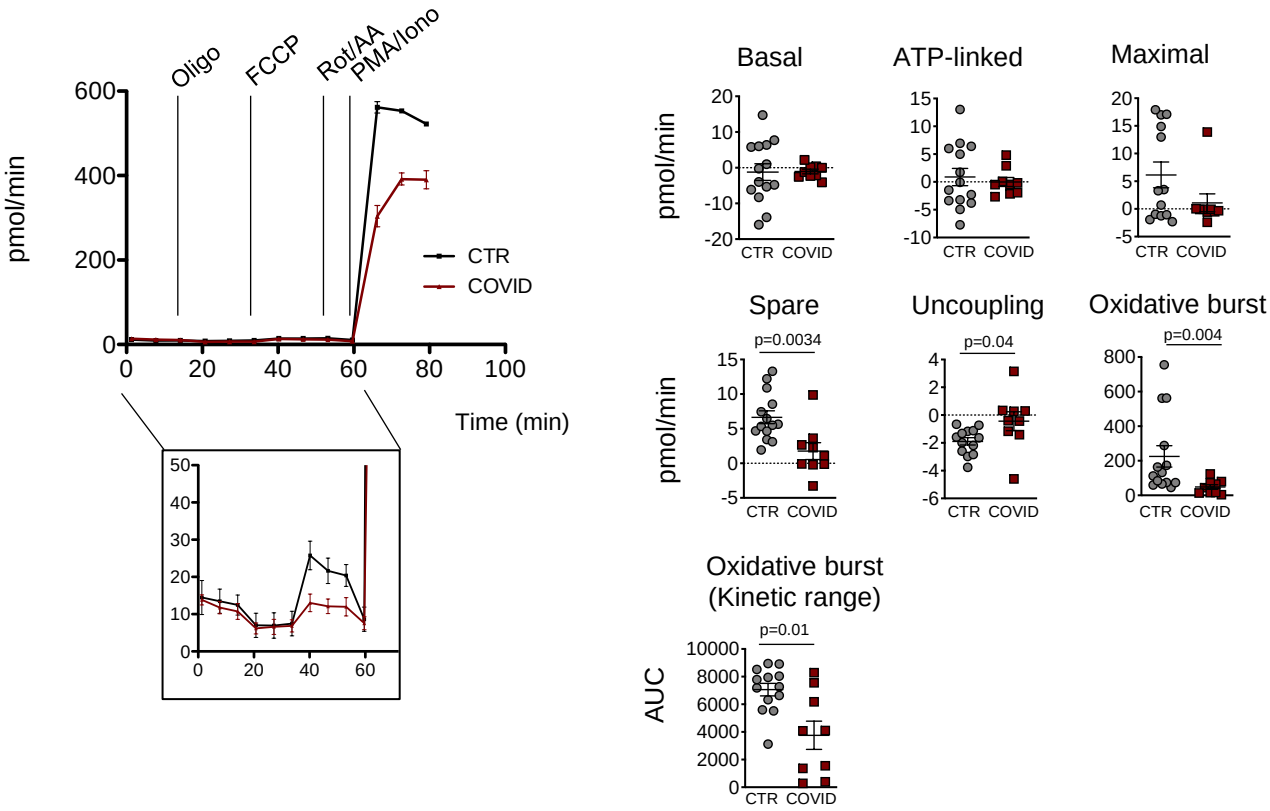


Figure 12a. Measurement of oxygen consumption rate (OCR) and oxidative burst of neutrophils from COVID-19 patients (COVID) and healthy donors (CTR). OCR was measured in real time, under basal condition and in response to mitochondria inhibitors: oligomycin (Oligo, 2 µM), FCCP (0.5 µM), and antimycin A plus rotenone (Rot/AA, 0.5 µM). Oxidative burst was measured in response to PMA/Ionomycin (PMA/Iono, 1 µg/mL). Scatter plots show the quantification of basal respiration (indicated as Basal OCR), ATP-linked respiration (ATP-linked), maximal respiration (Max Resp), uncoupling, spare respiratory capacity (Spare), oxidative burst immediate response. The oxidative burst kinetic range is also reported and was obtained by analyzing the area under the curve (AUC) from the 10th to the 13th measurement. Three independent experiments on 23 samples, in triplicate, were performed: n = 14 healthy donors (CTR), n = 19 COVID-19 patients (COVID). Data represent individual values, mean and standard error of the mean. Mann–Whitney test was used for statistical analysis.

Figure 12b.

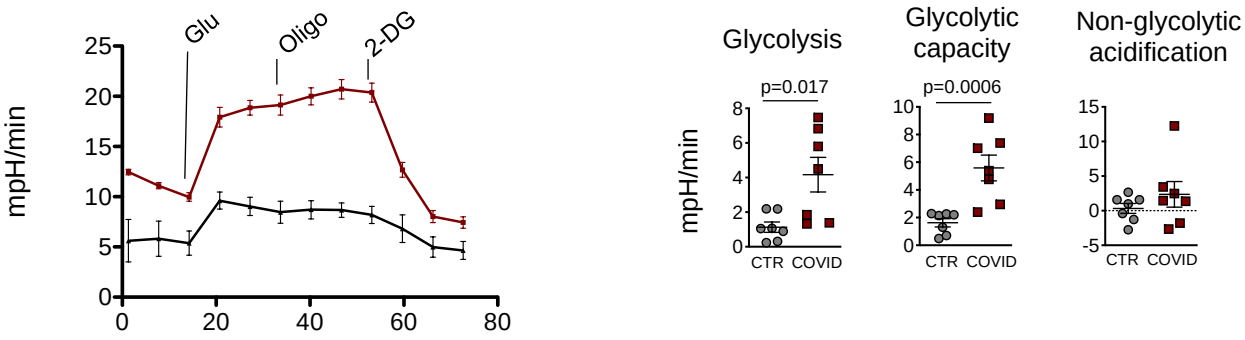


Figure 5b-12b. Measurement of extracellular acidification rate (ECAR) level in neutrophils from healthy controls (CTR) and COVID-19 patients. Scatter plots show the quantification of glycolysis, glycolytic capacity, and non-glycolytic acidification. Three independent experiments on 17 samples, in triplicates, were performed: n = 7 healthy donors (CTR), n = 10 COVID-19 patients (COVID). Data represent individual values, mean, and standard error of the mean. Mann–Whitney test was used for statistical analysis.

Figure 12c.

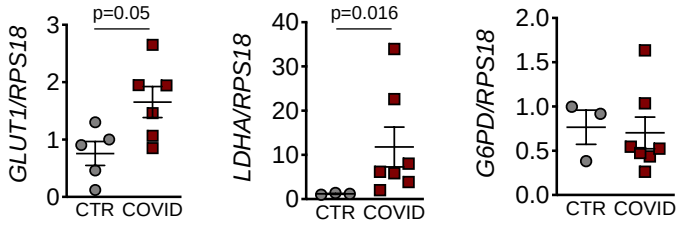
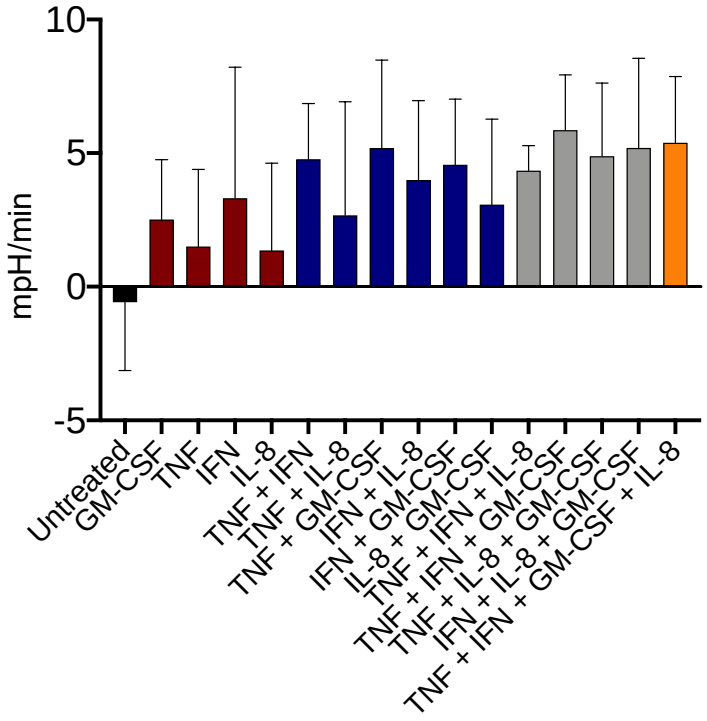


Figure 12c. Quantification of the expression level of lactate dehydrogenase A (LDHA) and glucose-6-phosphate dehydrogenase (G6PD) in neutrophils from COVID-19 patients and healthy donors. One experiment on 12 samples, in duplicate, was performed: n=5 healthy donors (CTR), n=7 COVID-19 patients (COVID). Data represent individual values, mean, and standard error of the mean. Mann–Whitney test was used for statistical analysis.

Figure 12d.



Condition	p-value
Untreated vs TNF+ IFN-γ	0.008
Untreated vs TNF+GM-CSF	0.008
Untreated vs TNF+IL-8	0.03
Untreated vs IFN-γ+GM-CSF	0.008
Untreated vs TNF+ IFN-γ+IL-8	0.004
Untreated vs TNF+IL-8+GM-CSF	0.005
Untreated vs IFN-γ+IL-8+GM-CSF	0.008
Untreated vs IFN-γ+IL-8+GM-CSF+TNF	0.008

Figure 12d. Measurement of ECAR level in neutrophils from healthy controls (CTR) treated with different cytokines, alone or in combination, for 4 h. Histograms show the quantification of glycolysis. Dark red color represents conditions where one single cytokine was used to stimulate neutrophils; blue color represents conditions where two cytokines were used to stimulate neutrophils; gray color represents conditions where three cytokines were used to stimulate neutrophils; orange color represents the condition where four cytokines were used to stimulate neutrophils. Two independent experiments on six samples, in triplicate, were performed. Data represent individual values, mean, and standard error of the mean. Mann–Whitney test was used for statistical analysis.

Figure 13a.

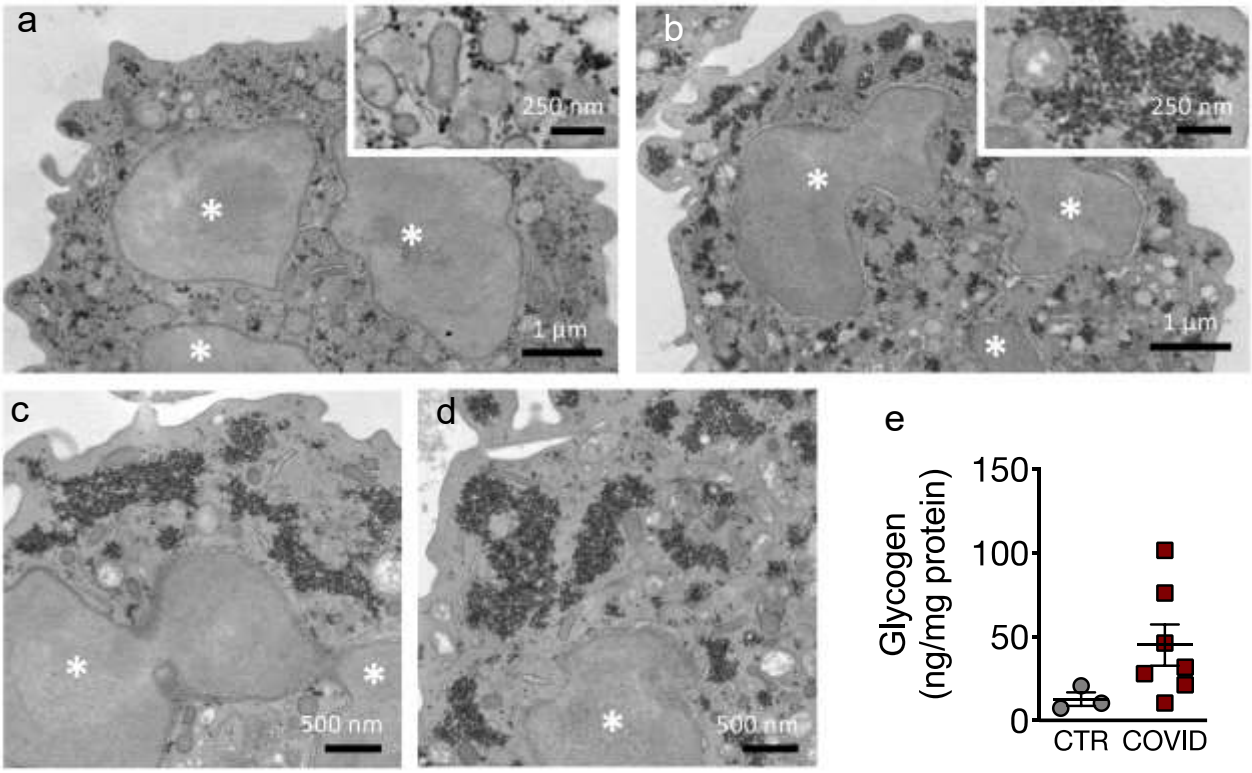


Figure 13a. Representative electron micrographs of mitochondrial ultrastructural changes observed in COVID-19 neutrophils. Panels "a" is a representative micrograph of neutrophils from healthy donor, whereas panels "b-d" are representative electron micrographs of neutrophils from COVID-19 patients. Asterisks refer to nucleus. In panel "e," the quantification of intracellular glycogen levels is reported. Two independent experiments on nine samples, in duplicate, were performed: n = 3 healthy donors (CTR), n = 6 COVID-19 patients (COVID). Mann–Whitney test was used for statistical analysis. Exact *p* values are reported in the figure.

Figure 13b.

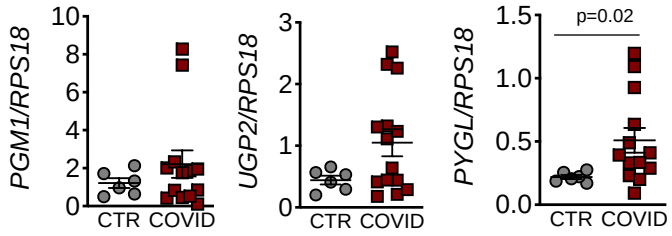


Figure 13b. Quantification of the expression level of phosphoglucomutase 1 (PGM1), glycogen phosphorylase L (PYGL), and UDP-glucose pyrophosphorylase 2 (UGP2). Two independent experiments on 20 samples, in duplicate, were performed: n = 6 healthy donors (CTR), n = 14 COVID-19 patients (COVID). Data represent individual values, mean, and standard error of the mean. Mann–Whitney test was used for statistical analysis.

Figure 13c.

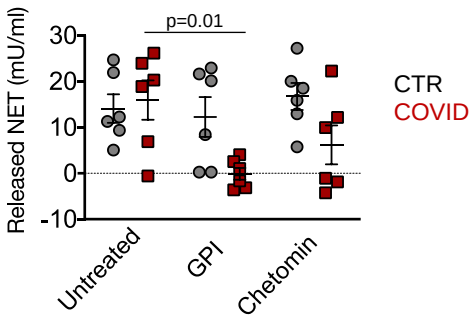


Figure 13c. Quantification of neutrophil extracellular traps (NET) release by neutrophils from healthy controls (CTR, in black) and COVID-19 patients (COVID, in dark red), in vitro, in the presence/absence of glycogen phosphorylase inhibitor (GPI, 50 µM,4 h) or chetomin, an HIF-1α inhibitor (10 ng/mL, 4 h). Cell cultures were performed with RPMI medium with glucose. Two independent experiments on six samples were performed: n=5 healthy donors (CTR), n=6 COVID-19 patients (COVID). Data represent individual values, mean ± standard error of the mean. Mann–Whitney test was used for statistical analysis

Figure 13d.

>chromosome:GRCh38:14:50857291:50945083:-1

GCTACGAGCGGGGCGAACTTTGGTCCAGGAGTTAAGAAACCTGAACCCTGGAGTCCTCAA
AAAAAATGAATGAAAATAACAGAGGCGCCCTGAGGATCCAAGCTGGGGCGGTGCCAAGGG
CTGGCAAGTGAGGTTGGGACAACAGAAGTCAA**ACGTG**CCGTCCTTCCAGATCCCGGCGCT
TATGGCGGAAGCCACTCCAGGTGAGAAATCCTAACAGTCATAATGGCATAACAAATAAAC
ATCGGCAAAACAGCAGTCTGCCAACG**ACGTG**CTTCCCTACACAGACGTCCTCCTGTCTCC
ACACTCTAGAGGGGAGAGGCGGAACAAATGCTGCCTCCGCAGATTTTGGAAATCCGGAAG
GGAGCCTCCGAGCCCAGGTCCCGGGCTGGCAGGGGTCTCGCCGGCGCTTGGACCTCGTCT
CCCACCCCCGAGCCCACTGCGGCCCCAGAGCCTCGGGAGGGGCCGGGCACTTCCTCTGCC
CTCCGGCCTGGGGCAGGGGCCGGGACGCGGTGGGAGTGCAGCGGGGACGGCACCGCCCGA
GGGGGCGGGCCCCAAACTTTCGTGCGCGTTGAAAGCTGCTGGCGCGGCGGGGCGGACTCC
ACCCCTGCCCGGCAGCCCAGCGCCTCCGGCCGCACTTCCAGCTCTCTGCGCAGCCCGCCG
CGCAGCCCGCCGCCCCAGCCATGGCGAAGCCCCTGACGGACCAGGAGAAGCGGCGGCAGA
TCAGCATCCGCGGCATCGTGGGCGTGGAGAACGTGGCAGAGCTGAAGAAGAGTTTCAACC
GGCACCTGCACTTCACGCTGGTCAAGGACCGCAACGTGGCCACCACCCGCGACTACTACT
TCGCGCTGGCGCACACGGTGCGCGACCACCTGGTGGGGCGCTGGATCCGCACGCAGCAGC
ACTACTACGACAAGTGCCCCAAG

Figure 13d. A portion of the *PYGL* gene is represented. Letters in light blue identify the core of hypoxia-responsive elements (HRE), whereas letters in dark red identify the first exon of the gene. Source: http://www.ensembl.org/Homo_sapiens/Gene/Sequence?db =core;g=ENSG00000100504; r = 14:50857891-50944483.

Figure 13e.

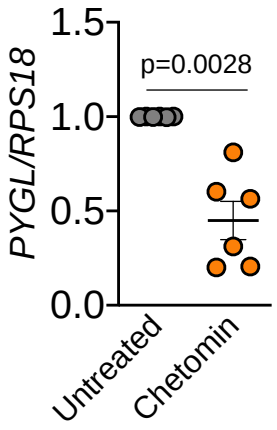


Figure 13e. Quantification of *PYGL* expression in neutrophils in the presence or absence of the HIF-1α inhibitor chetomin. One experiment on six samples, in duplicate, was performed. Data represent individual values, mean, and standard error of the mean (n = 6). Mann–Whitney test was used for statistical analysis.

Figure 14a.

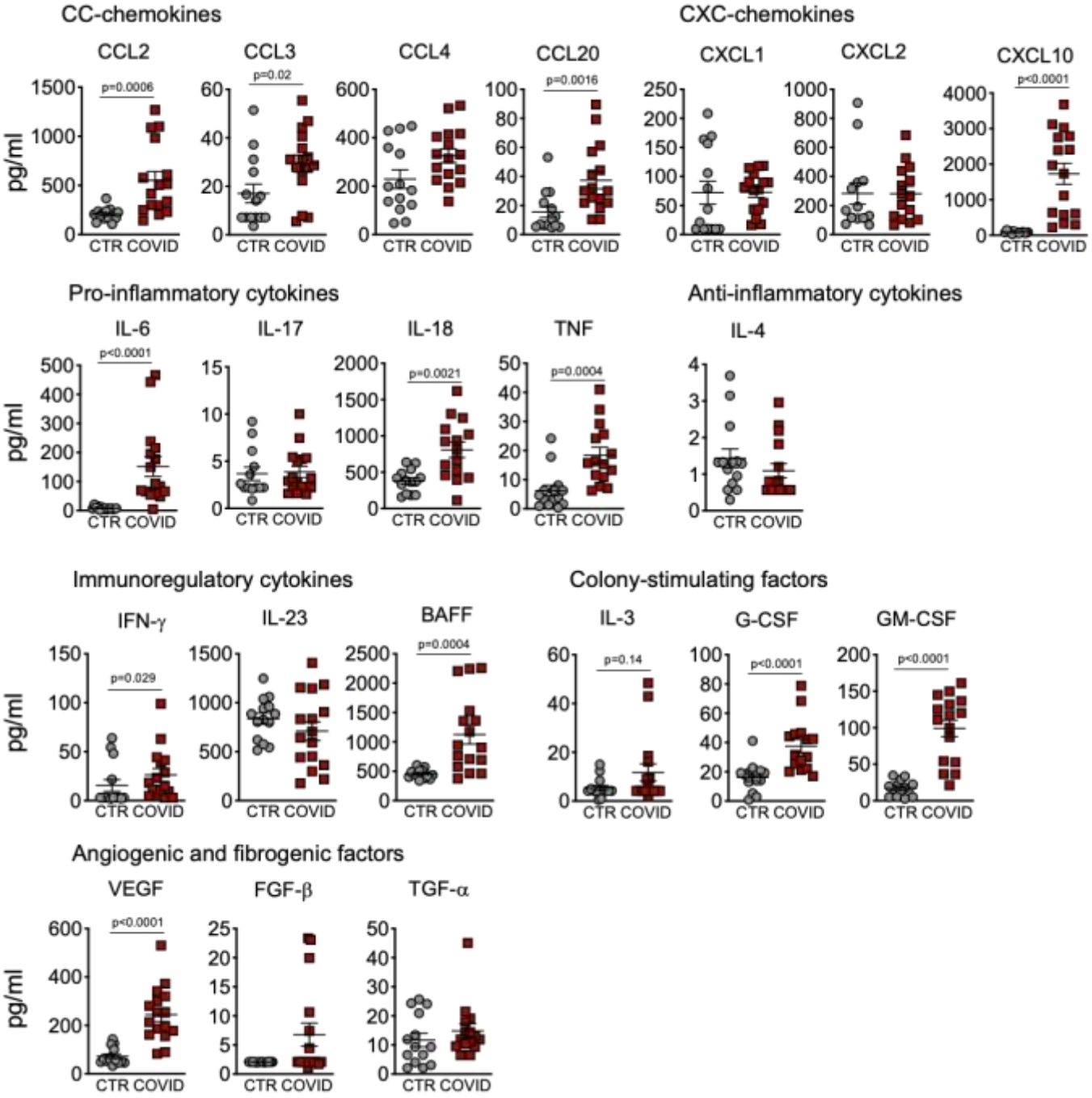


Figure 14a. Quantification of cytokines and other mediators in plasma obtained from COVID-19 patients and healthy controls. One experiment on 30 samples was performed: n = 16 healthy donors (CTR), n = 14 COVID-19 patients (COVID). Data represent individual values, mean (center bar) ± SEM (upper and lower bars). Statistical analysis by two-sided Mann–Whitney nonparametric test.

Figure 14b.

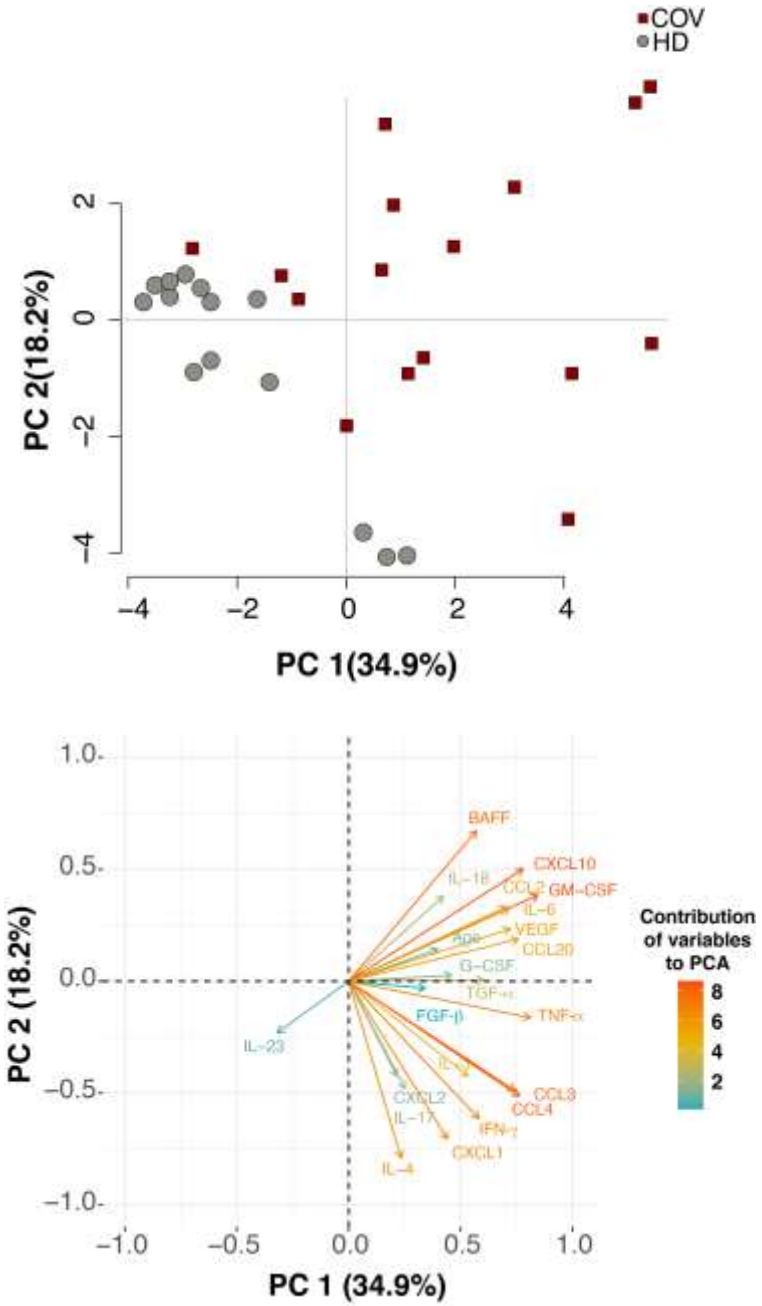


Figure 14b. Principal component analysis (PCA) analysis of cytokines, chemokines, and other soluble molecules involved in neutrophils' regulation. The PCA plot (upper) shows the first two principal components separating the samples. The percentage of explained variance for each component is shown in brackets. Each gray circle represents healthy donor, each red square represents a COVID-19 patient. At the bottom, a plot displays the variables as vectors, indicating the direction of each variable to the overall distribution. The strength of each variable is represented by colors: orange color represents a strong contribution; light blue color represents a milder contribution.

Figure 15a.

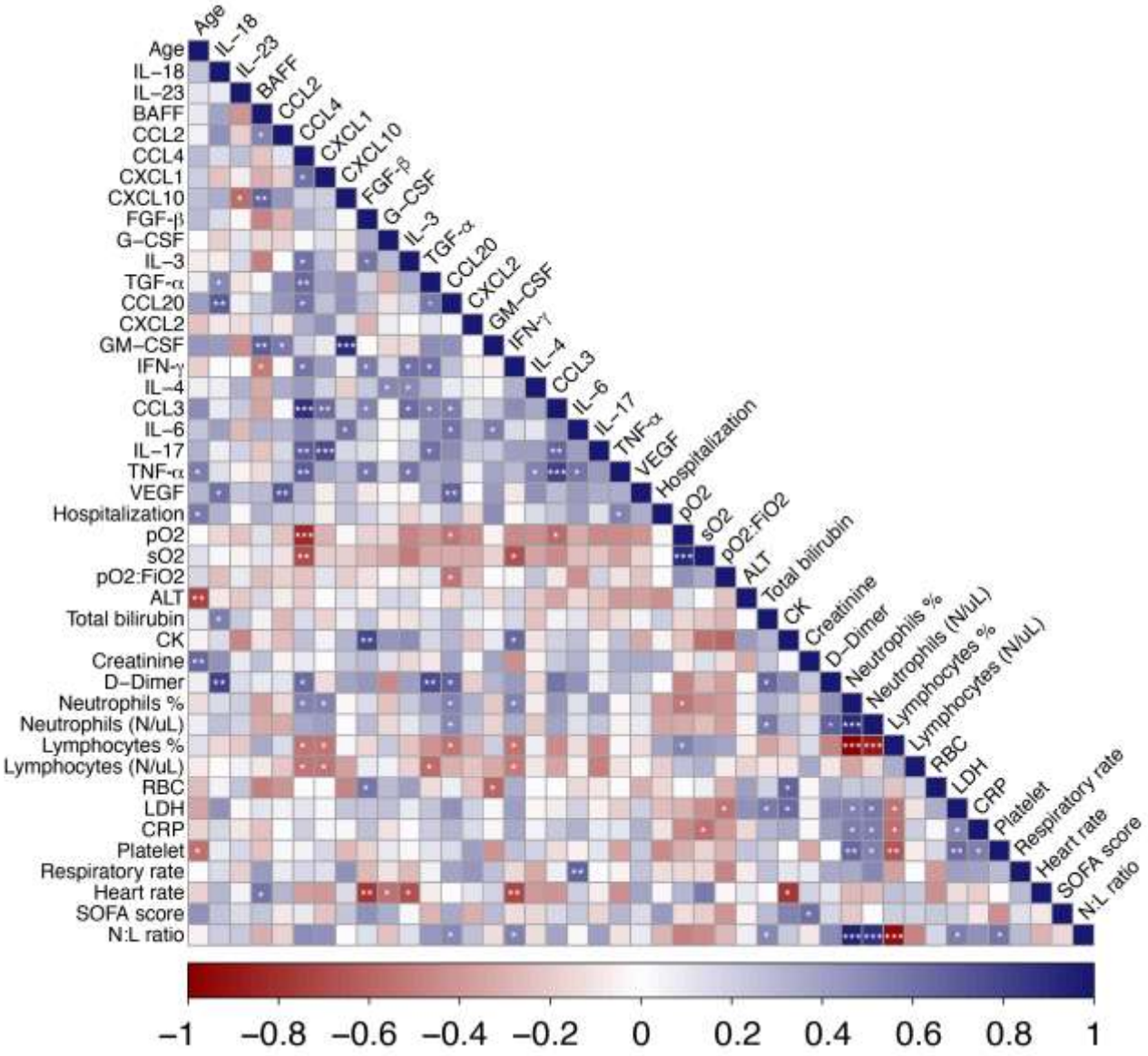


Figure 15a. Correlation map of the indicated parameters and clinical characteristics. Colors reflect the magnitude of the Pearson's correlation coefficient (red indicates negative correlation, blue indicates positive correlation). One experiment on 30 samples was performed: n = 16 healthy donors (CTR), n = 14 COVID-19 patients (COVID). Asterisks represent the statistically significant correlations: * $p < 0.05$, ** $p < 0.01$, ***$p < 0.001$. N:L ratio, neutrophil to lymphocyte ratio; LDH, lactate dehydrogenase; CRP, C-reactive protein; RBC, red blood cells; pCO_2, partial pressure of carbon dioxide; pO_2, partial pressure of oxygen; sO_2, oxygen saturation; pO_2/FiO_2, fraction of inspired oxygen; ALT, alanine aminotransferase; CK, creatine kinase.

Figure 15b.

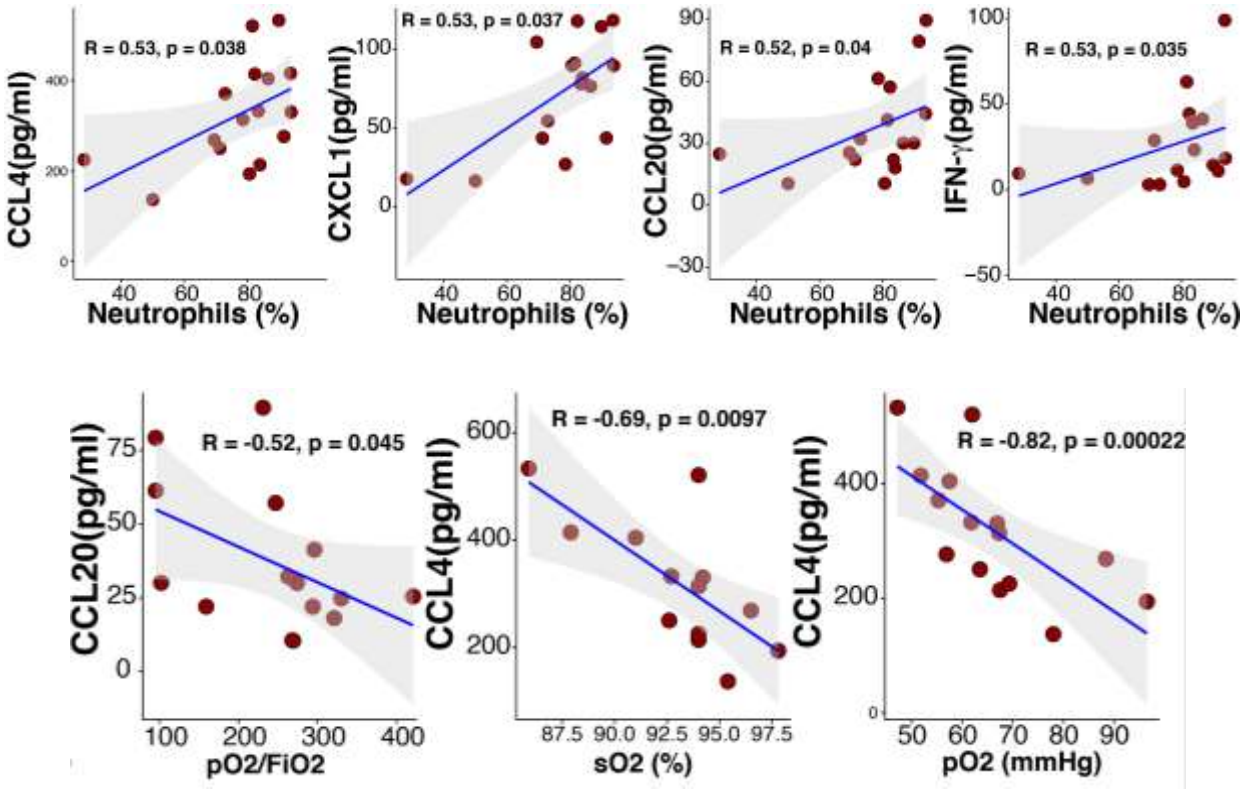


Figure 15b. The following correlations are reported: (i) Neutrophils' percentage with CCL4, CXCL1, CCL20, IFN-γ; (ii) CCL20 with pO_2/FiO_2; (iii) CCL4 with sO_2 and with pO_2.

Table 6. Differentially expressed genes between BAL neutrophils from COVID-19 patients and BAL neutrophils from healthy donors.
p_val = p-value not adjusted for multiple test correction; avg_logFC = average log2 fold change. Positive values indicate that the gene is more highly expressed in the cluster; pct.1 = The percentage of cells where the gene is detected in the cluster; pct.2 = The percentage of cells where the gene is detected on average in the other clusters; p_vl adj = Adjusted p-value, based on Bonferroni correction using all genes in the dataset, used to determine significance.

Upregulated genes

	p_val	avg_logFC	pct.1	pct.2	p_val_adj
IFITM3	3,84E-134	3,396981676	1	0.247	8,27E-130
IFITM2	5,87E-133	3,195462778	0.997	0.102	1,26E-128
ISG15	2,18E-126	2,937114006	0.999	0.251	4,70E-122
IFITM1	5,63E-134	2,892159343	0.997	0.009	1,21E-129
SAT1	6,84E-129	2,775742481	1	0.981	1,47E-124
IFIT2	1,60E-120	2,608106101	0.984	0.121	3,44E-116
RSAD2	1,46E-131	2,592040286	0.993	0.047	3,14E-127
TAOK1	8,70E-130	2,545623147	0.993	0.088	1,87E-125
IFIT3	1,16E-125	2,541314356	0.99	0.135	2,49E-121
CCL3L1	8,71E-88	2,529204393	0.947	0.27	1,87E-83
S100A8	1,31E-82	2,448154552	0.987	0.819	2,82E-78
H3F3B	5,23E-133	2,442187326	1	0.856	1,13E-128
CCL4L2	1,50E-34	2,356495672	0.915	0.553	3,23E-30
IL1RN	6,17E-121	2,334946165	0.968	0.051	1,33E-116
PI3	7,20E-28	2,169601246	0.38	0	1,55E-23
ISG20	9,29E-132	2,151000341	0.985	0	2,00E-127
SOD2	4,29E-116	2,092116889	0.99	0.293	9,24E-112
IFIT1	1,11E-115	2,042763162	0.971	0.112	2,39E-111
TNFSF10	2,87E-119	1,973023284	0.952	0.056	6,17E-115
CXCL8	1,87E-46	1,953252904	0.668	0.177	4,02E-42
NAMPT	1,14E-120	1,945129416	0.99	0.284	2,46E-116
MT2A	1,11E-79	1,81771992	0.988	0.512	2,40E-75
NFKBIA	1,00E-103	1,778361471	0.955	0.167	2,16E-99
MX1	2,28E-118	1,771332984	0.983	0.126	4,91E-114
G0S2	2,92E-61	1,713083517	0.682	0.06	6,29E-57
CCL4	3,58E-61	1,704168003	0.892	0.228	7,72E-57
C15orf48	6,75E-83	1,689343931	0.938	0.223	1,45E-78
CCL3	2,46E-67	1,687480711	0.918	0.233	5,30E-63
GBP1	8,10E-113	1,685697433	0.961	0.116	1,74E-108
BCL2A1	7,09E-102	1,664263161	0.981	0.321	1,53E-97
RNF213	8,06E-110	1,634542953	0.976	0.209	1,74E-105
FCGR3B	6,90E-74	1,597583073	0.722	0.005	1,49E-69
CCL2	1,13E-132	1,571331991	0.964	0.005	2,44E-128
PLEK	1,69E-92	1,55729973	0.937	0.251	3,65E-88
SRGN	4,69E-107	1,546001866	1	0.935	1,01E-102
KLF6	1,29E-101	1,537902765	0.991	0.298	2,79E-97

IRF7	2,41E-106	1,511429898	0.909	0.07	5,18E-102
HES4	1,30E-43	1,460496477	0.527	0.005	2,79E-39
IFI30	9,11E-100	1,452279956	0.962	0.172	1,96E-95
HLA-E	7,46E-105	1,445093656	0.998	0.553	1,61E-100
H3F3A	1,79E-102	1,440075426	0.998	0.977	3,86E-98
HLA-B	3,16E-118	1,409158454	1	0.995	6,81E-114
LITAF	5,24E-89	1,375311019	0.951	0.456	1,13E-84
ZFP36	4,13E-93	1,368792068	0.914	0.153	8,90E-89
HCAR3	1,26E-44	1,366848433	0.584	0.084	2,72E-40
TNFSF13B	9,26E-88	1,348802717	0.871	0.13	1,99E-83
SQSTM1	6,82E-67	1,345838966	0.871	0.307	1,47E-62
MX2	3,16E-71	1,314780884	0.735	0.051	6,80E-67
HLA-C	2,58E-110	1,312595906	1	0.972	5,55E-106
HERC5	1,18E-52	1,300905596	0.64	0.093	2,54E-48
APOBEC3A	2,29E-96	1,295718696	0.822	0	4,93E-92
ATP6V0C	1,99E-84	1,292025183	0.769	0.005	4,28E-80
MTRNR2L12	3,05E-80	1,222338597	0.747	0.009	6,57E-76
S100A9	3,66E-36	1,220999171	0.986	0.972	7,88E-32
MXD1	4,04E-56	1,219826058	0.644	0.056	8,70E-52
CXCL10	2,30E-164	1,212740536	0.914	0.005	4,96E-160
LY6E	1,97E-72	1,20585133	0.989	0.726	4,24E-68
PLAU	3,42E-28	1,190522309	0.452	0.074	7,36E-24
SLPI	1,87E-14	1,183093161	0.29	0.056	4,03E-10
TNFAIP6	1,97E-41	1,170580244	0.626	0.144	4,25E-37
IFI27	7,77E-81	1,166128578	0.964	0.228	1,67E-76
ANP32A	4,61E-46	1,128225084	0.625	0.144	9,92E-42
GADD45B	6,49E-31	1,121137681	0.479	0.074	1,40E-26
PSMB9	6,69E-88	1,095221302	0.904	0.163	1,44E-83
LCP2	1,37E-47	1,094770312	0.603	0.084	2,96E-43
PNRC1	4,05E-43	1,090894779	0.667	0.233	8,72E-39
GBP5	2,59E-34	1,088169771	0.462	0.023	5,57E-30
CSF3R	3,68E-44	1,06110855	0.6	0.102	7,92E-40
NEAT1	2,91E-66	1,054953471	0.998	0.953	6,28E-62
PLSCR1	6,31E-79	1,04322229	0.905	0.233	1,36E-74
SLC25A37	1,28E-38	1,043043489	0.514	0.042	2,76E-34
MARCKS	3,16E-39	1,026273138	0.575	0.112	6,81E-35
PPP1R15A	5,92E-38	1,017758243	0.557	0.116	1,28E-33
NINJ1	2,05E-35	1,015060085	0.523	0.098	4,41E-31
SMCHD1	9,61E-38	0,988620195	0.537	0.088	2,07E-33
IRF1	6,63E-32	0,98051542	0.479	0.07	1,43E-27
HIST2H2AA4	1,28E-22	0,979830352	0.322	0	2,75E-18
HCAR2	3,37E-28	0,957737835	0.464	0.093	7,27E-24
IER2	8,07E-31	0,951909063	0.485	0.088	1,74E-26
FPR1	1,83E-33	0,947966877	0.526	0.13	3,94E-29
GBP4	4,30E-30	0,93594112	0.447	0.051	9,26E-26
LYN	1,18E-40	0,925692156	0.584	0.116	2,55E-36
CARD16	1,48E-40	0,920341341	0.762	0.512	3,18E-36

DDX60L	8,12E-33	0,893473895	0.588	0.237	1,75E-28
CCL8	1,26E-153	0,892333937	0.882	0.005	2,72E-149
OASL	7,66E-31	0,883227975	0.494	0.107	1,65E-26
PLAUR	1,67E-43	0,883161127	0.867	0.391	3,60E-39
CYSTM1	8,06E-36	0,880106972	0.509	0.065	1,74E-31
FFAR2	2,29E-28	0,878739826	0.388	0.005	4,93E-24
VAMP5	8,43E-83	0,877915939	0.776	0.047	1,82E-78
HLA-A	1,57E-67	0,875839519	1	0.977	3,38E-63
UBE2L6	3,49E-66	0,875039885	0.746	0.102	7,51E-62
ELF1	4,74E-31	0,874804029	0.478	0.079	1,02E-26
IFI44L	1,59E-43	0,87254122	0.598	0.084	3,43E-39
TAGAP	6,36E-34	0,871336506	0.451	0.014	1,37E-29
TAP1	1,67E-34	0,862914083	0.484	0.047	3,60E-30
NCF1	5,66E-26	0,862714955	0.556	0.2	1,22E-21
JUNB	2,00E-46	0,862713402	0.712	0.181	4,30E-42
PPIF	1,92E-26	0,852149533	0.417	0.056	4,13E-22
CXCR4	3,48E-22	0,847101549	0.421	0.098	7,49E-18
AQP9	8,67E-33	0,842977103	0.509	0.098	1,87E-28
MT-ATP8	4,82E-91	0,830391233	0.892	0.149	1,04E-86
DUSP1	5,15E-68	0,828736535	0.915	0.209	1,11E-63
GABARAP	1,85E-50	0,822855344	0.958	0.609	3,99E-46
HIF1A	7,74E-27	0,821658007	0.463	0.107	1,67E-22
TNFAIP3	3,95E-22	0,802883861	0.419	0.107	8,51E-18
CCRL2	3,64E-26	0,800942264	0.462	0.112	7,84E-22
SELL	1,43E-27	0,798330187	0.38	0.005	3,09E-23
PHACTR1	7,45E-25	0,787660585	0.501	0.163	1,60E-20
CLEC4E	1,68E-26	0,786501911	0.404	0.042	3,61E-22
IDO1	2,97E-18	0,78260719	0.27	0	6,40E-14
EPSTI1	5,10E-50	0,778888045	0.674	0.112	1,10E-45
IFI6	4,41E-50	0,762398879	0.984	0.563	9,49E-46
CLEC2B	4,05E-24	0,760462515	0.429	0.088	8,71E-20
AC015912.3	7,31E-22	0,757118558	0.328	0.014	1,57E-17
NAPA	3,19E-26	0,751025911	0.42	0.06	6,88E-22
STAT1	1,74E-53	0,742405856	0.747	0.167	3,75E-49
PARP14	1,57E-23	0,741396265	0.45	0.121	3,38E-19
GNG5	3,16E-55	0,738896676	0.951	0.377	6,80E-51
FOS	8,65E-58	0,730927388	0.907	0.247	1,86E-53
TXN	5,35E-27	0,728187469	0.967	0.837	1,15E-22
IER3	9,04E-19	0,720289496	0.338	0.056	1,95E-14
SAMD9L	9,93E-22	0,716131837	0.438	0.13	2,14E-17
SGK1	1,43E-60	0,712429061	0.742	0.126	3,08E-56
IFIH1	1,25E-22	0,708766186	0.401	0.079	2,69E-18
CIR1	7,31E-20	0,708219664	0.427	0.135	1,57E-15
FTH1	6,98E-35	0,701502941	1	1	1,50E-30
IFI16	4,00E-23	0,699855864	0.489	0.177	8,62E-19
FYB1	4,11E-18	0,692421213	0.414	0.144	8,85E-14
GABARAPL2	3,65E-13	0,67226222	0.385	0.177	7,85E-09

DYNLT1	8,74E-37	0,670864879	0.67	0.223	1,88E-32
DDX58	4,02E-20	0,668685917	0.359	0.065	8,67E-16
OAS1	7,09E-26	0,666005419	0.481	0.121	1,53E-21
FCER1G	5,74E-26	0,660634218	0.998	0.995	1,24E-21
CD69	7,79E-14	0,652804537	0.253	0.033	1,68E-09
FLOT1	2,04E-19	0,651994522	0.385	0.102	4,40E-15
SERPINB1	7,20E-12	0,649280976	0.372	0.186	1,55E-07
XAF1	1,04E-18	0,640339679	0.424	0.14	2,24E-14
SOCS1	1,32E-14	0,64000428	0.247	0.019	2,85E-10
CREM	1,81E-20	0,638489738	0.32	0.019	3,90E-16
UBE2B	3,32E-20	0,63785228	0.404	0.107	7,15E-16
KIAA1551	1,56E-18	0,637287157	0.368	0.088	3,35E-14
WARS	6,94E-28	0,628908135	0.517	0.112	1,49E-23
GK	4,14E-18	0,627260353	0.426	0.149	8,92E-14
ADAR	2,14E-19	0,626843301	0.405	0.116	4,61E-15
ATP6V1G1	9,57E-49	0,624799171	0.862	0.307	2,06E-44
ZBP1	1,08E-21	0,62395101	0.338	0.023	2,33E-17
NBN	1,57E-18	0,623915903	0.373	0.093	3,38E-14
S100A12	1,60E-14	0,623126853	0.221	0	3,44E-10
CLIC1	2,35E-31	0,62092304	0.965	0.777	5,06E-27
CCR1	2,18E-16	0,619632702	0.343	0.088	4,69E-12
C4orf3	4,00E-16	0,616875707	0.451	0.214	8,61E-12
MAP1LC3B	5,53E-16	0,615702125	0.407	0.163	1,19E-11
NADK	1,63E-21	0,6135286	0.399	0.088	3,52E-17
IFI44	2,34E-18	0,611910365	0.359	0.084	5,04E-14
OAS3	5,74E-19	0,600382063	0.34	0.056	1,24E-14
SP110	4,73E-17	0,594877677	0.368	0.107	1,02E-12
CMPK2	8,16E-18	0,586307518	0.302	0.033	1,76E-13
MYL12A	6,90E-23	0,585982161	0.972	0.93	1,49E-18
GRINA	5,91E-14	0,573033813	0.489	0.302	1,27E-09
IL1R2	8,98E-17	0,572325447	0.257	0.005	1,93E-12
BAZ1A	1,17E-14	0,56693939	0.35	0.116	2,53E-10
PIM3	4,06E-17	0,565595679	0.317	0.056	8,75E-13
SAMD9	2,83E-16	0,559960867	0.344	0.088	6,09E-12
NOP10	2,28E-23	0,559145867	0.912	0.791	4,90E-19
TYMP	4,70E-33	0,558105636	0.964	0.567	1,01E-28
OAS2	3,05E-16	0,556266827	0.354	0.098	6,56E-12
DDIT3	8,55E-15	0,554947913	0.337	0.093	1,84E-10
SLAMF7	3,10E-14	0,553336843	0.225	0.005	6,68E-10
APOL6	8,38E-14	0,548224266	0.395	0.177	1,81E-09
VEGFA	2,05E-16	0,545920386	0.273	0.019	4,42E-12
ZC3HAV1	1,26E-14	0,535684147	0.291	0.056	2,71E-10
ZFP36L1	1,70E-08	0,534542975	0.284	0.126	0,000365954
CD48	3,49E-16	0,534483909	0.284	0.033	7,52E-12
CASP1	1,43E-13	0,525959881	0.41	0.195	3,08E-09
UBE2D3	9,31E-22	0,521117098	0.581	0.251	2,01E-17
ATF3	9,23E-13	0,519417536	0.268	0.056	1,99E-08

CSF2RB	1,22E-14	0,518544046	0.303	0.07	2,62E-10
STAT2	3,94E-14	0,517410608	0.313	0.079	8,48E-10
JUN	6,84E-36	0,516445644	0.74	0.223	1,47E-31
CCL7	1,05E-53	0,515924424	0.556	0	2,26E-49
GCH1	1,56E-14	0,514474926	0.245	0.019	3,37E-10
UBC	8,30E-23	0,512093184	0.948	0.684	1,79E-18
MAFF	9,76E-17	0,5111251	0.29	0.033	2,10E-12
TMEM140	5,85E-19	0,511085724	0.293	0.014	1,26E-14
TNFRSF1B	2,93E-14	0,504898234	0.287	0.056	6,31E-10
TLR2	1,65E-15	0,503859735	0.306	0.06	3,55E-11

Downregulated genes

	p_val	avg_logFC	pct.1	pct.2	p_val_adj
ANXA2	1,44E-53	-0,500603935	0.795	0.94	3,09E-49
ATP5MD	9,90E-45	-0,507360142	0.436	0.809	2,13E-40
TMBIM4	9,08E-98	-0,510253026	0.079	0.54	1,96E-93
SNX3	3,56E-125	-0,516023498	0.06	0.54	7,68E-121
FABP5	3,99E-46	-0,521675337	0.667	0.912	8,59E-42
YBX1	4,50E-54	-0,530966624	0.772	0.958	9,69E-50
PLIN2	1,47E-69	-0,531337527	0.051	0.363	3,16E-65
LGALS3BP	4,06E-139	-0,535149758	0.025	0.391	8,74E-135
ARPC1B	1,09E-104	-0,535884784	0.122	0.712	2,35E-100
PRDX1	3,26E-53	-0,537624639	0.626	0.949	7,03E-49
HMGN2	2,80E-130	-0,53926916	0.091	0.679	6,04E-126
NAP1L1	8,27E-152	-0,540333352	0.021	0.381	1,78E-147
TYROBP	1,93E-40	-0,540600577	0.995	1	4,16E-36
CYP27A1	1,31E-132	-0,544861379	0.023	0.367	2,83E-128
TBCA	4,47E-129	-0,544906008	0.034	0.423	9,63E-125
EIF3K	3,46E-170	-0,546754879	0.042	0.544	7,45E-166
CTSS	1,29E-43	-0,547499806	0.862	1	2,78E-39
ATP5MC3	7,33E-181	-0,54943921	0.025	0.456	1,58E-176
RPL7A	8,67E-63	-0,549710278	0.83	0.981	1,87E-58
ALOX5	1,18E-68	-0,551909415	0.058	0.377	2,55E-64
RBP4	1,28E-260	-0,552302341	0.001	0.335	2,76E-256
SUMO2	1,33E-139	-0,552601173	0.076	0.637	2,87E-135
RPSA	2,94E-71	-0,55295593	0.343	0.874	6,33E-67
CLEC12A	2,06E-149	-0,554550389	0.021	0.381	4,45E-145
HLA-DMB	5,13E-197	-0,559454527	0.009	0.353	1,10E-192
NPM1	3,08E-199	-0,561560943	0.04	0.586	6,63E-195
MCEMP1	1,26E-117	-0,564142807	0.097	0.665	2,72E-113
SCD	4,65E-222	-0,572086274	0.003	0.316	1,00E-217
TMEM258	2,37E-107	-0,572606396	0.068	0.521	5,10E-103
CTSC	9,55E-53	-0,573150242	0.733	0.963	2,06E-48
ATP5MG	2,96E-60	-0,584160313	0.574	0.963	6,38E-56
FAU	3,38E-54	-0,588323693	0.965	0.995	7,28E-50

RPL18	4,11E-87	-0,593381696	0.874	0.986	8,85E-83
ATP5MF	3,90E-160	-0,597144992	0.046	0.54	8,39E-156
S100A4	5,17E-61	-0,598597535	0.935	0.991	1,11E-56
RPS21	4,17E-87	-0,601550349	0.912	0.977	8,98E-83
RPS7	5,02E-81	-0,602791453	0.866	0.995	1,08E-76
CES1	2,72E-125	-0,608563909	0.029	0.386	5,87E-121
SKP1	8,03E-164	-0,609180014	0.071	0.67	1,73E-159
UQCR10	1,03E-89	-0,609281039	0.206	0.795	2,23E-85
NDUFS5	1,79E-243	-0,613838505	0.03	0.591	3,86E-239
UQCRQ	1,61E-145	-0,615238016	0.034	0.451	3,46E-141
BTF3	6,67E-198	-0,616830063	0.052	0.647	1,44E-193
INHBA	3,44E-143	-0,624057267	0.015	0.33	7,42E-139
RACK1	7,13E-65	-0,625903705	0.644	0.958	1,53E-60
ELOB	4,27E-65	-0,640995108	0.569	0.958	9,19E-61
SLC25A6	3,87E-277	-0,655069321	0.027	0.614	8,34E-273
TUBA1B	3,24E-64	-0,668144946	0.56	0.912	6,99E-60
SH3BGRL	0	-0,681770918	0.03	0.698	0
UQCRH	2,02E-303	-0,682023603	0.028	0.665	4,35E-299
ATP5MC2	1,37E-70	-0,683400801	0.435	0.912	2,95E-66
NDUFB2	5,84E-257	-0,684331615	0.04	0.674	1,26E-252
UQCR11	1,53E-92	-0,686014815	0.3	0.93	3,31E-88
SEC11A	9,98E-258	-0,692617191	0.028	0.595	2,15E-253
PSAP	3,40E-61	-0,699365354	0.958	0.991	7,33E-57
LST1	3,16E-101	-0,708645984	0.235	0.953	6,81E-97
RPL30	1,37E-73	-0,709191711	0.962	0.991	2,96E-69
FTL	2,82E-64	-0,712962166	1	1	6,07E-60
POLR2L	4,07E-299	-0,714304652	0.034	0.707	8,78E-295
ALOX5AP	1,20E-74	-0,720113037	0.345	0.977	2,59E-70
PABPC1	3,31E-96	-0,726567558	0.289	0.916	7,13E-92
DYNLL1	5,99E-264	-0,727647165	0.039	0.684	1,29E-259
EEF1B2	0	-0,732038778	0.031	0.712	0
VIM	5,02E-71	-0,734038325	0.963	0.986	1,08E-66
C1QC	0	-0,735220734	0.041	0.791	0
PSMA7	6,32E-87	-0,736817804	0.314	0.902	1,36E-82
ATP5ME	8,49E-249	-0,738789165	0.054	0.749	1,83E-244
NDUFA13	0	-0,741157002	0.016	0.702	0
GRN	1,71E-71	-0,744459725	0.771	0.977	3,68E-67
XIST	0	-0,745143511	0.002	0.433	0
CTSZ	1,69E-277	-0,745801579	0.047	0.758	3,64E-273
COX6C	7,05E-133	-0,762519385	0.172	0.833	1,52E-128
CD81	0	-0,768297865	0.014	0.698	0
RPL37	4,13E-109	-0,773471054	0.951	0.995	8,90E-105
EIF3E	0	-0,776828584	0.009	0.698	0
CALM2	5,91E-92	-0,778449624	0.326	0.972	1,27E-87
APLP2	2,02E-207	-0,783169309	0.098	0.879	4,36E-203
CCDC88A	4,34E-245	-0,787507816	0.013	0.451	9,35E-241
HCST	8,40E-244	-0,791407084	0.075	0.847	1,81E-239

VSIG4	0	-0,792842982	0.005	0.73	0
SSR4	0	-0,795993143	0.031	0.721	0
LIPA	7,97E-300	-0,799233568	0.017	0.558	1,72E-295
PTMA	1,74E-147	-0,806162962	0.932	0.995	3,74E-143
RPL29	1,98E-133	-0,808636826	0.853	0.986	4,27E-129
ATP5MPL	9,43E-208	-0,812941083	0.099	0.874	2,03E-203
RPL6	1,32E-113	-0,813658506	0.809	0.981	2,84E-109
CFD	2,44E-255	-0,82406517	0.046	0.712	5,26E-251
C1orf162	0	-0,824687997	0.022	0.819	0
RPL14	1,27E-143	-0,835530726	0.831	0.991	2,73E-139
RPS27L	2,61E-95	-0,839593136	0.387	0.949	5,62E-91
CAPG	1,37E-127	-0,84146694	0.211	0.898	2,96E-123
SLC11A1	6,47E-145	-0,844751846	0.058	0.563	1,39E-140
COX7C	3,44E-100	-0,868523401	0.418	0.972	7,40E-96
SNHG25	0	-0,868573421	0.001	0.512	0
NDUFB1	1,48E-257	-0,874269426	0.083	0.907	3,19E-253
MRC1	0	-0,879996936	0.005	0.772	0
FCGRT	2,22E-291	-0,883488027	0.071	0.912	4,78E-287
LGALS1	1,13E-152	-0,887942377	0.896	0.967	2,43E-148
RPS3	5,08E-154	-0,893173818	0.877	0.995	1,09E-149
RPS5	3,59E-110	-0,895672388	0.623	0.981	7,74E-106
RPS28	1,13E-85	-0,897764238	0.977	1	2,44E-81
COMMD6	1,82E-297	-0,907571886	0.067	0.893	3,93E-293
MGST3	0	-0,913519454	0.011	0.87	0
MSR1	0	-0,921808072	0.013	0.847	0
CRIP1	0	-0,924799317	0.005	0.777	0
RPS16	2,85E-134	-0,93137642	0.891	0.991	6,14E-130
GSTP1	0	-0,943171592	0.058	0.94	0
RPL3	8,43E-117	-0,943308993	0.482	0.972	1,82E-112
RPL22	4,76E-135	-0,944657013	0.772	0.977	1,02E-130
RPL5	1,34E-130	-0,949891425	0.289	0.963	2,88E-126
ALDH2	0	-0,950468917	0.005	0.847	0
UBA52	1,61E-130	-0,951926189	0.872	1	3,47E-126
NDUFA4	0	-0,951988069	0.035	0.898	0
RPS3A	1,13E-154	-0,959789821	0.849	0.991	2,43E-150
RPL19	1,65E-160	-0,962146414	0.937	0.995	3,56E-156
RPS11	4,08E-115	-0,964614092	0.385	0.991	8,78E-111
RPL8	9,13E-187	-0,968918345	0.904	1	1,97E-182
CD9	0	-0,9741297	0.04	0.865	0
MT-ND1	6,23E-54	-0,974807533	0.981	0.991	1,34E-49
MT-CO2	9,34E-52	-0,975378658	0.998	1	2,01E-47
RPL9	1,17E-148	-0,975525116	0.834	1	2,52E-144
TFRC	0	-0,976170295	0.011	0.73	0
TOMM7	0	-0,976597054	0.036	0.916	0
RPL4	0	-0,986899947	0.03	0.879	0
FBP1	0	-0,998446158	0.008	0.86	0
GPNMB	0	-0,999056341	0.015	0.874	0

PFDN5	5,60E-123	-1,003461449	0.76	0.986	1,21E-118
VAMP8	0	-1,009511385	0.037	0.902	0
CSTA	0	-1,040956247	0.057	0.86	0
OLR1	0	-1,047648117	0.023	0.879	0
MT-CYB	3,96E-58	-1,050760934	0.973	0.991	8,54E-54
RPL36	1,16E-208	-1,058647203	0.92	1	2,51E-204
RPL35A	4,66E-178	-1,066607991	0.89	0.991	1,00E-173
GCHFR	0	-1,070794593	0.011	0.87	0
UQCRB	0	-1,074860388	0.058	0.949	0
HLA-DMA	0	-1,079294452	0.027	0.944	0
RPL27	5,64E-127	-1,09659519	0.612	0.977	1,22E-122
RPS24	4,88E-191	-1,096729208	0.934	0.995	1,05E-186
RPL18A	6,75E-194	-1,098521358	0.887	1	1,45E-189
RPS13	2,62E-184	-1,105894678	0.934	0.991	5,65E-180
ACP5	0	-1,122281009	0.021	0.93	0
HLA-DQA1	0	-1,132229674	0.021	0.935	0
MT-ATP6	7,59E-63	-1,135283993	0.977	0.972	1,63E-58
RPS2	4,25E-170	-1,138754783	0.898	0.995	9,15E-166
RPS25	8,16E-160	-1,142617713	0.829	0.991	1,76E-155
UBB	1,01E-213	-1,156001202	0.149	0.986	2,18E-209
TSPO	7,16E-272	-1,175260104	0.099	0.963	1,54E-267
RPL15	1,05E-171	-1,17634829	0.834	1	2,27E-167
LTA4H	0	-1,177197704	0.027	0.902	0
RPS10	0	-1,177384291	0.015	0.958	0
RPL23A	2,25E-161	-1,194756894	0.732	0.986	4,86E-157
RPL23	0	-1,199090622	0.04	0.986	0
RPS12	1,26E-134	-1,206715642	0.948	1	2,72E-130
EEF1A1	4,04E-121	-1,208629	0.974	1	8,71E-117
RPS8	3,44E-186	-1,230467622	0.935	0.995	7,40E-182
RPS15	3,71E-191	-1,243989217	0.935	0.995	8,00E-187
RPL38	7,19E-148	-1,245110881	0.726	0.986	1,55E-143
MARCO	0	-1,2510339	0.006	0.963	0
TMSB4X	2,75E-98	-1,253726021	0.997	1	5,93E-94
RPS6	2,05E-170	-1,255564696	0.783	0.995	4,41E-166
RPL10A	0	-1,260099256	0.038	0.977	0
RPL35	2,87E-185	-1,260596814	0.812	0.986	6,18E-181
RPS4X	2,35E-169	-1,264790055	0.752	0.991	5,06E-165
RPLP1	1,61E-120	-1,273514434	0.977	1	3,48E-116
RPL7	0	-1,275296823	0.038	0.981	0
RPS23	1,45E-222	-1,290201634	0.907	0.995	3,13E-218
RPL39	5,12E-116	-1,292663064	0.971	1	1,10E-111
RETN	0	-1,298612677	0.003	0.847	0
RPS15A	1,13E-199	-1,306591095	0.919	0.995	2,44E-195
RPL12	8,93E-212	-1,316586061	0.925	0.991	1,92E-207
RPS14	5,75E-198	-1,34482597	0.908	0.995	1,24E-193
RPS27A	3,83E-175	-1,35534934	0.917	1	8,25E-171
RPL41	1,94E-115	-1,379075519	0.985	1	4,18E-111

HLA-DRB5	9,67E-151	-1,393733137	0.225	0.902	2,08E-146
RPL13	3,95E-232	-1,404518477	0.925	1	8,50E-228
RPL32	2,50E-181	-1,407770834	0.942	1	5,39E-177
RPS17	0	-1,412702573	0.011	0.916	0
RPL37A	9,70E-193	-1,423448743	0.86	0.981	2,09E-188
RPLP2	1,97E-221	-1,426468448	0.907	1	4,23E-217
RPL17	0	-1,437524795	0.041	0.94	0
RPL11	9,62E-221	-1,439233785	0.933	1	2,07E-216
MS4A7	0	-1,472138714	0.021	0.977	0
MT-ND4	1,78E-90	-1,481751439	0.977	1	3,83E-86
HLA-DPA1	1,62E-184	-1,486975764	0.729	1	3,50E-180
CST3	7,54E-206	-1,519204691	0.917	1	1,62E-201
NUPR1	0	-1,531441478	0.044	0.902	0
RPS18	1,50E-212	-1,546057176	0.857	1	3,22E-208
HLA-DQB1	0	-1,547583176	0.039	0.967	0
RPL36A	0	-1,563724326	0.029	0.967	0
HLA-DPB1	9,10E-165	-1,568618016	0.407	1	1,96E-160
CD52	0	-1,581305469	0.043	0.949	0
RPL26	2,90E-189	-1,582945125	0.774	0.995	6,24E-185
MT-CO1	1,85E-88	-1,596652057	0.994	1	3,97E-84
RPL34	2,03E-191	-1,615295566	0.937	1	4,37E-187
RPL31	1,33E-216	-1,619028076	0.16	0.935	2,86E-212
RPS29	1,37E-204	-1,631254156	0.874	0.995	2,95E-200
RPL10	6,56E-168	-1,636589434	0.946	0.995	1,41E-163
MT-ND2	2,59E-95	-1,67982918	0.978	1	5,58E-91
CD74	4,73E-127	-1,685108473	0.973	0.995	1,02E-122
RPS27	2,61E-144	-1,7347136	0.963	0.995	5,62E-140
RPL27A	0	-1,757277338	0.054	1	0
RPL13A	6,86E-175	-1,768086546	0.318	0.986	1,48E-170
RPS19	1,56E-183	-1,777588452	0.949	1	3,36E-179
RPS20	0	-1,837205182	0.059	0.986	0
RPL21	3,20E-185	-1,899249267	0.795	1	6,90E-181
HLA-DRB1	1,08E-214	-2,012691035	0.877	1	2,32E-210
MT-CO3	6,78E-106	-2,021064205	0.982	1	1,46E-101
MT-ND3	4,61E-107	-2,041210777	0.989	0.995	9,94E-103
C1QB	0	-2,140194811	0.04	0.991	0
C1QA	0	-2,14398663	0.041	1	0
FABP4	0	-2,155354673	0.008	0.972	0
HLA-DRA	9,08E-196	-2,252777733	0.932	1	1,96E-191
APOE	0	-2,384253814	0.046	1	0
LYZ	6,03E-153	-2,608397838	0.655	0.991	1,30E-148
APOC1	8,97E-206	-3,194623241	0.256	1	1,93E-201

4. DISCUSSION

4.1. Role and functionality of monocytes during COVID-19

A profound dysregulation in the myeloid cell compartment is associated with severe COVID-19 disease. COVID-19 patients present important alterations in the structure and function of the monocyte compartment which could largely contribute to the observed immune dysregulation. In this study, it was found that COVID-19 monocytes were severely impaired with regard to oxidative and glycolytic metabolism, similar to the immune-metabolic paralysis observed in patients with sepsis (Cheng *et al*, 2016). In monocytes, as well as in other types of cells, reactive oxygen species are rapidly released, and their quantification is a direct measure of the extent of activation and phagocytic activity (Vergis *et al*, 2017). As well as phagocytosis, microbial killing, and cytokine production, also the ability to perform oxidative burst in response to a challenge is influenced by the metabolic state of the cell (McBride *et al*., 2020). A large amount of oxygen is consumed during the oxidative burst, generating ROS that are key players in pathogen clearance. Both the complete burst and the immediate response were reduced in monocytes from COVID-19 patients, proving that cells from patients were inefficient and dysfunctional. It has been recently shown that severe COVID-19 also develops dysfunctional HLA-DR^{low}CD163^{+} and HLA-DR^{low},S100A^{high}, CD14^{+} monocytes. A low level of HLA-DR identified functionally impaired monocytes, but a formal proof of their status was lacking (Schulte-Schrepping *et al*, 2020). Unexpectedly, we could observe a slight - even if not statistically significant - reduction in the proportion of unstimulated monocytes producing IFN-γ in COVID-19 patients if compared to healthy subjects, opposite to the increase in the proportion of monocytes producing TNF (Figure 3c). This could explain a tendency of monocytes to deploy inflammatory responses through the production of pro-inflammatory cytokines, such as TNF, rather than responses driven by molecules with direct antiviral activity, such as IFN-γ.

Altogether, our results suggest that monocytes from COVID-19 patients accumulate dysfunctional mitochondria and are metabolically impaired if compared to those from healthy subjects. This could lead to an altered immune response, including a defective antigen presentation, with a possible increased susceptibility to secondary infections. COVID-19 related mitochondrial alterations, including a significant reduction of mitochondrial membrane potential, an impaired mitochondrial respiration, and a severe inhibition of the activity of the mitochondrial electron transport chain complexes I, III, and IV are similar to those observed in PBMCs from patients with

sepsis (Japiassu *et al*, 2011; Jang *et al*, 2019; McBride *et al*, 2020). Since monocyte functions such as, among others, phagocytosis and oxidative burst are highly energy-demanding processes, compromised bioenergetics can contribute to a poor response to infection leading to an immune paralysis similar to that described during in sepsis (Lachmandas *et al*, 2016; Cheng SC. *et al*, 2016). In general, alterations in bioenergetic status are implicated in multiorgan dysfunction and in poor outcome of the patient (Brealey *et al*, 2002).

Phenotypic analysis identified a different distribution of monocytes subsets in COVID-19 patients if compared to controls (Figures 4c and 4d). Intermediate monocytes ($CD14^{+}CD16^{++}CD38^{+}$) expressing CCR2 were increased in COVID-19 patients comparted to healthy donors. The count of circulating intermediate monocyte is commonly higher in patients with systemic infections, suggesting their relevant involvement in the rapid immune response against invading pathogens (Fingerle *et al*, 1993; Nockher *et al*, 1998). CCR2 actively mediates monocytes' mobilization and recruitment during inflammation, and monocytes expressing high levels of CCR2 are able to migrate to sites of injury where they can differentiate into inflammatory macrophages (Marsh *et al*, 2017; She *et al*, 2022). Furthermore, $CCR2^{+}$ inflammatory monocytes mediate innate NK lymphocytes and memory $CD8^{+}$ T cells activation, thus contributing to antiviral immunity (Soudja *et al*, 2012). Intermediate monocytes strongly contribute to the cytokine storm that occurs during severe COVID-19. They are mainly pro-inflammatory cells, with the capacity to secrete high levels of pro-inflammatory cytokines, including IL-6, TNF, IL-1β, and IL-8, which are increased in plasma from COVID-19 patients and dramatically contribute to hyperinflammation (De Biasi *et al*, 2020b). To counteract this phenomenon, a solution can be the reduction of intermediate monocyte count by biological drugs such as the inhibitors of anti-IL-6 receptor tocilizumab or sarilumab, that are able to decrease mortality (Guaraldi *et al*, 2020).

Different functions belong to classical monocytes, which during infections migrate to inflamed site, where they recognize and phagocytose pathogens and secrete several pro-inflammatory cytokines, leading to other immune cells recruitment to orchestrate inflammatory response (Ziegler-Heitbrock *et al*, 2010). Nonclassical monocytes predominantly remain in the vascular system, migrate along the endothelium and perform a continuous intravascular screening, in a process called patrolling (Buscher *et al*, 2017). They differ from classical monocytes for their involvement in wound healing processes and do not reach the level of production of pro-inflammatory cytokines that is typical of classical monocyte. Moreover, their promote neutrophil adhesion at the endothelial interface via the secretion of TNF (Schmidl *et al,* 2014).

TIM-3, PD-1 and its ligand PD-L1 are three molecules that regulate cell-mediated immunity and are expressed by different immune cells, including lymphocytes and monocytes (Anderson *et al,* 2007; Keir *et al*, 2008; Xia *et al*, 2018). TIM-3 is expressed on monocytes in different clinical and pathological settings, and it can synergize with Toll-like receptors (Anderson *et al*, 2007; Riva and Mehta, 2019). The precise role of TIM-3 in monocyte biology is controversial and still scarcely understood. Recent findings suggest that the PD-1/PD-L1 pathway plays an important role in the pathogenesis of sepsis, with increased expression of PD-1 or PD-L1 on monocytes being associated with increased mortality in septic patients (Zhang *et al*, 2010; Zasada *et al*, 2017). In general, expression of inhibitory immune checkpoints, like PD-1, PD-L1, and TIM-3, has been linked to a more suppressive phenotype and worse prognosis in sepsis, infections, and even cancer (Zasada *et al*, 2017; Wang *et al*, 2017; Tai *et al*, 2018). It is interesting to note that despite the heterogeneity characterizing circulating monocytes, inhibitory checkpoints, in particular PD-1 and PD-L1, were significantly over-expressed in all the three subsets of monocytes, while previous data revealed that PD-L1 was mainly expressed on nonclassical monocytes in peripheral blood (Bianchini *et al*, 2019). PD-1 and TIM-3 and their ligands, PD-L1 and galectin-9, are inhibitory pathways that regulate the balance between protective immunity and host immune-mediated damage. In plasma of patients with COVID-19 pneumonia galectin-9 levels were highly increased (De Biasi *et al*, 2020b), despite monocytes from healthy controls and COVID-19 patients showed a similar expression of TIM-3. Despite the unchanged pattern of expression of the receptor, it cannot be excluded that also in these patients, as in patients suffering from sepsis or alcoholic liver disease, the binding of soluble factors PD-L1 and galactin-9 to their receptors on monocytes is engaged leading to exhaustion and paralysis of the immune compartments (Markwick *et al*, 2015). The upregulation of PD-1 and PD-L1 on monocytes from COVID-19 raises important clinical questions for the potential intersection between COVID-19 and cancer immunotherapy, being immune checkpoint inhibitors (ICI) the pillar of cancer therapy in several tumors (Maio *et al*, 2020).

On the one hand, in the presence of the cytokine storm, ICI therapy could affect the monocytic compartment, further unbalancing the immunologic response. This, in turn, could exacerbate inflammation and therefore worsen the clinical course of COVID-19 disease. To this regard, it has been found that anti-PD-L1 therapy led to dominant gene expression changes in $CD14^+$ monocytes (Bar *et al*, 2020). On the other hand, considering the T-cell compartment, ICI therapy could mitigate the early phase of COVID-19 disease by contributing to viral clearance through the reactivation of potentially exhausted, $PD\text{-}1^+$ antigen-specific T cells (Maio *et al*, 2020). These

considerations imply that scientific evidence is now needed to provide mechanistic insights on the possible relationship between ICI and COVID-19 infection and to clarify whether ICI could be used in cancer patients with concomitant COVID-19.

In plasma from COVID-19 patients we detected high levels of IL-6, TNF, IFN-γ, IL-18 which is a clear hallmark of clearly the abnormal inflammatory response related to SARS-CoV-2 infection. In association to increased cytokine levels also soluble inflammatory chemokine such as CCL2, CCL11, CXCL10, and OPN were significantly higher if compared to healthy controls. Importantly, GM-CSF was also increased in severe COVID-19 patients, and it positively correlates with disease progression. GM-CSF is barely detectable in the blood of healthy individuals, whereas during inflammation it is secreted by several different cell types, including epithelial cells and leukocytes, and mediate two important functions of the immune response which are mature myeloid cells polarization towards a pro-inflammatory phenotype and mobilization of immature myeloid cells to sites of inflammation to restore functional immune repertoire. This process is known as emergency myelopoiesis (Silvin *et al*, 2020). GM-CSF can also enhance the ability of dendritic cells to prime T cells during antigen-specific immune responses. It was reported that the percentages of GM-CSF-expressing $CD4^+$ T cells, $CD8^+$ T cells, natural killer cells and B cells were significantly higher in the blood of patients with COVID-19 who were admitted to an intensive care unit than in healthy controls (Kreutmair *et al*, 2021). Activated lymphocytes (GM-CSF-producing T helper cells) can migrate into diseased tissue and the circulation, serving as a source of GM-CSF, thereby aiding in the recruitment and activation of new myeloid cells. Therefore, given the relevant role of this soluble factor in the pathogenesis of COVID-19, GM-CSF inhibition via neutralizing antibodies can be a promising therapeutic strategy to contrast the hyperactive host immune response observed in COVID-19.

4.2. Role and functionality of neutrophils during COVID-19

Innate immunity is our immune system's first line of defense against infections. Variability in innate immune system associated with hyperinflammation is observed in patients with severe COVID-19 and is a major contributor to the disease outcome (Chevrier *et al*, 2020; Yang *et al*, 2022). Myeloid compartment, in particular, monocytes and neutrophils are strongly affected by the infection. Hallmarks of severe COVID-19 include increased neutrophil-to-lymphocyte ratio and circulating neutrophil count, which are considered two main indicators of disease severity and predictors of mortality (Du *et al*, 2020; Liu *et al*, 2020a). Neutrophil migration and accumulation to the lung, cell activation, degranulation and NET formation increase in patients with COVID-19 pneumonia and contribute to organ damage (Veras *et al*, 2020; Fox *et al*, 2020). However, mechanisms underlying the excessive neutrophilic response were missing. In this thesis, a fine characterization of granulocytes, in particular neutrophils, from a phenotypic and metabolic point of view is reported. Among the phenotype changes occurring during the severe disease, an increase of immature neutrophils was observed, along with the presence of mature degranulated neutrophils and degranulated basophils and the concomitant expanded release of MPO and EL from degranulating neutrophils. Considering the oxidative capabilities of MPO, and the fact that elastin, the target of EL, is crucial for the functionality of the lung but significantly decreases with age, it can be hypothesized that inhibiting MPO and EL could become an additional therapeutic strategy for COVID-19.

In line with enhanced neutrophil degranulation, a significant increase in NET levels was present in plasma from COVID-19 patients, thus, confirming that neutrophils from these patients are more prone to release NET. NET involvement in the pathogenesis of severe COVID-19 has been well documented during the pandemic (Radermecker *et al*, 2020; Wang *et al*, 2020b). Excessive NET formation in COVID-19 patients is confirmed by elevated concentrations of NET-associated markers such as circulating cfDNA or MPO-DNA complexes, and EL-DNA complexes, also present in lung vessels (Veras *et al*, 2020; Ouwendijk *et al,* 2021; Janiuk *et al*, 2021). Increased NETosis drives hypercoagulability and predispose to thrombotic events associated with SARS-CoV-2 infection (Middleton *et al*, 2020). A persistent presence of neutrophils and NET was seen in several organs of deceased patients (Schurink *et al*, 2020). Neutrophils isolated from severe COVID-19 patients are more prone to NETosis and generate more NET in vitro (Veras *et al*, 2020).

In this study, it is shown that circulating neutrophils not only are degranulated and more apt to release NET, but they are also profoundly remodeled in their metabolism. In the last decade a great effort has been put in understanding metabolism and how it affects cell function. Knowledge acquired has opened new roads in leukocyte biology with a crucial impact in the immunology field. Traditionally, glycolysis has been considered as the sole source of energy for neutrophil functions. However, it is not the only one taking part in neutrophil differentiation and function (Kumar *et al*, 2019). Glycogenolysis for example has a relevant role in supporting neutrophil migration, chemotaxis, phagocytosis, and formation of NET in a hyperinflammatory setting (Robinson *et al*, 1982). Indeed, in severe COVID-19, neutrophils have enhanced glycolysis, store huge amounts of glycogen, and mobilize glycogen to perform NET. NET release as well as ROS production mainly depend on glucose availability. Hyperglycaemia, under normoxic conditions, induces NET formation (Wang *et al*, 2019), whereas glucose starvation is detrimental to neutrophils, impairing their immune response. In individuals with end-stage kidney disease, uremia induces the hyperactivation of glycogen synthase kinase 3 beta (GSK3b) which blocks glucose uptake leading to neutrophil impairment (Jawale *et al*, 2020). Genetic defects affecting mediators involved in cytosolic glucose cycling and storage such as glucose-6-phosphate transporter of the endoplasmic reticulum (G6PC3) or glucose-6-phosphate transporter (G6PT) decrease glucose availability due to the formation of toxic metabolites that arrest neutrophil maturation and functions and induce neutropenia (Veiga-da-Cunha *et al,* 2019). Neutropenia have been associated with the lack of glucose-6-phosphatase–β in mice (Cheung *et al*, 2007).

Different clinical settings such as hypoxemia observed in COVID-19, can remodel immunometabolism, which is crucial for immune cells to mediate inflammatory response. Cellular adaptations to hypoxia are mainly regulated by HIF-1α which has a relevant role in modifying metabolism in neutrophils (Sadiku *et al*, 2019; Cramer *et al*, 2003). HIF-1α is regulated both at the transcriptional and post-translational level. HIF-1α levels were indeed increased in neutrophils from severe COVID-19 patients compared to healthy donors. However, this increased protein expression was not coupled with an increase of *HIF1A* mRNA, suggesting a post-translational stabilization of HIF-1α rather its upregulation. HIF-1α leads to impaired metabolism, which in turn, leads to a functional reprograming with decreased respiratory burst, increased degranulation, and increased NETosis during COVID-19. The presence of dysfunctional oxidative burst, upon stimulation, in neutrophils from severe COVID-19 patients has been observed in a previous report (Schulte-Schrepping *et al*, 2020). Here, it is reported that oxidative burst is impaired in neutrophils from

COVID patients, but also that neutrophils' propensity to undergo NETosis is increased. Given that nicotinamide adenine dinucleotide phosphate (NADPH) oxidase (NOX) derived ROS have been implicated in promoting NETs, the coexistence of the abovementioned phenomena could appear discrepant. However, this can be explained considering that different signalling pathways can contribute to NET formation. Mechanisms involved can be both dependent and independent to the activation of NADPH-oxidase. The former relies on the formation of superoxide whose cascade culminates with cell death and NET release (Ley *et al*, 2018; Pieterse *et al*, 2018). The latter triggers NET formation in different ways, for example without requiring NOX and ROS production, but through the blebbing of the nuclear envelope and successive vesicular inside-out transportation of NET (Yipp *et al,* 2013). Notably, increased levels of HIF-1α have been observed also in BAL from COVID-19 patients suggesting that these metabolic changes could also affect infiltrating counterpart.

Previously it was reported that HIF-1α is a regulator of glycogen metabolism, and thus during hypoxia, HIF-1α induces storage of the carbohydrate glycogen which serves as a fuel reserve that can be quickly mobilized to glucose to meet energy demand (Pelletier *et al*, 2012; Pescador *et al*, 2010). Beyond its physiological functions in the liver as body's glucose reservoir, and in the muscle as energy supply for contraction, a crucial role for glycogen in controlling immune cell processes has been recently described (Ma *et al*, 2020; The *et al*, 2019). Glycogen metabolism is a key event for M1 macrophage polarization against bacterial infections and regulates T-cell memory (Zhang *et al*, 2021). In the case of infection like sepsis, the increase of glycogen granules in blood cells can help in early diagnosis, thus proper intervention, and improvement of the prognosis (Ghosh *et al*, 2020). In our study we observed a high amount of glycogen stored in neutrophils from severe COVID-19 patients whose mobilization is regulated by HIF-1α through glycogen phosphorylase L (PYGL). The identification of this pathway may have important clinical significance and provide potential therapeutic targets to halt hyperinflammation in COVID-19, as well as in various other inflammatory diseases.

Whether the metabolic rewiring in COVID-19 induced by hypoxia that triggers HIF-1α stabilization and leads to more NETosis could be enhanced also by the multicytokine exposure linked to cytokine storm, requires further investigation. Glycolysis is increased when neutrophils are simultaneously stimulated with TNF, IFN-γ, GM-CSF, IL-8. This suggests that the increased glycolysis and glycogenolysis could represent an attempt of neutrophils to adapt to changes in their microenvironment which include poor oxygenation and/or high levels of pro-inflammatory

cytokines. Moreover, these metabolic changes could also explain the increased ability of neutrophils isolated from patients to form NETs spontaneously.

In line with previous reports, in severe COVID-19 patients, an altered plasma concentration of several cytokines, chemokines, and other soluble factors involved in neutrophils' regulation is present. This revealed a prevalent pro-inflammatory pattern of response (De Biasi *et al*, 2020b; Chevrier *et al*, 2020). Key factors are IL-6, G-CSF, GM-CSF, and BAFF which are involved in the emergency granulopoiesis that occurs in inflammatory settings. Their elevated levels potentially explain the increase in activated/degranulated granulocytes that was observed (Lourda *et al*, 2021; Parsa *et al*, 2016). The increase of G-CSF likely explains the increased ability of neutrophils to perform NET. Indeed, G-CSF potentiates neutrophils to generate NET, and treatment with G-CSF neutralizing antibody reduces the sensitization toward NET formation. We observed a marked plasma increase of TNF, IL-18, IFN-γ, which are potent regulators of survival and function of neutrophils and are indicative of a broad inflammatory response.

A similar pattern was found as far as the plasma levels of FGF-β and VEGF in severe COVID-19 patients is concerned. These molecules can be produced by a huge variety of cells, including neutrophils, either spontaneously or following appropriate stimulation (Mantovani *et al*, 2011). In patients with severe COVID-19 significantly increased plasma levels of CCL2, CXCL10 and CCL20 were present, molecules that can be released by activated neutrophils to attract TH1 and TH17 cells to the site of inflammation (Mantovani *et al*, 2011; Pelletier *et al*, 2010). The existence of a loop of recruitment/activation of neutrophils/T cells with a shift toward TH17 of the T-cell response was previously observed in COVID-19 patients (De Biasi *et al*, 2020b). A correlation between the plasma concentration of some chemokines and clinical parameters, which are strong indicators of the severity of the disease, is reported in this thesis. In particular, it has to be underlined that plasma levels of CCL20 correlated with both the percentage of neutrophils and with pO_2/FiO_2, and CCL4 correlated with sO_2 and pO_2, hallmarks of COVID-19 severity.

5. CONCLUSIONS

As far as monocytes during severe COVID-19 are concerned, here it is shown that infection with SARS-CoV-2 could severely affect the monocytic compartment of innate immunity. Monocytes from severe COVID-19 patients exhibited a phenotypic, functional, and metabolic impairment, resembling the immune paralysis profile that has been associated with poor outcomes in individuals with sepsis (Weiss *et al*, 2020). It is recognized that metabolism plays a critical role in the immune response to infection, and defects in cellular metabolism such as decreased mitochondrial respiration and redox imbalance that occur upon infection are implicated in the immunologic changes (Weiss *et al*, 2020). Monocytes have indeed bioenergetic alterations, in both their glycolytic and oxidative metabolism. They failed to increase glycolysis but also, they exhibited a decreased mitochondrial respiration. Oxygen consumption rate is reduced as well as their capacity to perform oxidative burst compared to healthy controls. However, monocytes from patients with COVID-19 pneumonia remain capable to produce cytokines. Importantly, the massive and uncontrolled inflammatory status and cytokine storm syndrome typical of COVID-19 promote the initiation of phenomenon called emergency hematopoiesis (Balandra´n *et al*, 2022), that induce the commitment and expansion of bone marrow innate cell compartments as a rescue attempt against infection. For this reason, immature monocytes are released in the periphery and their count significantly increased in patients with COVID-19. Regarding the phenotype, the upregulation of inhibitory checkpoints including PD-1 and PD-L1 on monocytes from COVID-19 patients, represents a point that deserves further investigations. The blocking of checkpoints makes monocytes potential target of immunotherapy, possibly using strategies that are already available and successfully used in oncology.

Then, as far as granulocytes are concerned, it is reported in this thesis that neutrophils from patients with severe COVID-19 pneumonia have a remodeled metabolism, with increased glycolysis and glycogenolysis, which are crucial for NET formation. As already observed in several inflammatory lung diseases, including non-resolving pneumonia and ARDS, an excessive NET formation can be detrimental to the host. A high concentration of NET positively correlates with sepsis severity and organ dysfunction. NET contribute to immunothrombosis during inflammatory response due to their strong tendance in COVID-19 to aggregate with platelets and activated endothelium to form microthrombi, which occlude the vasculature and exacerbate inflammation

(Middleton *et al*, 2020; Veras *et al*, 2019; Perdomo *et al*, 2019). The early onset of these events in which host's innate immune cells interact with the virus, is followed by tissue damage such as endothelial and lung injury that can progress to pneumonia, multiorgan failure and death in worst cases of COVID-19 (Tan *et al*, 2021). During SARS-CoV-2 infection evidence of increased NET production was found not only in plasma but also in lung and in bronchoalveolar lavage fluid (Dowey *et al*, 2022). Neutrophils from patients with severe COVID-19 pneumonia have a remodeled metabolism with increased glycolysis and glycogenolysis that are crucial for NET formation. The data here reported shed new light on the role of glycogen in neutrophils' function and suggest that also neutrophil metabolism could prove an effective target for innovative therapy. In general, controlling NET formation can be a promising therapeutic strategy for COVID-19, as well as for other inflammatory diseases. Based on the findings here reported a possible strategy can be the inhibition of PYGL that leads to a reduction in NET formation. Finally, also molecules such as MPO and EL, whose production and plasma levels are extremely high in patients with COVID-19, could be novel targets for other, potential, and innovative therapies against this disease.

6. BIBLIOGRAPHY

Ackermann M, Verleden SE, Kuehnel M, et al. Pulmonary Vascular Endothelialitis, Thrombosis, and Angiogenesis in Covid-19. *N Engl J Med*. 2020;383(2):120-128. doi:10.1056/NEJMoa2015432

Ahl PJ, Hopkins RA, Xiang WW, et al. Met-Flow, a strategy for single-cell metabolic analysis highlights dynamic changes in immune subpopulations. *Commun Biol*. 2020;3(1):305. Published 2020 Jun 12. doi:10.1038/s42003-020-1027-9

Anderson AC, Anderson DE, Bregoli L, et al. Promotion of tissue inflammation by the immune receptor Tim-3 expressed on innate immune cells. *Science*. 2007;318(5853):1141-1143. doi:10.1126/science.1148536

Arachchillage DJ, Stacey A, Akor F, Scotz M, Laffan M. Thrombolysis restores perfusion in COVID-19 hypoxia. *Br J Haematol*. 2020;190(5):e270-e274. doi:10.1111/bjh.17050

Argüello RJ, Combes AJ, Char R, et al. SCENITH: A Flow Cytometry-Based Method to Functionally Profile Energy Metabolism with Single-Cell Resolution. *Cell Metab*. 2020;32(6):1063-1075.e7. doi:10.1016/j.cmet.2020.11.007

Artyomov MN, Van den Bossche J. Immunometabolism in the Single-Cell Era. Cell Metab. 2020;32(5):710-725. doi:10.1016/j.cmet.2020.09.013

Auffray C, Fogg D, Garfa M, et al. Monitoring of blood vessels and tissues by a population of monocytes with patrolling behavior. *Science*. 2007;317(5838):666-670. doi:10.1126/science.1142883

Augier S, Ciucci T, Luci C, Carle GF, Blin-Wakkach C, Wakkach A. Inflammatory blood monocytes contribute to tumor development and represent a privileged target to improve host immunosurveillance. J Immunol. 2010;185(12):7165-7173. doi:10.4049/jimmunol.0902583

Aviner R. The science of puromycin: From studies of ribosome function to applications in biotechnology. *Comput Struct Biotechnol J*. 2020;18:1074-1083. Published 2020 Apr 24. doi:10.1016/j.csbj.2020.04.014

Baig AM, Khaleeq A, Ali U, Syeda H. Evidence of the COVID-19 Virus Targeting the CNS: Tissue Distribution, Host-Virus Interaction, and Proposed Neurotropic Mechanisms. *ACS Chem Neurosci*. 2020;11(7):995-998. doi:10.1021/acschemneuro.0c00122

Balandrán JC, Zamora-Herrera G, Romo-Rodríguez R, Pelayo R. Emergency Hematopoiesis in the Pathobiology of COVID-19: The Dark Side of an Early Innate Protective Mechanism. *J Interferon Cytokine Res*. 2022;42(8):393-405. doi:10.1089/jir.2022.0028

Banerjee H, Joyner J, Stevenson M, et al. Short Communication: Studying the Role of Smart Flare Gold Nano Particles in Studying Micro RNA and Oncogene Differential Expression in Prostate Cancer Cell Lines. *J Can Res Updates*. 2017;6(2):25-28. doi:10.6000/1929-2279.2017.06.02.1

Bao J, Li C, Zhang K, Kang H, Chen W, Gu B. Comparative analysis of laboratory indexes of severe and non-severe patients infected with COVID-19. *Clin Chim Acta*. 2020;509:180-194. doi:10.1016/j.cca.2020.06.009

Bar N, Costa F, Das R, et al. Differential effects of PD-L1 versus PD-1 blockade on myeloid inflammation in human cancer. *JCI Insight*. 2020;5(12):e129353. Published 2020 Jun 18. doi:10.1172/jci.insight.129353

Becht E, McInnes L, Healy J, et al. Dimensionality reduction for visualizing single-cell data using UMAP [published online ahead of print, 2018 Dec 3]. *Nat Biotechnol*. 2018;10.1038/nbt.4314. doi:10.1038/nbt.4314

Bein T, Grasso S, Moerer O, et al. The standard of care of patients with ARDS: ventilatory settings and rescue therapies for refractory hypoxemia. *Intensive Care Med*. 2016;42(5):699-711. doi:10.1007/s00134-016-4325-4

Berra E, Benizri E, Ginouvès A, Volmat V, Roux D, Pouysségur J. HIF prolyl-hydroxylase 2 is the key oxygen sensor setting low steady-state levels of HIF-1alpha in normoxia. *EMBO J.* 2003;22(16):4082-4090. doi:10.1093/emboj/cdg392

Bianchini M, Duchêne J, Santovito D, et al. PD-L1 expression on nonclassical monocytes reveals their origin and immunoregulatory function. *Sci Immunol*. 2019;4(36):eaar3054. doi:10.1126/sciimmunol.aar3054

Boettcher S, Manz MG. Regulation of Inflammation- and Infection-Driven Hematopoiesis. *Trends Immunol*. 2017;38(5):345-357. doi:10.1016/j.it.2017.01.004

Borella R, De Biasi S, Paolini A, et al. Metabolic reprograming shapes neutrophil functions in severe COVID-19. Eur J Immunol. 2022;52(3):484-502. doi:10.1002/eji.202149481

Bost P, Giladi A, Liu Y, et al. Host-Viral Infection Maps Reveal Signatures of Severe COVID-19 Patients. *Cell*. 2020;181(7):1475-1488.e12. doi:10.1016/j.cell.2020.05.006

Brealey D, Brand M, Hargreaves I, et al. Association between mitochondrial dysfunction and severity and outcome of septic shock. *Lancet*. 2002;360(9328):219-223. doi:10.1016/S0140-6736(02)09459-X

Brinkmann V, Reichard U, Goosmann C, et al. Neutrophil extracellular traps kill bacteria. *Science*. 2004;303(5663):1532-1535. doi:10.1126/science.1092385

Burn GL, Foti A, Marsman G, Patel DF, Zychlinsky A. The Neutrophil. *Immunity*. 2021;54(7):1377-1391. doi:10.1016/j.immuni.2021.06.006

Buscher K, Marcovecchio P, Hedrick CC, Ley K. Patrolling Mechanics of Non-Classical Monocytes in Vascular Inflammation. *Front Cardiovasc Med*. 2017;4:80. Published 2017 Dec 19. doi:10.3389/fcvm.2017.00080

Cao C, Cai Z, Xiao X, et al. The architecture of the SARS-CoV-2 RNA genome inside virion. *Nat Commun*. 2021;12(1):3917. Published 2021 Jun 24. doi:10.1038/s41467-021-22785-x.

Carissimo G, Xu W, Kwok I, et al. Whole blood immunophenotyping uncovers immature neutrophil-to-VD2 T-cell ratio as an early marker for severe COVID-19. *Nat Commun*. 2020;11(1):5243. Published 2020 Oct 16. doi:10.1038/s41467-020-19080-6

Carsana L, Sonzogni A, Nasr A, et al. Pulmonary post-mortem findings in a series of COVID-19 cases from northern Italy: a two-centre descriptive study. *Lancet Infect Dis*. 2020;20(10):1135-1140. doi:10.1016/S1473-3099(20)30434-5

Chacko BK, Kramer PA, Ravi S, et al. Methods for defining distinct bioenergetic profiles in platelets, lymphocytes, monocytes, and neutrophils, and the oxidative burst from human blood. *Lab Invest*. 2013;93(6):690-700. doi:10.1038/labinvest.2013.53

Chaouat AE, Achdout H, Kol I, et al. SARS-CoV-2 receptor binding domain fusion protein efficiently neutralizes virus infection. *PLoS Pathog*. 2021;17(12):e1010175. Published 2021 Dec 20. doi:10.1371/journal.ppat.1010175

Chen EY, Tan CM, Kou Y, et al. Enrichr: interactive and collaborative HTML5 gene list enrichment analysis tool. *BMC Bioinformatics*. 2013;14:128. Published 2013 Apr 15. doi:10.1186/1471-2105-14-128

Chen G, Wu D, Guo W, et al. Clinical and immunological features of severe and moderate coronavirus disease 2019. *J Clin Invest*. 2020;130(5):2620-2629. doi:10.1172/JCI137244

Chen N, Zhou M, Dong X, et al. Epidemiological and clinical characteristics of 99 cases of 2019 novel coronavirus pneumonia in Wuhan, China: a descriptive study. *Lancet*. 2020;395(10223):507-513. doi:10.1016/S0140-6736(20)30211-7

Chen W. A potential treatment of COVID-19 with TGF-β blockade. *Int J Biol Sci*. 2020;16(11):1954-1955. Published 2020 Apr 21. doi:10.7150/ijbs.46891

Cheng L, Li H, Li L, et al. Ferritin in the coronavirus disease 2019 (COVID-19): A systematic review and meta-analysis. *J Clin Lab Anal*. 2020;34(10):e23618. doi:10.1002/jcla.23618

Cheng SC, Scicluna BP, Arts RJ, et al. Broad defects in the energy metabolism of leukocytes underlie immunoparalysis in sepsis. *Nat Immunol*. 2016;17(4):406-413. doi:10.1038/ni.3398

Cheung YY, Kim SY, Yiu WH, et al. Impaired neutrophil activity and increased susceptibility to bacterial infection in mice lacking glucose-6-phosphatase-beta. *J Clin Invest*. 2007;117(3):784-793. doi:10.1172/JCI30443

Chevrier S, Zurbuchen Y, Cervia C, et al. A distinct innate immune signature marks progression from mild to severe COVID-19. *Cell Rep Med*. 2020;2(1):100166. Published 2020 Dec 26. doi:10.1016/j.xcrm.2020.100166

Chilunda V, Martinez-Aguado P, Xia LC, et al. Transcriptional Changes in CD16+ Monocytes May Contribute to the Pathogenesis of COVID-19. *Front Immunol*. 2021;12:665773. Published 2021 May 24. doi:10.3389/fimmu.2021.665773

Chimen M, Yates CM, McGettrick HM, et al. Monocyte Subsets Coregulate Inflammatory Responses by Integrated Signaling through TNF and IL-6 at the Endothelial Cell Interface. *J Immunol*. 2017;198(7):2834-2843. doi:10.4049/jimmunol.1601281

Chu H, Zhou J, Wong BH, et al. Productive replication of Middle East respiratory syndrome coronavirus in monocyte-derived dendritic cells modulates innate immune response. *Virology*. 2014;454-455:197-205. doi:10.1016/j.virol.2014.02.018

Codo AC, Davanzo GG, Monteiro LB, et al. Elevated Glucose Levels Favor SARS-CoV-2 Infection and Monocyte Response through a HIF-1α/Glycolysis-Dependent Axis [published correction appears in Cell Metab. 2020 Sep 1;32(3):498-499]. *Cell Metab*. 2020;32(3):437-446.e5. doi:10.1016/j.cmet.2020.07.007

Coleman CM, Frieman MB. Coronaviruses: important emerging human pathogens. *J Virol*. 2014;88(10):5209-5212. doi:10.1128/JVI.03488-13.

Cordero MD, De Miguel M, Moreno Fernández AM, et al. Mitochondrial dysfunction and mitophagy activation in blood mononuclear cells of fibromyalgia patients: implications in the pathogenesis of the disease. *Arthritis Res Ther*. 2010;12(1):R17. doi:10.1186/ar2918

Cossarizza A, Baccarani-Contri M, Kalashnikova G, Franceschi C. A new method for the cytofluorimetric analysis of mitochondrial membrane potential using the J-aggregate forming lipophilic cation 5,5',6,6'-tetrachloro-1,1',3,3'-tetraethylbenzimidazolcarbocyanine iodide (JC-1). *Biochem Biophys Res Commun*. 1993;197(1):40-45. doi:10.1006/bbrc.1993.2438

Cossarizza A, Chang HD, Radbruch A, et al. Guidelines for the use of flow cytometry and cell sorting in immunological studies (third edition). *Eur J Immunol*. 2021;51(12):2708-3145. doi:10.1002/eji.202170126

Cottet-Rousselle C, Ronot X, Leverve X, Mayol JF. Cytometric assessment of mitochondria using fluorescent probes. *Cytometry A*. 2011;79(6):405-425. doi:10.1002/cyto.a.21061

Cramer T, Yamanishi Y, Clausen BE, et al. HIF-1alpha is essential for myeloid cell-mediated inflammation [published correction appears in *Cell*. 2003 May 2;113(3):419]. *Cell*. 2003;112(5):645-657. doi:10.1016/s0092-8674(03)00154-5

Cueno ME, Imai K. Structural Comparison of the SARS CoV 2 Spike Protein Relative to Other Human-Infecting Coronaviruses. *Front Med (Lausanne*). 2021;7:594439. Published 2021 Jan 14. doi:10.3389/fmed.2020.594439

Cui J, Li F, Shi ZL. Origin and evolution of pathogenic coronaviruses. *Nat Rev Microbiol*. 2019;17(3):181-192. doi:10.1038/s41579-018-0118-9

Cyprian FS, Suleman M, Abdelhafez I, et al. Complement C5a and Clinical Markers as Predictors of COVID-19 Disease Severity and Mortality in a Multi-Ethnic Population. *Front Immunol*. 2021;12:707159. Published 2021 Dec 13. doi:10.3389/fimmu.2021.707159

Davison GM, Nkambule BB, Mkandla Z, et al. Platelet, monocyte and neutrophil activation and glucose tolerance in South African Mixed Ancestry individuals. *Sci Rep*. 2017;7:40329. Published 2017 Jan 16. doi:10.1038/srep40329

De Biasi S, Gibellini L, Cossarizza A. Uncompensated Polychromatic Analysis of Mitochondrial Membrane Potential Using JC-1 and Multilaser Excitation. *Curr Protoc Cytom*. 2015;72:7.32.1-7.32.11. Published 2015 Apr 1. doi:10.1002/0471142956.cy0732s72

De Biasi S, Lo Tartaro D, Meschiari M, et al. Expansion of plasmablasts and loss of memory B cells in peripheral blood from COVID-19 patients with pneumonia. *Eur J Immunol*. 2020a;50(9):1283-1294. doi:10.1002/eji.202048838

De Biasi S, Meschiari M, Gibellini L, et al. Marked T cell activation, senescence, exhaustion and skewing towards TH17 in patients with COVID-19 pneumonia. *Nat Commun.* 2020b;11(1):3434. Published 2020 Jul 6. doi:10.1038/s41467-020-17292-4

De Biasi S, Simone AM, Bianchini E, et al. Mitochondrial functionality and metabolism in T cells from progressive multiple sclerosis patients. *Eur J Immunol*. 2019;49(12):2204-2221. doi:10.1002/eji.201948223

de Wit E, van Doremalen N, Falzarano D, Munster VJ. SARS and MERS: recent insights into emerging coronaviruses. *Nat Rev Microbiol*. 2016;14(8):523-534. doi:10.1038/nrmicro.2016.81

Dhont S, Derom E, Van Braeckel E, Depuydt P, Lambrecht BN. The pathophysiology of 'happy' hypoxemia in COVID-19. *Respir Res*. 2020;21(1):198. Published 2020 Jul 28. doi:10.1186/s12931-020-01462-5

Dowey R, Cole J, Thompson AAR, et al. Enhanced neutrophil extracellular trap formation in COVID-19 is inhibited by the protein kinase C inhibitor ruboxistaurin. *ERJ Open Res*. 2022;8(2):00596-2021. Published 2022 Apr 4. doi:10.1183/23120541.00596-2021

Du RH, Liang LR, Yang CQ, et al. Predictors of mortality for patients with COVID-19 pneumonia caused by SARS-CoV-2: a prospective cohort study [published correction appears in Eur Respir J. 2020 Sep 24;56(3):]. *Eur Respir J*. 2020;55(5):2000524. Published 2020 May 7. doi:10.1183/13993003.00524-2020

Ellery PJ, Tippett E, Chiu YL, et al. The CD16+ monocyte subset is more permissive to infection and preferentially harbors HIV-1 in vivo. *J Immunol*. 2007;178(10):6581-6589. doi:10.4049/jimmunol.178.10.6581

Feng X, Li S, Sun Q, et al. Immune-Inflammatory Parameters in COVID-19 Cases: A Systematic Review and Meta-Analysis. *Front Med (Lausanne)*. 2020;7:301. Published 2020. Jun 9. doi:10.3389/fmed.2020.00301

Fingerle G, Pforte A, Passlick B, Blumenstein M, Ströbel M, Ziegler-Heitbrock HW. The novel subset of CD14+/CD16+ blood monocytes is expanded in sepsis patients. *Blood*. 1993;82(10):3170-3176.

Fox S, Leitch AE, Duffin R, Haslett C, Rossi AG. Neutrophil apoptosis: relevance to the innate immune response and inflammatory disease. *J Innate Immun*. 2010;2(3):216-227. doi:10.1159/000284367

Fox SE, Akmatbekov A, Harbert JL, Li G, Quincy Brown J, Vander Heide RS. Pulmonary and cardiac pathology in African American patients with COVID-19: an autopsy series from New Orleans. *Lancet Respir Med*. 2020;8(7):681-686. doi:10.1016/S2213-2600(20)30243-5

Galani IE, Rovina N, Lampropoulou V, et al. Untuned antiviral immunity in COVID-19 revealed by temporal type I/III interferon patterns and flu comparison. *Nat Immunol*. 2021;22(1):32-40. doi:10.1038/s41590-020-00840-x

Gao YM, Xu G, Wang B, Liu BC. Cytokine storm syndrome in coronavirus disease 2019: A narrative review. *J Intern Med*. 2021;289(2):147-161. doi:10.1111/joim.13144

Gardie B, Percy MJ, Hoogewijs D, et al. The role of PHD2 mutations in the pathogenesis of erythrocytosis. Hypoxia (Auckl). 2014;2:71-90. Published 2014 Jul 1. doi:10.2147/HP.S54455

Gaspar JM, Velloso LA. Hypoxia Inducible Factor as a Central Regulator of Metabolism - Implications for the Development of Obesity. *Front Neurosci*. 2018;12:813. Published 2018 Nov 1. doi:10.3389/fnins.2018.00813

Gautier EL, Ivanov S, Lesnik P, Randolph GJ. Local apoptosis mediates clearance of macrophages from resolving inflammation in mice. *Blood*. 2013;122(15):2714-2722. doi:10.1182/blood-2013-01-478206

Ghosh A, Nanda P, Tripathy S, Sinha MK. Glycogen Accumulation in Neutrophil Can Be a Marker of Sepsis. *Int J Appl Basic Med Res*. 2020;10(1):22-24. doi:10.4103/ijabmr.IJABMR_350_18

Giamarellos-Bourboulis EJ, Netea MG, Rovina N, et al. Complex Immune Dysregulation in COVID-19 Patients with Severe Respiratory Failure. *Cell Host Microbe*. 2020;27(6):992-1000.e3. doi:10.1016/j.chom.2020.04.009

Gibellini L, De Biasi S, Paolini A, et al. Altered bioenergetics and mitochondrial dysfunction of monocytes in patients with COVID-19 pneumonia. EMBO Mol Med. 2020;12(12):e13001. doi:10.15252/emmm.202013001

Gibellini L, Losi L, De Biasi S, et al. LonP1 Differently Modulates Mitochondrial Function and Bioenergetics of Primary Versus Metastatic Colon Cancer Cells. *Front Oncol*. 2018;8:254. Published 2018 Jul 9. doi:10.3389/fonc.2018.00254

Gibellini L, Pinti M, Bartolomeo R, et al. Inhibition of Lon protease by triterpenoids alters mitochondria and is associated to cell death in human cancer cells. *Oncotarget*. 2015;6(28):25466-25483. doi:10.18632/oncotarget.4510

Gibson PG, Qin L, Puah SH. COVID-19 acute respiratory distress syndrome (ARDS): clinical features and differences from typical pre-COVID-19 ARDS. *Med J Aust*. 2020;213(2):54-56.e1. doi:10.5694/mja2.50674

Gill SE, Dos Santos CC, O'Gorman DB, et al. Transcriptional profiling of leukocytes in critically ill COVID19 patients: implications for interferon response and coagulation. *Intensive Care Med Exp*. 2020;8(1):75. Published 2020 Dec 11. doi:10.1186/s40635-020-00361-9

Gordon S, Taylor PR. Monocyte and macrophage heterogeneity. *Nat Rev Immunol*. 2005;5(12):953-964. doi:10.1038/nri1733

Green CA, Quraishi MN, Shabir S, et al. Screening faecal microbiota transplant donors for SARS-CoV-2 by molecular testing of stool is the safest way forward. *Lancet Gastroenterol Hepatol*. 2020;5(6):531. doi:10.1016/S2468-1253(20)30089-3

Grieb P, Swiatkiewicz M, Prus K, Rejdak K. Hypoxia may be a determinative factor in COVID-19 progression. *Curr Res Pharmacol Drug Discov.* 2021;2:100030. doi:10.1016/j.crphar.2021.100030

Griffiths MJD, McAuley DF, Perkins GD, et al. Guidelines on the management of acute respiratory distress syndrome. *BMJ Open Respir Res*. 2019;6(1):e000420. Published 2019 May 24. doi:10.1136/bmjresp-2019-000420

Guan WJ, Ni ZY, Hu Y, et al. Clinical Characteristics of Coronavirus Disease 2019 in China. *N Engl J Med*. 2020;382(18):1708-1720. doi:10.1056/NEJMoa2002032

Guaraldi G, Meschiari M, Cozzi-Lepri A, et al. Tocilizumab in patients with severe COVID-19: a retrospective cohort study [published correction appears in Lancet Rheumatol. 2020 Oct;2(10):e591]. *Lancet Rheumatol*. 2020;2(8):e474-e484. doi:10.1016/S2665-9913(20)30173-9

Guo YR, Cao QD, Hong ZS, et al. The origin, transmission and clinical therapies on coronavirus disease 2019 (COVID-19) outbreak - an update on the status. *Mil Med Res*. 2020;7(1):11. Published 2020 Mar 13. doi:10.1186/s40779-020-00240-0

Hadjadj J, Yatim N, Barnabei L, et al. Impaired type I interferon activity and inflammatory responses in severe COVID-19 patients. *Science*. 2020;369(6504):718-724. doi:10.1126/science.abc6027

Hafemeister C, Satija R. Normalization and variance stabilization of single-cell RNA-seq data using regularized negative binomial regression. *Genome Biol*. 2019;20(1):296. Published 2019 Dec 23. doi:10.1186/s13059-019-1874-1

Hazeldine J, Lord JM. Neutrophils and COVID-19: Active Participants and Rational Therapeutic Targets. *Front Immunol*. 2021;12:680134. Published 2021 Jun 2. doi:10.3389/fimmu.2021.680134

Hidalgo San Jose L, Signer RAJ. Cell-type-specific quantification of protein synthesis in vivo. *Nat Protoc*. 2019;14(2):441-460. doi:10.1038/s41596-018-0100-z

Hikmet F, Méar L, Edvinsson Å, Micke P, Uhlén M, Lindskog C. The protein expression profile of ACE2 in human tissues. *Mol Syst Biol*. 2020;16(7):e9610. doi:10.15252/msb.20209610

Hitomi Y, Miyamura M, Mori S, et al. Intermittent hypobaric hypoxia increases the ability of neutrophils to generate superoxide anion in humans. *Clin Exp Pharmacol Physiol*. 2003;30(9):659-664. doi:10.1046/j.1440-1681.2003.03891.x

Hoffmann M, Kleine-Weber H, Schroeder S, et al. SARS-CoV-2 Cell Entry Depends on ACE2 and TMPRSS2 and Is Blocked by a Clinically Proven Protease Inhibitor. *Cell.* 2020;181(2):271-280.e8. doi:10.1016/j.cell.2020.02.052

Hoxhaj G, Ben-Sahra I, Lockwood SE, et al. Direct stimulation of NADP+ synthesis through Akt-mediated phosphorylation of NAD kinase. *Science*. 2019;363(6431):1088-1092. doi:10.1126/science.aau3903

Huang C, Wang Y, Li X, et al. Clinical features of patients infected with 2019 novel coronavirus in Wuhan, China [published correction appears in Lancet. 2020 Jan 30;]. *Lancet*. 2020;395(10223):497-506. doi:10.1016/S0140-6736(20)30183-5

Hui DS, Joynt GM, Wong KT, et al. Impact of severe acute respiratory syndrome (SARS) on pulmonary function, functional capacity and quality of life in a cohort of survivors. *Thorax*. 2005;60(5):401-409. doi:10.1136/thx.2004.030205

Jakubzick C, Gautier EL, Gibbings SL, et al. Minimal differentiation of classical monocytes as they survey steady-state tissues and transport antigen to lymph nodes. *Immunity*. 2013;39(3):599-610. doi:10.1016/j.immuni.2013.08.007

Jakubzick CV, Randolph GJ, Henson PM. Monocyte differentiation and antigen-presenting functions. *Nat Rev Immunol*. 2017;17(6):349-362. doi:10.1038/nri.2017.28

Jang DH, Orloski CJ, Owiredu S, Shofer FS, Greenwood JC, Eckmann DM. Alterations in Mitochondrial Function in Blood Cells Obtained From Patients With Sepsis Presenting to an Emergency Department. *Shock*. 2019;51(5):580-584. doi:10.1097/SHK.0000000000001208

Janiuk K, Jabłońska E, Garley M. Significance of NETs Formation in COVID-19. *Cells*. 2021;10(1):151. Published 2021 Jan 14. doi:10.3390/cells10010151

Japiassú AM, Santiago AP, d'Avila JC, et al. Bioenergetic failure of human peripheral blood monocytes in patients with septic shock is mediated by reduced F1Fo adenosine-5'-triphosphate synthase activity. *Crit Care Med*. 2011;39(5):1056-1063. doi:10.1097/CCM.0b013e31820eda5c

Jawale CV, Ramani K, Li DD, et al. Restoring glucose uptake rescues neutrophil dysfunction and protects against systemic fungal infection in mouse models of kidney disease. *Sci Transl Med*. 2020;12(548):eaay5691. doi:10.1126/scitranslmed.aay5691

Jeon JH, Hong CW, Kim EY, Lee JM. Current Understanding on the Metabolism of Neutrophils. *Immune Netw*. 2020;20(6):e46. Published 2020 Dec 24. doi:10.4110/in.2020.20.e46

Kano R, Sato A, Sobukawa H, et al. Short communication: ELISA system for screening of bovine mastitis caused by Prototheca zopfii. *J Dairy Sci*. 2016;99(8):6590-6593. doi:10.3168/jds.2016-11168

Kapellos TS, Bonaguro L, Gemünd I, et al. Human Monocyte Subsets and Phenotypes in Major Chronic Inflammatory Diseases. *Front Immunol*. 2019;10:2035. Published 2019 Aug 30. doi:10.3389/fimmu.2019.02035

Keir ME, Butte MJ, Freeman GJ, Sharpe AH. PD-1 and its ligands in tolerance and immunity. *Annu Rev Immunol*. 2008;26:677-704. doi:10.1146/annurev.immunol.26.021607.090331

Kim SY, Jun HS, Mead PA, Mansfield BC, Chou JY. Neutrophil stress and apoptosis underlie myeloid dysfunction in glycogen storage disease type Ib. *Blood*. 2008;111(12):5704-5711. doi:10.1182/blood-2007-12-129114

Kramer PA, Ravi S, Chacko B, Johnson MS, Darley-Usmar VM. A review of the mitochondrial and glycolytic metabolism in human platelets and leukocytes: implications for their use as bioenergetic biomarkers. *Redox Biol*. 2014;2:206-210. Published 2014 Jan 10. doi:10.1016/j.redox.2013.12.026

Kreutmair S, Unger S, Núñez NG, et al. Distinct immunological signatures discriminate severe COVID-19 from non-SARS-CoV-2-driven critical pneumonia [published correction appears in Immunity. 2022 Feb 8;55(2):366-375]. *Immunity*. 2021;54(7):1578-1593.e5. doi:10.1016/j.immuni.2021.05.002

Ku HC, Cheng CF. Master Regulator Activating Transcription Factor 3 (ATF3) in Metabolic Homeostasis and Cancer. *Front Endocrinol* (Lausanne). 2020;11:556. Published 2020 Aug 14. doi:10.3389/fendo.2020.00556

Kuleshov MV, Jones MR, Rouillard AD, et al. Enrichr: a comprehensive gene set enrichment analysis web server 2016 updateYu. *Nucleic Acids Res*. 2016;44(W1):W90-W97. doi:10.1093/nar/gkw377

Kumar S, Dikshit M. Metabolic Insight of Neutrophils in Health and Disease. *Front Immunol*. 2019;10:2099. Published 2019 Sep 20. doi:10.3389/fimmu.2019.02099

Kyriazopoulou E, Leventogiannis K, Norrby-Teglund A, et al. Macrophage activation-like syndrome: an immunological entity associated with rapid progression to death in sepsis. *BMC Med*. 2017;15(1):172. Published 2017 Sep 18. doi:10.1186/s12916-017-0930-5

L.A.B. Jun Xia, Daniel C. Link, ER Stress-Induced Expression of CCAAT/Enhancer Binding Protein Gamma (C/EBPG) May Contribute to the Block in Granulocytic Differentiation in Severe Congenital Neutropenia, *Blood* 120(21) (2012).

Lachmandas E, Boutens L, Ratter JM, et al. Microbial stimulation of different Toll-like receptor signalling pathways induces diverse metabolic programmes in human monocytes. *Nat Microbiol*. 2016;2:16246. Published 2016 Dec 19. doi:10.1038/nmicrobiol.2016.246

Lachmann G, Knaak C, Vorderwülbecke G, et al. Hyperferritinemia in Critically Ill Patients. *Crit Care Med*. 2020;48(4):459-465. doi:10.1097/CCM.0000000000004131

Lahm H, Doppler S, Dreßen M, et al. Live fluorescent RNA-based detection of pluripotency gene expression in embryonic and induced pluripotent stem cells of different species. *Stem Cells*. 2015;33(2):392-402. doi:10.1002/stem.1872

Lam TT, Jia N, Zhang YW, et al. Identifying SARS-CoV-2-related coronaviruses in Malayan pangolins. *Nature*. 2020;583(7815):282-285. doi:10.1038/s41586-020-2169-0.

Lawrence SM, Corriden R, Nizet V. The Ontogeny of a Neutrophil: Mechanisms of Granulopoiesis and Homeostasis. *Microbiol Mol Biol Rev*. 2018;82(1):e00057-17. Published 2018 Feb 7. doi:10.1128/MMBR.00057-17

Lee J, Tam H, Adler L, Ilstad-Minnihan A, Macaubas C, Mellins ED. The MHC class II antigen presentation pathway in human monocytes differs by subset and is regulated by cytokines. *PLoS One*. 2017;12(8):e0183594. Published 2017 Aug 23. doi:10.1371/journal.pone.0183594

Leisman DE, Ronner L, Pinotti R, et al. Cytokine elevation in severe and critical COVID-19: a rapid systematic review, meta-analysis, and comparison with other inflammatory syndromes. *Lancet Respir Med*. 2020;8(12):1233-1244. doi:10.1016/S2213-2600(20)30404-5

Ley K, Hoffman HM, Kubes P, et al. Neutrophils: New insights and open questions. *Sci Immunol*. 2018;3(30):eaat4579. doi:10.1126/sciimmunol.aat4579

Li F, Li W, Farzan M, Harrison SC. Structure of SARS coronavirus spike receptor-binding domain complexed with receptor. *Science*. 2005;309(5742):1864-1868.

Li F. Structure, Function, and Evolution of Coronavirus Spike Proteins. *Annu Rev Virol*. 2016;3(1):237-261. doi:10.1146/annurev-virology-110615-042301

Li Q, Guan X, Wu P, et al. Early Transmission Dynamics in Wuhan, China, of Novel Coronavirus-Infected Pneumonia. *N Engl J Med*. 2020;382(13):1199-1207. doi:10.1056/NEJMoa2001316

Liew PX, Kubes P. The Neutrophil's Role During Health and Disease. *Physiol Rev*. 2019;99(2):1223-1248. doi:10.1152/physrev.00012.2018

Lindqvist LM, Tandoc K, Topisirovic I, Furic L. Cross-talk between protein synthesis, energy metabolism and autophagy in cancer. *Curr Opin Genet Dev*. 2018;48:104-111. doi:10.1016/j.gde.2017.11.003

Liu J, Li S, Liu J, et al. Longitudinal characteristics of lymphocyte responses and cytokine profiles in the peripheral blood of SARS-CoV-2 infected patients. *EBioMedicine*. 2020a;55:102763. doi:10.1016/j.ebiom.2020.102763

Liu J, Liu Y, Xiang P, et al. Neutrophil-to-lymphocyte ratio predicts critical illness patients with 2019 coronavirus disease in the early stage. *J Transl Med*. 2020b;18(1):206. Published 2020 May 20. doi:10.1186/s12967-020-02374-0

Loganathan S, Kuppusamy M, Wankhar W, et al. Angiotensin-converting enzyme 2 (ACE2): COVID 19 gate way to multiple organ failure syndromes. *Respir Physiol Neurobiol*. 2021;283:103548. doi:10.1016/j.resp.2020.103548

Lourda M, Dzidic M, Hertwig L, et al. High-dimensional profiling reveals phenotypic heterogeneity and disease-specific alterations of granulocytes in COVID-19. *Proc Natl Acad Sci U S A*. 2021;118(40):e2109123118. doi:10.1073/pnas.2109123118

Ma J, Wei K, Liu J, et al. Glycogen metabolism regulates macrophage-mediated acute inflammatory responses. *Nat Commun*. 2020;11(1):1769. Published 2020 Apr 14. doi:10.1038/s41467-020-15636-8

Machhi J, Herskovitz J, Senan AM, et al. The Natural History, Pathobiology, and Clinical Manifestations of SARS-CoV-2 Infections. J Neuroimmune Pharmacol. 2020;15(3):359-386. doi:10.1007/s11481-020-09944-5

MacIntyre NR. Supporting oxygenation in acute respiratory failure. *Respir Care*. 2013;58(1):142-150. doi:10.4187/respcare.02087

Maio M, Hamid O, Larkin J, et al. Immune Checkpoint Inhibitors for Cancer Therapy in the COVID-19 Era. *Clin Cancer Res*. 2020;26(16):4201-4205. doi:10.1158/1078-0432.CCR-20-1657

Manning HL, Schwartzstein RM. Pathophysiology of dyspnea. *N Engl J Med*. 1995;333(23):1547-1553. doi:10.1056/NEJM199512073332307

Mantovani A, Cassatella MA, Costantini C, Jaillon S. Neutrophils in the activation and regulation of innate and adaptive immunity. *Nat Rev Immunol*. 2011;11(8):519-531. Published 2011 Jul 25. doi:10.1038/nri3024

Markwick LJ, Riva A, Ryan JM, et al. Blockade of PD1 and TIM3 restores innate and adaptive immunity in patients with acute alcoholic hepatitis. *Gastroenterology*. 2015;148(3):590-602.e10. doi:10.1053/j.gastro.2014.11.041

Marsh SA, Arthur HM, Spyridopoulos I. The secret life of nonclassical monocytes. *Cytometry A*. 2017;91(11):1055-1058. doi:10.1002/cyto.a.23280

Martín-Montañez E, Pavia J, Valverde N, et al. The S1P mimetic fingolimod phosphate regulates mitochondrial oxidative stress in neuronal cells. *Free Radic Biol Med*. 2019;137:116-130. doi:10.1016/j.freeradbiomed.2019.04.022

Mason JA, Cockfield JA, Pape DJ, et al. SGK1 signaling promotes glucose metabolism and survival in extracellular matrix detached cells. *Cell Rep.* 2021;34(11):108821. doi:10.1016/j.celrep.2021.108821

Masters PS. The molecular biology of coronaviruses. *Adv Virus Res*. 2006;66:193-292. doi:10.1016/S0065-3527(06)66005-3

Masucci MT, Minopoli M, Del Vecchio S, Carriero MV. The Emerging Role of Neutrophil Extracellular Traps (NETs) in Tumor Progression and Metastasis. *Front Immunol*. 2020;11:1749. Published 2020 Sep 16. doi:10.3389/fimmu.2020.01749

Mathias JR, Perrin BJ, Liu TX, Kanki J, Look AT, Huttenlocher A. Resolution of inflammation by retrograde chemotaxis of neutrophils in transgenic zebrafish. *J Leukoc Biol*. 2006;80(6):1281-1288. doi:10.1189/jlb.0506346

McBride MA, Owen AM, Stothers CL, et al. The Metabolic Basis of Immune Dysfunction Following Sepsis and Trauma. *Front Immunol*. 2020;11:1043. Published 2020 May 29. doi:10.3389/fimmu.2020.01043

Merad M, Martin JC. Pathological inflammation in patients with COVID-19: a key role for monocytes and macrophages [published correction appears in Nat Rev Immunol. 2020 Jun 2;]. *Nat Rev Immunol*. 2020;20(6):355-362. doi:10.1038/s41577-020-0331-4

Mesas AE, Cavero-Redondo I, Álvarez-Bueno C, et al. Predictors of in-hospital COVID-19 mortality: A comprehensive systematic review and meta-analysis exploring differences by age, sex and health conditions. *PLoS One*. 2020;15(11):e0241742. Published 2020 Nov 3. doi:10.1371/journal.pone.0241742

Middleton EA, He XY, Denorme F, et al. Neutrophil extracellular traps contribute to immunothrombosis in COVID-19 acute respiratory distress syndrome. *Blood*. 2020;136(10):1169-1179. doi:10.1182/blood.2020007008

Moore JB, June CH. Cytokine release syndrome in severe COVID-19. *Science*. 2020;368(6490):473-474. doi:10.1126/science.abb8925

Nicholas D, Proctor EA, Raval FM, et al. Advances in the quantification of mitochondrial function in primary human immune cells through extracellular flux analysis. *PLoS One*. 2017;12(2):e0170975. Published 2017 Feb 8. doi:10.1371/journal.pone.0170975

Nockher WA, Scherberich JE. Expanded CD14+ CD16+ monocyte subpopulation in patients with acute and chronic infections undergoing hemodialysis. *Infect Immun*. 1998;66(6):2782-2790. doi:10.1128/IAI.66.6.2782-2790.1998

Nowicka M, Krieg C, Crowell HL, et al. CyTOF workflow: differential discovery in high-throughput high-dimensional cytometry datasets. *F1000Res*. 2017;6:748. Published 2017 May 26. doi:10.12688/f1000research.11622.3

O'Neill LA, Kishton RJ, Rathmell J. A guide to immunometabolism for immunologists. *Nat Rev Immunol*. 2016;16(9):553-565. doi:10.1038/nri.2016.70

Onofrio L, Caraglia M, Facchini G, Margherita V, Placido S, Buonerba C. Toll-like receptors and COVID-19: a two-faced story with an exciting ending. *Future Sci OA*. 2020;6(8):FSO605. Published 2020 Jul 30. doi:10.2144/fsoa-2020-0091

Osuchowski MF, Winkler MS, Skirecki T, et al. The COVID-19 puzzle: deciphering pathophysiology and phenotypes of a new disease entity. *Lancet Respir Med*. 2021;9(6):622-642. doi:10.1016/S2213-2600(21)00218-6

Ouwendijk WJD, Raadsen MP, van Kampen JJA, et al. High Levels of Neutrophil Extracellular Traps Persist in the Lower Respiratory Tract of Critically Ill Patients With Coronavirus Disease 2019. *J Infect Dis*. 2021;223(9):1512-1521. doi:10.1093/infdis/jiab050

Pacella I, Procaccini C, Focaccetti C, et al. Fatty acid metabolism complements glycolysis in the selective regulatory T cell expansion during tumor growth. *Proc Natl Acad Sci U S A*. 2018;115(28):E6546-E6555. doi:10.1073/pnas.1720113115

Palframan RT, Jung S, Cheng G, et al. Inflammatory chemokine transport and presentation in HEV: a remote control mechanism for monocyte recruitment to lymph nodes in inflamed tissues. *J Exp Med*. 2001;194(9):1361-1373. doi:10.1084/jem.194.9.1361

Parsa R, Lund H, Georgoudaki AM, et al. BAFF-secreting neutrophils drive plasma cell responses during emergency granulopoiesis. *J Exp Med*. 2016;213(8):1537-1553. doi:10.1084/jem.20150577

Pelgrom LR, van der Ham AJ, Everts B. Analysis of TLR-Induced Metabolic Changes in Dendritic Cells Using the Seahorse XF(e)96 Extracellular Flux Analyzer. *Methods Mol Biol*. 2016;1390:273-285. doi:10.1007/978-1-4939-3335-8_17

Pelletier J, Bellot G, Gounon P, Lacas-Gervais S, Pouysségur J, Mazure NM. Glycogen Synthesis is Induced in Hypoxia by the Hypoxia-Inducible Factor and Promotes Cancer Cell Survival. *Front Oncol*. 2012;2:18. Published 2012 Feb 28. doi:10.3389/fonc.2012.00018

Pelletier M, Maggi L, Micheletti A, et al. Evidence for a cross-talk between human neutrophils and Th17 cells. *Blood*. 2010;115(2):335-343. doi:10.1182/blood-2009-04-216085

Perdomo J, Leung HHL, Ahmadi Z, et al. Neutrophil activation and NETosis are the major drivers of thrombosis in heparin-induced thrombocytopenia. *Nat Commun*. 2019;10(1):1322. Published 2019 Mar 21. doi:10.1038/s41467-019-09160-7

Pescador N, Villar D, Cifuentes D, et al. Hypoxia promotes glycogen accumulation through hypoxia inducible factor (HIF)-mediated induction of glycogen synthase 1. *PLoS One*. 2010;5(3):e9644. Published 2010 Mar 12. doi:10.1371/journal.pone.0009644

Pieterse E, Rother N, Yanginlar C, et al. Cleaved N-terminal histone tails distinguish between NADPH oxidase (NOX)-dependent and NOX-independent pathways of neutrophil extracellular trap formation. *Ann Rheum Dis*. 2018;77(12):1790-1798. doi:10.1136/annrheumdis-2018-213223

Prilutskiy A, Kritselis M, Shevtsov A, et al. SARS-CoV-2 Infection-Associated Hemophagocytic Lymphohistiocytosis. *Am J Clin Pathol*. 2020;154(4):466-474. doi:10.1093/ajcp/aqaa124

Puhach O, Meyer B, Eckerle I. SARS-CoV-2 viral load and shedding kinetics [published online ahead of print, 2022 Dec 2]. *Nat Rev Microbiol*. 2022;1-15. doi:10.1038/s41579-022-00822-w

Qin C, Zhou L, Hu Z, et al. Dysregulation of Immune Response in Patients With Coronavirus 2019 (COVID-19) in Wuhan, China. *Clin Infect Dis.* 2020;71(15):762-768. doi:10.1093/cid/ciaa248

Radermecker C, Detrembleur N, Guiot J, et al. Neutrophil extracellular traps infiltrate the lung airway, interstitial, and vascular compartments in severe COVID-19. J Exp Med. 2020;217(12):e20201012. doi:10.1084/jem.20201012

Reers M, Smith TW, Chen LB. J-aggregate formation of a carbocyanine as a quantitative fluorescent indicator of membrane potential. *Biochemistry*. 1991;30(18):4480-4486. doi:10.1021/bi00232a015

Ren LL, Wang YM, Wu ZQ, et al. Identification of a novel coronavirus causing severe pneumonia in human: a descriptive study. *Chin Med J (Engl*). 2020;133(9):1015-1024. doi:10.1097/CM9.0000000000000722

Reusch N, De Domenico E, Bonaguro L, et al. Neutrophils in COVID-19. *Front Immunol*. 2021;12:652470. Published 2021 Mar 25. doi:10.3389/fimmu.2021.652470

Reymond N, Imbert AM, Devilard E, et al. DNAM-1 and PVR regulate monocyte migration through endothelial junctions. *J Exp Med*. 2004;199(10):1331-1341. doi:10.1084/jem.20032206

Rice CM, Davies LC, Subleski JJ, et al. Tumour-elicited neutrophils engage mitochondrial metabolism to circumvent nutrient limitations and maintain immune suppression. *Nat Commun*. 2018;9(1):5099. Published 2018 Nov 30. doi:10.1038/s41467-018-07505-2

Riva A, Mehta G. Regulation of Monocyte-Macrophage Responses in Cirrhosis-Role of Innate Immune Programming and Checkpoint Receptors. *Front Immunol*. 2019;10:167. Published 2019 Feb 5. doi:10.3389/fimmu.2019.00167

Robinson JM, Karnovsky ML, Karnovsky MJ. Glycogen accumulation in polymorphonuclear leukocytes, and other intracellular alterations that occur during inflammation. *J Cell Biol*. 1982;95(3):933-942. doi:10.1083/jcb.95.3.933

Robinson KM, Janes MS, Pehar M, et al. Selective fluorescent imaging of superoxide in vivo using ethidium-based probes. *Proc Natl Acad Sci U S A*. 2006;103(41):15038-15043. doi:10.1073/pnas.0601945103

Roca E, Ventura L, Zattra CM, Lombardi C. EOSINOPENIA: an early, effective and relevant COVID-19 biomarker?. *QJM*. 2021;114(1):68-69. doi:10.1093/qjmed/hcaa259

Rockx B, Kuiken T, Herfst S, et al. Comparative pathogenesis of COVID-19, MERS, and SARS in a nonhuman primate model. *Science*. 2020;368(6494):1012-1015. doi:10.1126/science.abb7314

Rodriguez L, Pekkarinen PT, Lakshmikanth T, et al. Systems-Level Immunomonitoring from Acute to Recovery Phase of Severe COVID-19. *Cell Rep Med*. 2020;1(5):100078. doi:10.1016/j.xcrm.2020.100078

Rossi A, Pacella I, Piconese S. RNA Flow Cytometry for the Study of T Cell Metabolism. *Int J Mol Sci*. 2021;22(8):3906. Published 2021 Apr 9. doi:10.3390/ijms22083906

Ryabkova VA, Churilov LP, Shoenfeld Y. Influenza infection, SARS, MERS and COVID-19: Cytokine storm - The common denominator and the lessons to be learned. *Clin Immunol*. 2021;223:108652. doi:10.1016/j.clim.2020.108652

Sadiku P, Walmsley SR. Hypoxia and the regulation of myeloid cell metabolic imprinting: consequences for the inflammatory response. *EMBO Rep*. 2019;20(5):e47388. doi:10.15252/embr.201847388

Sadiku P, Willson JA, Dickinson RS, et al. Prolyl hydroxylase 2 inactivation enhances glycogen storage and promotes excessive neutrophilic responses. *J Clin Invest*. 2017;127(9):3407-3420. doi:10.1172/JCI90848

Sadiku P, Willson JA, Ryan EM, et al. Neutrophils Fuel Effective Immune Responses through Gluconeogenesis and Glycogenesis [published correction appears in Cell Metab. 2021 May 4;33(5):1062-1064]. *Cell Metab*. 2021;33(2):411-423.e4. doi:10.1016/j.cmet.2020.11.016

Salvioli S, Ardizzoni A, Franceschi C, Cossarizza A. JC-1, but not DiOC6(3) or rhodamine 123, is a reliable fluorescent probe to assess delta psi changes in intact cells: implications for studies on mitochondrial functionality during apoptosis. *FEBS Lett*. 1997;411(1):77-82. doi:10.1016/s0014-5793(97)00669-8

Schmidl C, Renner K, Peter K, et al. Transcription and enhancer profiling in human monocyte subsets. *Blood*. 2014;123(17):e90-e99. doi:10.1182/blood-2013-02-484188

Schuetz P, Albrich W, Mueller B. Procalcitonin for diagnosis of infection and guide to antibiotic decisions: past, present and future. *BMC Med*. 2011;9:107. Published 2011 Sep 22. doi:10.1186/1741-7015-9-107

Schulte-Schrepping J, Reusch N, Paclik D, et al. Severe COVID-19 Is Marked by a Dysregulated Myeloid Cell Compartment. *Cell*. 2020;182(6):1419-1440.e23. doi:10.1016/j.cell.2020.08.001

Schurink, B., Roos, E., Radonic, T., Barbe, E., Bouman, C.S.C., de Boer, H.H., de Bree, G.J.et al., Viral presence and immunopathology in patients with lethal COVID-19: a prospective autopsy cohort study. *Lancet Microbe*. 2020. 1: e290–e299.

Schwab JM, Chiang N, Arita M, Serhan CN. Resolvin E1 and protectin D1 activate inflammation-resolution programmes. *Nature*. 2007;447(7146):869-874. doi:10.1038/nature05877

Segundo-Val IS, Sanz-Lozano CS. Introduction to the Gene Expression Analysis. Methods Mol Biol. 2016;1434:29-43. doi:10.1007/978-1-4939-3652-6_3

Selders GS, Fetz AE, Radic MZ, Bowlin GL. An overview of the role of neutrophils in innate immunity, inflammation and host-biomaterial integration. *Regen Biomater*. 2017;4(1):55-68. doi:10.1093/rb/rbw041.

Serbina NV, Salazar-Mather TP, Biron CA, Kuziel WA, Pamer EG. TNF/iNOS-producing dendritic cells mediate innate immune defense against bacterial infection. *Immunity*. 2003;19(1):59-70. doi:10.1016/s1074-7613(03)00171-7

Serhan CN, Chiang N, Van Dyke TE. Resolving inflammation: dual anti-inflammatory and pro-resolution lipid mediators. Nat Rev Immunol. 2008;8(5):349-361. doi:10.1038/nri2294

Shang J, Ye G, Shi K, et al. Structural basis of receptor recognition by SARS-CoV-2. *Nature*. 2020;581(7807):221-224. doi:10.1038/s41586-020-2179-y

Shapiro H, Lutaty A, Ariel A. Macrophages, meta-inflammation, and immuno-metabolism. *ScientificWorldJournal*. 2011;11:2509-2529. doi:10.1100/2011/397971

She S, Ren L, Chen P, et al. Functional Roles of Chemokine Receptor CCR2 and Its Ligands in Liver Disease. *Front Immunol*. 2022;13:812431. Published 2022 Feb 25. doi:10.3389/fimmu.2022.812431

Shenoy S. Coronavirus (Covid-19) sepsis: revisiting mitochondrial dysfunction in pathogenesis, aging, inflammation, and mortality. *Inflamm Res*. 2020;69(11):1077-1085. doi:10.1007/s00011-020-01389-z

Shi C, Pamer EG. Monocyte recruitment during infection and inflammation. *Nat Rev Immunol*. 2011;11(11):762-774. Published 2011 Oct 10. doi:10.1038/nri3070

Siddamreddy S, Thotakura R, Dandu V, Kanuru S, Meegada S. Corona Virus Disease 2019 (COVID-19) Presenting as Acute ST Elevation Myocardial Infarction. *Cureus.* 2020;12(4):e7782. Published 2020 Apr 22. doi:10.7759/cureus.7782.

Silvin A, Chapuis N, Dunsmore G, et al. Elevated Calprotectin and Abnormal Myeloid Cell Subsets Discriminate Severe from Mild COVID-19. *Cell.* 2020;182(6):1401-1418.e18. doi:10.1016/j.cell.2020.08.002

Siswanto, Gani M, Fauzi AR, et al. Possible silent hypoxemia in a COVID-19 patient: A case report. *Ann Med Surg (Lond)*. 2020;60:583-586. doi:10.1016/j.amsu.2020.11.053

Soh KT, Wallace PK. RNA Flow Cytometry Using the Branched DNA Technique. *Methods Mol Biol*. 2018;1678:49-77. doi:10.1007/978-1-4939-7346-0_4

Song Y, Liu P, Shi XL, et al. SARS-CoV-2 induced diarrhoea as onset symptom in patient with COVID-19. *Gut*. 2020;69(6):1143-1144. doi:10.1136/gutjnl-2020-320891

Sorbello M, El-Boghdadly K, Di Giacinto I, et al. The Italian coronavirus disease 2019 outbreak: recommendations from clinical practice. *Anaesthesia*. 2020;75(6):724-732. doi:10.1111/anae.15049

Soudja SM, Ruiz AL, Marie JC, Lauvau G. Inflammatory monocytes activate memory CD8(+) T and innate NK lymphocytes independent of cognate antigen during microbial pathogen invasion. *Immunity*. 2012;37(3):549-562. doi:10.1016/j.immuni.2012.05.029

Spinelli E, Mauri T, Beitler JR, Pesenti A, Brodie D. Respiratory drive in the acute respiratory distress syndrome: pathophysiology, monitoring, and therapeutic interventions. *Intensive Care Med*. 2020;46(4):606-618. doi:10.1007/s00134-020-05942-6

Srinivasan S, Cui H, Gao Z, et al. Structural Genomics of SARS-CoV-2 Indicates Evolutionary Conserved Functional Regions of Viral Proteins. *Viruses.* 2020;12(4):360. Published 2020 Mar 25. doi:10.3390/v12040360

Stuart T, Butler A, Hoffman P, et al. Comprehensive Integration of Single-Cell Data. *Cell*. 2019;177(7):1888-1902.e21. doi:10.1016/j.cell.2019.05.031

Stunault MI, Bories G, Guinamard RR, Ivanov S. Metabolism Plays a Key Role during Macrophage Activation. *Mediators Inflamm*. 2018;2018:2426138. Published 2018 Dec 10. doi:10.1155/2018/2426138

Sugiura A, Rathmell JC. Metabolic Barriers to T Cell Function in Tumors. *J Immunol*. 2018;200(2):400-407. doi:10.4049/jimmunol.1701041

Tai H, Xing H, Xiang D, et al. Monocyte Programmed Death Ligand-1, A Predicator for 28-Day Mortality in Septic Patients. *Am J Med Sci*. 2018;355(4):362-367. doi:10.1016/j.amjms.2017.12.008

Tan LY, Komarasamy TV, Rmt Balasubramaniam V. Hyperinflammatory Immune Response and COVID-19: A Double Edged Sword. *Front Immunol*. 2021;12:742941. Published 2021 Sep 30. doi:10.3389/fimmu.2021.742941

Thwe PM, Pelgrom LR, Cooper R, et al. Cell-Intrinsic Glycogen Metabolism Supports Early Glycolytic Reprogramming Required for Dendritic Cell Immune Responses. *Cell Metab*. 2019;30(1):225. doi:10.1016/j.cmet.2019.05.017

Tolstik TV, Bogatyreva AI, Grechko AV, Oishi Y, Markin AM. Features of mitochondrial dynamics in monocytes in inflammatory and metabolic disorders. *Vessel Plus.* 2022; 6:58. http://dx.doi.org/10.20517/2574-1209.2022.22

Tonetti T, Grasselli G, Rucci P, et al. Synergistic Effect of Static Compliance and D-dimers to Predict Outcome of Patients with COVID-19-ARDS: A Prospective Multicenter Study. *Biomedicines*. 2021;9(9):1228. Published 2021 Sep 15. doi:10.3390/biomedicines9091228

Troiano L, Granata AR, Cossarizza A, et al. Mitochondrial membrane potential and DNA stainability in human sperm cells: a flow cytometry analysis with implications for male infertility. *Exp Cell Res.* 1998;241(2):384-393. doi:10.1006/excr.1998.4064

van der Windt GJW, Chang CH, Pearce EL. Measuring Bioenergetics in T Cells Using a Seahorse Extracellular Flux Analyzer. *Curr Protoc Immunol*. 2016;113:3.16B.1-3.16B.14. Published 2016 Apr 1. doi:10.1002/0471142735.im0316bs113

Veiga-da-Cunha M, Chevalier N, Stephenne X, et al. Failure to eliminate a phosphorylated glucose analog leads to neutropenia in patients with G6PT and G6PC3 deficiency. *Proc Natl Acad Sci U S A*. 2019;116(4):1241-1250. doi:10.1073/pnas.1816143116

Venable AS, Henning AL, Prado EA, McFarlin BK. Using Image-Based Flow Cytometry with a FISH-Based FlowRNA Assay to Simultaneously Detect Intracellular TNF-α Protein and mRNA in Monocytes Following LPS Stimulation. *Methods Mol Biol*. 2016;1389:139-151. doi:10.1007/978-1-4939-3302-0_9

Veras FP, Pontelli MC, Silva CM, et al. SARS-CoV-2-triggered neutrophil extracellular traps mediate COVID-19 pathology. J Exp Med. 2020;217(12):e20201129. doi:10.1084/jem.20201129

Vergis N, Khamri W, Beale K, et al. Defective monocyte oxidative burst predicts infection in alcoholic hepatitis and is associated with reduced expression of NADPH oxidase. *Gut*. 2017;66(3):519-529. doi:10.1136/gutjnl-2015-310378

Voss K, Hong HS, Bader JE, Sugiura A, Lyssiotis CA, Rathmell JC. A guide to interrogating immunometabolism. *Nat Rev Immunol*. 2021;21(10):637-652. doi:10.1038/s41577-021-00529-8

Wallace DC. Mitochondrial diseases in man and mouse. *Science*. 1999;283(5407):1482-1488. doi:10.1126/science.283.5407.1482

Walmsley SR, Print C, Farahi N, et al. Hypoxia-induced neutrophil survival is mediated by HIF-1alpha-dependent NF-kappaB activity. *J Exp Med*. 2005;201(1):105-115. doi:10.1084/jem.20040624

Wang C, Xie J, Zhao L, et al. Alveolar macrophage dysfunction and cytokine storm in the pathogenesis of two severe COVID-19 patients. *EBioMedicine*. 2020a;57:102833. doi:10.1016/j.ebiom.2020.102833

Wang J, Li Q, Yin Y, et al. Excessive Neutrophils and Neutrophil Extracellular Traps in COVID-19. *Front Immunol*. 2020b;11:2063. Published 2020 Aug 18. doi:10.3389/fimmu.2020.02063

Wang L, Zhou X, Yin Y, Mai Y, Wang D, Zhang X. Hyperglycemia Induces Neutrophil Extracellular Traps Formation Through an NADPH Oxidase-Dependent Pathway in Diabetic Retinopathy. *Front Immunol*. 2019;9:3076. Published 2019 Jan 8. doi:10.3389/fimmu.2018.03076

Wang T, Du Z, Zhu F, et al. Comorbidities and multi-organ injuries in the treatment of COVID-19. *Lancet*. 2020c;395(10228):e52. doi:10.1016/S0140-6736(20)30558-4

Wang Z, Yin N, Zhang Z, Zhang Y, Zhang G, Chen W. Upregulation of T-cell Immunoglobulin and Mucin-Domain Containing-3 (Tim-3) in Monocytes/Macrophages Associates with Gastric Cancer Progression. *Immunol Invest*. 2017;46(2):134-148. doi:10.1080/08820139.2016.1229790

Weber C, Belge KU, von Hundelshausen P, et al. Differential chemokine receptor expression and function in human monocyte subpopulations. *J Leukoc Biol*. 2000;67(5):699-704. doi:10.1002/jlb.67.5.699

Weisdorf DJ, Craddock PR, Jacob HS. Granulocytes utilize different energy sources for movement and phagocytosis. *Inflammation*. 1982;6(3):245-256. doi:10.1007/BF00916406

Weiss SL, Zhang D, Bush J, et al. Mitochondrial Dysfunction is Associated With an Immune Paralysis Phenotype in Pediatric Sepsis. *Shock*. 2020;54(3):285-293. doi:10.1097/SHK.0000000000001486

Wen W, Su W, Tang H, et al. Immune cell profiling of COVID-19 patients in the recovery stage by single-cell sequencing [published correction appears in Cell Discov. 2020 Jun 20;6:41]. *Cell Discov*. 2020;6:31. Published 2020 May 4. doi:10.1038/s41421-020-0168-9

WHO Working Group on the Clinical Characterisation and Management of COVID-19 infection. A minimal common outcome measure set for COVID-19 clinical research. *Lancet Infect Dis*. 2020;20(8):e192-e197. doi:10.1016/S1473-3099(20)30483-7

Widlansky ME, Wang J, Shenouda SM, et al. Altered mitochondrial membrane potential, mass, and morphology in the mononuclear cells of humans with type 2 diabetes. *Transl Res.* 2010;156(1):15-25. doi:10.1016/j.trsl.2010.04.001

Wilk AJ, Rustagi A, Zhao NQ, et al. A single-cell atlas of the peripheral immune response in patients with severe COVID-19. *Nat Med*. 2020;26(7):1070-1076. doi:10.1038/s41591-020-0944-y

Wilson MS, Wynn TA. Pulmonary fibrosis: pathogenesis, etiology and regulation. *Mucosal Immunol*. 2009;2(2):103-121. doi:10.1038/mi.2008.85

Winstone H, Lista MJ, Reid AC, et al. The Polybasic Cleavage Site in SARS-CoV-2 Spike Modulates Viral Sensitivity to Type I Interferon and IFITM2. *J Virol*. 2021;95(9):e02422-20. Published 2021 Apr 12. doi:10.1128/JVI.02422-20

Wölfel R, Corman VM, Guggemos W, et al. Virological assessment of hospitalized patients with COVID-2019 [published correction appears in Nature. 2020 Dec;588(7839):E35]. *Nature*. 2020;581(7809):465-469. doi:10.1038/s41586-020-2196-x

Wong KL, Tai JJ, Wong WC, et al. Gene expression profiling reveals the defining features of the classical, intermediate, and nonclassical human monocyte subsets. *Blood*. 2011;118(5):e16-e31. doi:10.1182/blood-2010-12-326355

Wrapp D, Wang N, Corbett KS, et al. Cryo-EM structure of the 2019-nCoV spike in the prefusion conformation. Science. 2020;367(6483):1260-1263. doi:10.1126/science.abb2507

Xia L, Oyang L, Lin J, et al. The cancer metabolic reprogramming and immune response. *Mol Cancer*. 2021;20(1):28. Published 2021 Feb 5. doi:10.1186/s12943-021-01316-8

Xia Q, Wei L, Zhang Y, Sheng J, Wu W, Zhang Y. Immune Checkpoint Receptors Tim-3 and PD-1 Regulate Monocyte and T Lymphocyte Function in Septic Patients. *Mediators Inflamm*. 2018;2018:1632902. Published 2018 Nov 22. doi:10.1155/2018/1632902

Xiong Y, Liu Y, Cao L, et al. Transcriptomic characteristics of bronchoalveolar lavage fluid and peripheral blood mononuclear cells in COVID-19 patients. *Emerg Microbes Infect*. 2020;9(1):761-770. doi:10.1080/22221751.2020.1747363

Yan R, Zhang Y, Li Y, Xia L, Guo Y, Zhou Q. Structural basis for the recognition of SARS-CoV-2 by full-length human ACE2. *Science*. 2020;367(6485):1444-1448. doi:10.1126/science.abb2762

Yang W. Early innate immune responses in different COVID-19 sub-phenotypes through a transcriptomics lens. *Clin Transl Discov*. 2022;2(2):e79. doi:10.1002/ctd2.79

Yipp BG, Kubes P. NETosis: how vital is it?. *Blood*. 2013;122(16):2784-2794. doi:10.1182/blood-2013-04-457671

Yu G, He QY. ReactomePA: an R/Bioconductor package for reactome pathway analysis and visualization. *Mol Biosyst*. 2016;12(2):477-479. doi:10.1039/c5mb00663e

Yu G, Wang LG, Han Y, He QY. clusterProfiler: an R package for comparing biological themes among gene clusters. OMICS. 2012;16(5):284-287. doi:10.1089/omi.2011.0118

Yu M, Liu Y, Xu D, Zhang R, Lan L, Xu H. Prediction of the Development of Pulmonary Fibrosis Using Serial Thin-Section CT and Clinical Features in Patients Discharged after Treatment for COVID-19 Pneumonia. *Korean J Radiol*. 2020;21(6):746-755. doi:10.3348/kjr.2020.0215

Zahorec R. Neutrophil-to-lymphocyte ratio, past, present and future perspectives. *Bratisl Lek Listy*. 2021;122(7):474-488. doi:10.4149/BLL_2021_078

Zappia L, Oshlack A. Clustering trees: a visualization for evaluating clusterings at multiple resolutions. *Gigascience*. 2018;7(7):giy083. doi:10.1093/gigascience/giy083

Zasada M, Lenart M, Rutkowska-Zapała M, et al. Analysis of PD-1 expression in the monocyte subsets from non-septic and septic preterm neonates. *PLoS One*. 2017;12(10):e0186819. Published 2017 Oct 19. doi:10.1371/journal.pone.0186819

Zhang B, Zhou X, Zhu C, et al. Immune Phenotyping Based on the Neutrophil-to-Lymphocyte Ratio and IgG Level Predicts Disease Severity and Outcome for Patients With COVID-19. *Front Mol Biosci*. 2020a;7:157. Published 2020 Jul 3. doi:10.3389/fmolb.2020.00157

Zhang C, Wu Z, Li JW, Zhao H, Wang GQ. Cytokine release syndrome in severe COVID-19: interleukin-6 receptor antagonist tocilizumab may be the key to reduce mortality. *Int J Antimicrob Agents*. 2020b;55(5):105954. doi:10.1016/j.ijantimicag.2020.105954

Zhang H, Ma J, Tang K, Huang B. Beyond energy storage: roles of glycogen metabolism in health and disease. *FEBS J*. 2021;288(12):3772-3783. doi:10.1111/febs.15648

Zhang Q, Bastard P, Liu Z, et al. Inborn errors of type I IFN immunity in patients with life-threatening COVID-19. *Science*. 2020c;370(6515):eabd4570. doi:10.1126/science.abd4570

Zhang Y, Zhou Y, Lou J, et al. PD-L1 blockade improves survival in experimental sepsis by inhibiting lymphocyte apoptosis and reversing monocyte dysfunction. *Crit Care*. 2010;14(6):R220. doi:10.1186/cc9354

Zhou F, Yu T, Du R, et al. Clinical course and risk factors for mortality of adult in patients with COVID-19 in Wuhan, China: a retrospective cohort study. *Lancet*. 2020a;395(10229):1054-1062. doi:10.1016/S0140-6736(20)30566-3

Zhou L, Niu Z, Jiang X, et al. SARS-CoV-2 Targets by the pscRNA Profiling of ACE2, TMPRSS2 and Furin Proteases. *iScience*. 2020b;23(11):101744. doi:10.1016/j.isci.2020.101744

Zhu H, Wei L, Niu P. The novel coronavirus outbreak in Wuhan, China. *Glob Health Res Policy*. 2020;5:6. Published 2020 Mar 2. doi:10.1186/s41256-020-00135-6

Zhu X, Meyers A, Long D, et al. Frontline Science: Monocytes sequentially rewire metabolism and bioenergetics during an acute inflammatory response. *J Leukoc Biol.* 2019;105(2):215-228. doi:10.1002/JLB.3HI0918-373R

Ziegler-Heitbrock L, Ancuta P, Crowe S, et al. Nomenclature of monocytes and dendritic cells in blood. *Blood*. 2010;116(16):e74-e80. doi:10.1182/blood-2010-02-258558

Zuo H, Wan Y. Metabolic Reprogramming in Mitochondria of Myeloid Cells. *Cells*. 2019;9(1):5. Published 2019 Dec 18. doi:10.3390/cells9010005

Zuo Y, Yalavarthi S, Shi H, et al. Neutrophil extracellular traps in COVID-19. *JCI Insight*. 2020;5(11):e138999. Published 2020 Jun 4. doi:10.1172/jci.insight.138999